FABRICATION AND CHARACTERIZATION OF III-NITRIDE NANOPHOTONIC DEVICES

By

RAJENDRA PRASAD DAHAL

B. Sc., Tribhuvan University, 1998

M. Sc., Tribhuvan University, 2001

AN ABSTRACT OF A DISSERTATION

submitted in partial fulfillment of the requirements for the degree

DOCTOR OF PHILOSOPHY

Department of Physics

College of Arts and Sciences

KANSAS STATE UNIVERSITY

Manhattan, Kansas

2009

ABSTRACT

III-nitride photonic devices such as photodetectors (PDs), light emitting diode (LEDs), solar cells and optical waveguide amplifiers were designed, fabricated and characterized. High quality AlN epilayers were grown on sapphire and n-SiC substrates by metal organic chemical vapor deposition and utilized as active deep UV (DUV) photonic materials for the demonstration of metal-semiconductor-metal (MSM) detectors, Schottky barrier detectors, and avalanche photodetectors (APDs). AlN DUV PDs exhibited peak responsivity at 200 nm with a very sharp cutoff wavelength at 207 nm and extremely low dark current (<10 fA), very high breakdown voltages, high responsivity, and more than four orders of DUV to UV/visible rejection ratio. AlN Schottky PDs grown on n-SiC substrates exhibited high zero bias responsivity and a thermal energy limited detectivity of about 1.0×10^{15} cm $Hz^{1/2}$ W^{-1}. The linear mode operation of AlN APDs with the shortest cutoff wavelength (210 nm) and a photocurrent multiplication of 1200 was demonstrated. A linear relationship between device size and breakdown field was observed for AlN APDs.

Photovoltaic operation of InGaN solar cells in wavelengths longer than that of previous attainments was demonstrated by utilizing $In_xGa_{1-x}N$/GaN MQWs as the active layer. $In_xGa_{1-x}N$/GaN MQWs solar cells with x =0.3 exhibited open circuit voltage of about 2 V, a fill factor of about 60% and external quantum efficiency of 40% at 420 nm and 10% at 450 nm. The performance of $In_xGa_{1-x}N$/GaN MQWs solar cell was found to be highly correlated with the crystalline quality of the $In_xGa_{1-x}N$ active layer. The possible causes of poorer PV characteristics for higher In content in InGaN active layer were explained.

Photoluminescence excitation studies of GaN:Er and $In_{0.06}Ga_{0.94}N$:Er epilayers showed that Er emission intensity at 1.54 μm increases significantly as the excitation energy is tuned

from below to above the energy bandgap of these epilayers. Current-injected 1.54 μm LEDs based on heterogeneous integration of Er-doped III-nitride epilayers with III-nitride UV LEDs were demonstrated. Optical waveguide amplifiers based on AlGaN/GaN:Er/AlGaN heterostructures was designed, fabricated, and characterized. The measured optical loss of the devices was ~3.5 cm^{-1} at 1.54 μm. A relative signal enhancement of about 8 dB/cm under the excitation of a broadband 365 nm nitride LED was achieved. The advantages and possible applications of 1.54 μm emitters and optical amplifiers based on Er doped III-nitrides in optical communications have been discussed.

FABRICATION AND CHARACTERIZATION OF III-NITRIDE NANOPHOTONIC DEVICES

By

RAJENDRA PRASAD DAHAL

B. Sc., Tribhuvan University, 1998

M. Sc., Tribhuvan University, 2001

A DISSERTATION

submitted in partial fulfillment of the requirements for the degree

DOCTOR OF PHILOSOPHY

Department of Physics

College of Arts and Sciences

KANSAS STATE UNIVERSITY

Manhattan, Kansas

2009

Approved by:

Major Professor

Hongxing Jiang

Copyright

RAJENDRA PRASAD DAHAL

2009

ABSTRACT

III-nitride photonic devices such as photodetectors (PDs), light emitting diode (LEDs), solar cells and optical waveguide amplifiers were designed, fabricated and characterized. High quality AlN epilayers were grown on sapphire and n-SiC substrates by metal organic chemical vapor deposition and utilized as active deep UV (DUV) photonic materials for the demonstration of metal-semiconductor-metal (MSM) detectors, Schottky barrier detectors, and avalanche photodetectors (APDs). AlN DUV PDs exhibited peak responsivity at 200 nm with a very sharp cutoff wavelength at 207 nm and extremely low dark current (<10 fA), very high breakdown voltages, high responsivity, and more than four orders of DUV to UV/visible rejection ratio. AlN Schottky PDs grown on n-SiC substrates exhibited high zero bias responsivity and a thermal energy limited detectivity of about 1.0 x 10^{15} cm $Hz^{1/2}$ W^{-1}. The linear mode operation of AlN APDs with the shortest cutoff wavelength (210 nm) and a photocurrent multiplication of 1200 was demonstrated. A linear relationship between device size and breakdown field was observed for AlN APDs.

Photovoltaic operation of InGaN solar cells in wavelengths longer than that of previous attainments was demonstrated by utilizing $In_xGa_{1-x}N$/GaN MQWs as the active layer. $In_xGa_{1-x}N$/GaN MQWs solar cells with x =0.3 exhibited open circuit voltage of about 2 V, a fill factor of about 60% and external quantum efficiency of 40% at 420 nm and 10% at 450 nm. The performance of $In_xGa_{1-x}N$/GaN MQWs solar cell was found to be highly correlated with the crystalline quality of the $In_xGa_{1-x}N$ active layer. The possible causes of poorer PV characteristics for higher In content in InGaN active layer were explained.

Photoluminescence excitation studies of GaN:Er and $In_{0.06}Ga_{0.94}N$:Er epilayers showed that Er emission intensity at 1.54 μm increases significantly as the excitation energy is tuned

from below to above the energy bandgap of these epilayers. Current-injected 1.54 μm LEDs based on heterogeneous integration of Er-doped III-nitride epilayers with III-nitride UV LEDs were demonstrated. Optical waveguide amplifiers based on AlGaN/GaN:Er/AlGaN heterostructures was designed, fabricated, and characterized. The measured optical loss of the devices was ~3.5 cm^{-1} at 1.54 μm. A relative signal enhancement of about 8 dB/cm under the excitation of a broadband 365 nm nitride LED was achieved. The advantages and possible applications of 1.54 μm emitters and optical amplifiers based on Er doped III-nitrides in optical communications have been discussed.

Table of Contents

List of Figures ... xii

Acknowledgements ... xviii

Dedication ... xviii

CHAPTER 1 - Introduction ... 1

1.1 Crystal Structure of III-nitrides and their Physical Properties ... 2

1.2 III-nitride based UV Solar-blind Photodetectors Development ... 3

1.3 InGaN Alloys and Nanostructures for Photovoltaic Applications ... 9

1.4 Er doped $In_xGa_{1-x}N$ alloys based Emitters and Optical Amplifiers ... 12

1.5 Metals-Semiconductor Junction: Schottky and Ohmic Contacts ... 15

1.6 Overview of the Thesis ... 17

CHAPTER 2 - Experiment: Growth, Fabrication and Characterization Techniques ... 19

2.1 III-nitride photonic devices: Growth ... 19

2.2 III-nitride Photonic Devices: Fabrication ... 21

2.3 Facets preparation for III-nitride laser diode and waveguide amplifier ... 25

2.4 Highly Reflecting Dielectric DBR mirror preparation for LDs ... 27

2.5 Scanning Electron Microscopy (SEM) ... 28

2.6 Atomic Force Microscopy (AFM) ... 32

2.7 Electroluminescence, Current-Voltage, and Light-Current Measurements………… 33

2.8 Photoresponse Measurements for Photodetectors………………….………………… 34

2.9 Other Characterization Techniques……………………..………………………… 35

CHAPTER 3 - AlN MSM Photodetectors…………………….………………………… 37

3.1 Metal-semiconductor-metal Photodetectors…………….…………………………… 37

3.2 Dark Current in MSM Photodetectors………………….……………………………. 38

3.3 Responsivity of MSM Photodetectors…………………..……………………………. 39

3.4 Band Width and Speed of MSM PDs…………………..…………………………….. 41

3.5 AlN based deep UV MSM PDs……………………………..………………………… 42

3.6 AlN epilayer Growth and Characterization………………..………………………. 43

3.7 AlN MSM PDs Fabrication……………………………..…………………………. 47

3.8 AlN MSM PDs Characterization…………………………….………………………. 48

CHAPTER 4- AlN Schottky and Avalanche Photodetectors………………………………… 53

4.1 Schottky Barrier Photodetectors………………..…………………………………….. 53

4.2 AlN based Schottky deep UV Photodetector………………..……………………... 54

4.3 AlN based Schottky deep UV Photodetectors grown on SiC Substrate………………. 55

4.4 AlN SBPDs on SiC Substrate: Growth & Fabrication….…………..………………… 56

4.5 AlN SBPDs on SiC substrate: Device Characterization…………………….….…….. 57

4.6 AlN SBPD on Sapphire Substrate…………………………………………………… 62

4.7 AlN SBPDs on Sapphire substrate: Growth & Fabrication………………………….. 63

4.8 AlN SBPDs on AlN/Sapphire template: Device Characterization…………………….. 65

4.9 Reverse breakdown field comparison for AlN on n-SiC and AlN/sapphire substrates 68

4.10 AlN Avalanche Photodetectors…………………………………………………… 69

4.11 AlN avalanche Photodetectors: Growth and Fabrication…………………………… 70

4.12 AlN avalanche Photodetectors: Characterization…………………………………… 72

CHAPTER 5- InGaN/GaN MQWs Solar Cells………………………………………………. 78

5.1 Introduction………………………………………………………………………… 80

5.2 InGaN/GaN MQWs Solar Cells with Long Operating Wavelength…………………… 82

5.3 InGaN/GaN MQWs Solar Cells: Growth & Fabrication……………………………. 83

5.4 InGaN/GaN MQWs Solar Cells: Device Characterization………………………….. 84

CHAPTER 6- 1.54 μm Emitter and Optical Amplifier based on Er doped InGaN/GaN…….. 87

6.1 Introduction………………………………………………………………………… 87

6.2 Growth of GaN:Er and InGaN:Er…………………………………………………… 89

6.3 Photoluminescence Excitation (PLE) spectroscopy of GaN:Er and InGaN:Er epilayers 89

6.4 Current injected 1.54 μm emitter based on Er doped GaN: Fabrication and Characterization……………………………………………………………………….. 92

6.5 1.54 μm Er doped GaN/AlGaN Waveguide Optical Amplifiers ……………………… 95

6.6 Er doped GaN/AlGaN Optical Waveguide Amplifier: Growth and Fabrication…….. 97

6.7 Er doped GaN/AlGaN Optical Waveguide Characterization: Optical Loss and Signal Amplification Measurement…………………………………………………………... 98

CHAPTER 7- Over all Conclusions………………………………………………………. 103

REFERENCES……………………………………………………………………………. 106

APPENDIX……………………………………………………………………………….. 116

List of Figures

Figures Page

Fig. 1.1 Schematic illustration of the wurtzite lattice structure of III-V nitrides with N atoms (gray sphere) and group III-elements (In, or Ga or Al by yellow sphere) [After Ref. 9]. 3

Fig.1.2 Comparison of photoresponses of $Al_xGa_{1-x}N$ photodetectors in the whole alloys composition range, and also include for cBN photodetectors. 8

Fig. 1.3 Bandgap energy of InGaN alloys system cover the entire solar spectrum. The gap energies of conventional multijunction (MJ) solar materials (Ge, GaAs, and GaInP) are also shown in the right hand panel for comparison (After Ref. 29). 10

Fig. 1.4 Relevant energy levels in the PL of GaN:Er films: excitation laser photon energies, GaN conduction band edge and Er 4*f* energy levels [After Ref. 36]. 13

Fig. 1.5 Energy band diagram of metal and n-type semiconductor, (a) and (b) are flat band diagram, (c) and (d) are under equilibrium after metal and semiconductor are in contact. 16

Fig. 2.1 (a) Optical microscopy image of laser facets prepared by mechanical polishing and (b) AFM image scanned on polished area which revealed surface roughness less than 1 nm for scan size of 10 x10 μm^2. 26

Fig. 2.2 (a) Schematic layer structure of SiO_2/TiO_2 DBR mirror and (b) reflectivity as functions of wavelength of 8 periods SiO_2/TiO_2 DBR mirror. 27

Fig. 2.3 Photograph of SEM interfaced with NPGS (for e-beam lithography) and EDX (for composition determination) system located in nanophotonic lab. 29

Fig. 2.4 SEM image of (a) as grown GaN surface showing the defects, (b) top view of fabricated laser diode, and (c) magnified and tilted view of side wall of dry etch waveguide. 30

Fig. 2.5 SEM image of PC patterns with e-beam after development in e-beam developer.

Fig. 2.6 AFM image of (a) GaN surface after wet etch by phosphoric acid showing etch pits and (b) a fabricated GaN waveguide. 32

Fig. 2.7 Photograph of micro manipulator probe station equipped with optical microscope and CCD camera for measuring I-V, L-I and EL characteristics of LEDs, LDs, PDs and solar cell. The inset is the photograph of green LD probing using this set up. 33

Fig. 2.8 Photograph of measurement set up for I-V and photoresponse of DUV photodetector located in our nanophotonic lab. This set up is also capable of measuring absorption spectra of thin film semiconductors. 35

Fig. 3.1 A schematic diagram of MSM photodetector. 37

Fig. 3.2 Energy band diagram of metal-semiconductor-metal junctions. 39

Fig. 3.3 Room temperature photoluminescence (PL) spectra of AlN epilayer. 44

Fig. 3.4 X-ray diffraction ω scans (rocking curves) of the (a) symmetric plane (002) and (b) asymmetric plane (102) of an AlN epilayer used in this study. 45

Fig. 3.5 Atomic Force Microscopy image (10 x 10 μm^2) of as grown AlN epilayer. 46

Fig. 3.6 Atomic Force Microscopy image (10 x 10 μm^2) of etched AlN epilayer. 46

Fig. 3.7 (a) Schematic layer structure of Fabricated AlN MSM PD, and (b) optical microscopy image of the device with 80 x 80 μm^2 active area having finger width and spacing each 1 μm. 47

Fig. 3.8 Dark I-V characteristics of AlN MSM photodetector. The inset shows the photocurrent stability on switching the polarity of bias voltage. 48

Fig. 3.9 I-V characteristics of AlN MSM photodetector in dark and under 200 nm DUV light illumination (semi-log scale). 49

Fig. 3.10 Spectral response of an AlN MSM detector at V_b = -30 V. 50

Fig. 3.11 Responsivity of AlN MSM photodetector as functions of applied bias. 51

Fig. 4.1 (a) Schematic layer structure of AlN/*n*-SiC hybrid Schottky barrier photodetector and (b) optical microscopy images of fabricated photodetectors with a device size of 100 μm in diameter, but having different ring width and spacing. 56

Fig. 4.2 *I-V* characteristics of an AlN/*n*-SiC hybrid Schottky barrier photodetector. The inset shows the same plot in semilog scale. 58

Fig. 4.3 Spectral photoresponse of an AlN/*n*-SiC hybrid Schottky barrier photodetector measured at V_b=−10 V. 59

Fig. 4.4 Spectral photoresponses of an AlN/*n*-SiC hybrid Schottky barrier photodetector measure at different bias voltages V_b. The inset shows the peak responsivity at 200 nm as a function of V_b. The responsivity in the photovoltaic mode (zero bias) is 0.078 A/W. 60

Fig. 4.5 (a) Schematic layer structure of AlN Schottky barrier photodetector on AlN/sapphire template and (b) optical microscopy image of a fabricated photodetector with a device size of 100 μm in diameter. 64

Fig. 4.6 *I-V* characteristics of an AlN Schottky barrier photodetector on AlN/sapphire template. The inset shows the same plot in semilog scale. 65

Fig. 4.7 Spectral photoresponse of an AlN Schottky PD on AlN/sapphire template measure at V_b = −5 V. 66

Fig. 4.8 Spectral EQE of an AlN Schottky PD under different reverse bias voltages. 67

Fig. 4.9 Reverse break down field comparison for AlN grown on n-SiC and AlN/sapphire template. 68

Fig. 4.10 SEM image of a fabricated AlN APD with *d*=100 μm in diameter. 71

Fig. 4.11 I-V characteristics of AlN APD with *d*=100 μm in dark and under 200 nm light illumination. 72

Fig. 4.12 Photocurrent multiplication or gain of an AlN APD with *d*=100 μm M_{ph} as a function of the reverse bias voltage V_b. M_{ph} increases only slowly at $|V_b|<180$ V,

but increases exponentially at $|V_b|>180$ V and reaches about 1200 at $V_b=-250$ V. The inset is the same plot in the semilog scale. 74

Fig. 4.13 Reverse bias *I-V* characteristics of AlN APDs with d =100, 50, and 30 μm in diameter. The breakdown voltage V_B increases with decreasing device size. 75

Fig. 4.14 Reverse breakdown voltage (V_B) and breakdown field (E_B) as functions of the device area $A(=\pi d^2/4)$ for AlN APDs. The solid lines are the linear least square fits of data. The breakdown field of dislocation-free AlN epilyer (E_B at d=0) is about 4.1 MV/cm. 76

Fig. 5.1 (a) Idealized equivalent circuit and (b) a typical I-V characteristics of solar cell under illumination. 78

Fig. 5.2 (a) XRD Θ-2Θ curves of (002) planes (b) PL emission spectra of representative $In_xGa_{1-x}N$ epilayers (0.2 μm thick) grown on epi-GaN/Al_2O_3 templates. 81

Fig. 5.3 (a) Schematic layer structure of solar cells based on InGaN/GaN MQWs. (b) PL emission spectrum of an $In_xGa_{1-x}N$/GaN MQW (x~0.3) solar cell structure. 83

Fig. 5.4 (a) spectrum of the white light source used for *I-V* characteristics measurements (b) optical microscopy image of a fabricated device. 83

Fig. 5.5 (a) I-V characteristics for a solar cell with $In_xGa_{1-x}N$/GaN MQW (x~0.3 & 0.4) as the active region. (b) J_{sc} (left) and V_{OC} (right) as a function of incident light intensity for $In_{0.3}Ga_{0.7}N$/GaN MQW solar cell. 84

Fig. 5.6 (a) Current- and power-density vs voltage characteristics for a solar cell with $In_xGa_{1-x}N$/GaN MQW (x~0.3) as the active region, (b) External quantum efficiency vs excitation wavelength for the same device. 85

Fig. 6.1 Schematic layer structure of (a) GaN:Er and, (b) $In_{0.06}Ga_{0.94}N$: Er epilayers. 89

Fig. 6.2 (a) RT emission spectra near 1.54 μm of GaN:Er epilayer with III-nitride LEDs excitation. The excitation wavelengths (λ_{exc}) varies from 362 to 470 nm, corresponding to energies from below to above bandgap of the host GaN and the

emission intensities were normalized to the LED optical power outputs, (b) PLE spectrum probed at 1.54 μm (left axis) and optical absorption spectrum (right axis) of GaN:Er. Fringes in the absorption spectrum are due to thin film (GaN:Er) interference effects. 90

Fig. 6.3 PLE spectrum probed at 1.54 μm (left axis) and absorption spectrum (right axis) of a $In_{0.06}Ga_{0.94}N$:Er epilayer. Emission intensity at 1.54 μm, I_{emi}, increases sharply for excitation energy greater than 3.18 eV (λ_{exc}<390 nm) corresponding to the RT band-gap of $In_{0.06}Ga_{0.94}N$. 92

Fig. 6.4 Schematically illustrates that the 1.54 μm LED is fabricated by heterogeneous integration of a GaN:Er epilayer with a 365 nm III-nitride LED. 93

Fig. 6.5 (a) IR emission spectra of a current-injected 1.54 μm LED under different injection current levels. The inset is the visible emission spectrum of the same device, showing virtually no Er-related emission in the spectral range of 430–850 nm. (b) Emission intensity (I_{emi}) of the same 1.54 μm LED as a function of the forward injection current. 94

Fig. 6.6 Schematic layer structure of fabricated strip Er-doped GaN waveguide amplifier, which utilizes GaN: Er as optical gain medium with $Al_{0.03}Ga_{0.97}N$ as top and bottom cladding layers. 97

Fig. 6.7 Atomic force microscopy image of fabricated devices. The inset shows the optical microscopy image of waveguide facets prepared by mechanical polishing. 98

Fig. 6.8 (a) PL spectra of Er-doped GaN waveguide amplifier taken from the end facet of the waveguide when the other end is illuminated by a 371 nm nitride laser. 1.54 μm emission was generated at the laser excitation spot within the core of the waveguide and guided to the end facet of the waveguide. The inset shows the optical loss measurement setup, and (b) plot of 1.54 μm peak intensity as a function of laser excitation spot distance, *d*. The slope of the plot gives the optical loss, which is about 3.5 cm^{-1}. 99

Fig. 6.9 Schematic set up for the optical amplification property measurement. The excitation source is III-nitride high power LEDs. 100

Fig. 6.10 Spectra of the transmitted 1.54 μm signal emerged from the exit end of the Er-doped GaN waveguide measured under the excitation by a 365 nm high power nitride LED operating at different forward currents. The intensity of the 1.54 μm signal guided through the waveguide increases with an increase of the forward current applied to the 365 nm LED, demonstrating a relative signal gain at 1.54 μm. 101

Acknowledgements

I would like to express my gratitude to all those who gave me the possibility to complete this dissertation. I extend my sincere gratitude and appreciation to my advisors Professor Hongxing Jiang and Professor Jingyu Lin for their persistent encouragement, effective guidance and presence throughout the course of this dissertation. Special thanks are due to Dr. Jing Li, Prof. Sixuan Jin and Weiping Zhao for their help in learning different experimental techniques. I would like to thank Dr. Jing Li, Dr. Mim Lal Nakarmi, Dr. Talal Al Tahtamouni, and Dr. Cris Ugolini for sharing MOCVD grown samples and useful discussions. Many thanks are due to Dr. Zhaoyang Fan, Dr. Jagat Shakya, Dr. Neeraj Nepal, Dr. Neelam Khan, Bed Nidhi Pantha, Ashok Sedhain and other past and present members of the GaN research group for their kind assistance and useful discussions. In addition, I would also like to thank Prof. Christopher Culbertson and Prof. Michael O'Shea for serving on my advisory committee, and Prof. Kevin Lease, my committee chairperson. I truly appreciate their time and effort.

I would also like to acknowledge the financial support provided to me from the physics department of Kansas State University and Electrical & Computer Engineering department of Texas Tech University for providing internship for last two semesters. Thanks are due to Frank Jiang for his time and efforts for proof reading of the thesis. I am obliged to acknowledge the aid received from mechanical shop, electronics shop and administrative staffs of physics department at Kansas State University.

Last but not the least; I am thankful to my parents, *Ba:* Durga Prasad Upadhaya Dahal and *Ama:* Om Kumari Upadhaya Dahal, my wife Nirja, daughter Prajeeta and other family members for their affection and support without which I would not have been here.

Dedication

To my parents, wife Nirja and daughter Prajeeta

CHAPTER 1-INTRODUCTION

III-nitride wide bandgap semiconductors, with direct energy bandgaps spanning from 0.7 eV (InN), 3.4 eV (GaN) to 6.1 eV (AlN) have been established technologically as very important photonic and optoelectronic materials. Intense research efforts have been devoted to achieving high quality III-nitride materials for solid-state devices. These III-nitride based devices are efficient, compact and robust compared to devices based on narrow bandgap semiconductors such as Si, GaAs etc [1-4]. The complete miscibility of the pure phases of AlN-GaN and the partial miscibility of InN-GaN offer tuning of the energy bandgap over a wide range through the use of alloying and heterostructure design. Moreover, the large band offset for InN/GaN/AlN allows novel quantum wells (QWs) nanophotonic device design. These properties offer an enormous variety of possible applications such as light emitting diodes (LEDs) and laser diodes (LDs) with emission wavelength ranging from green to deep ultraviolet (UV). It is anticipated that solid-state lighting devices like high power LEDs will replace incandescent light bulbs and fluorescent lamps for energy savings. Other applications of III-nitrides involve high electron mobility transistors (HEMTs), high frequency/high power amplifiers, solar blind photodetectors (device that can detect the radiation in narrow wavelength window of 240 to 285 nm, a UV absorption band at the surface of the earth, without interference from the sun), and gas sensors [5-6].

Recently, the application of III-nitride based photonic devices have expanded (beyond its conventional use for emitters and detectors) into the emerging fields of bio- and chemical sensors, optical communication technology, and energy harvesting devices such as solar cells and photo-electrochemical cells (PEC) for H_2 generation by water splitting via sunlight. Efficient solid-state UV light sources/sensors are crucial in many fields of research and development. For

instance, protein fluorescence is generally excited by UV light. Monitoring changes of intrinsic fluorescence in a protein can provide important information on its structural changes [7]. Thus, the availability of chip-scale UV light sources and sensors is expected to open up new opportunities for medical research and health care. Solid-state UV light sources also have applications in water purification, equipment/personnel decontamination, and white light generation [8]. Furthermore, wide bandgap III-nitride semiconductors have a much lower intrinsic carrier concentrations over a wide temperature range than Si or GaAs because the intrinsic carrier concentration is an exponential function of the bandgap energy and temperature. This results in lower leakage and dark currents, which is especially important in photodetectors and HEMT based chemical and bio-sensors.

1.1 Crystal Structure of III-nitrides and their Physical Properties

III-nitrides commonly refer to AlN, GaN, and InN and their alloys, and are compounds of nitrogen, the smallest group V element in the Periodic Table with one of the highest values of electronegativity. Unlike more conventional semiconductors, such as silicon (Si) or gallium arsenide (GaAs), which have a diamond or zinc-blende structure with a cubic symmetry, III-nitride semiconductors crystallize into a wurtzite crystallographic structure, [Fig. 1.1] which is a thermodynamically stable structure with nitrogen atoms forming a hexagonal close packed (hcp) structure and the group III atoms occupying half of the tetrahedral sites available in the hcp lattice [9]. Due to the lack of a center of symmetry, III-Nitrides are polar crystals, causing them to possess many interesting properties such as piezoelectricity, pyroelectricity and non-linear optical properties [10]. The big difference in electro-negativity between the group III elements and nitrogen (Al = 1.18, Ga= 1.13, In = 0.99, N = 3.1) results in very strong chemical bonds

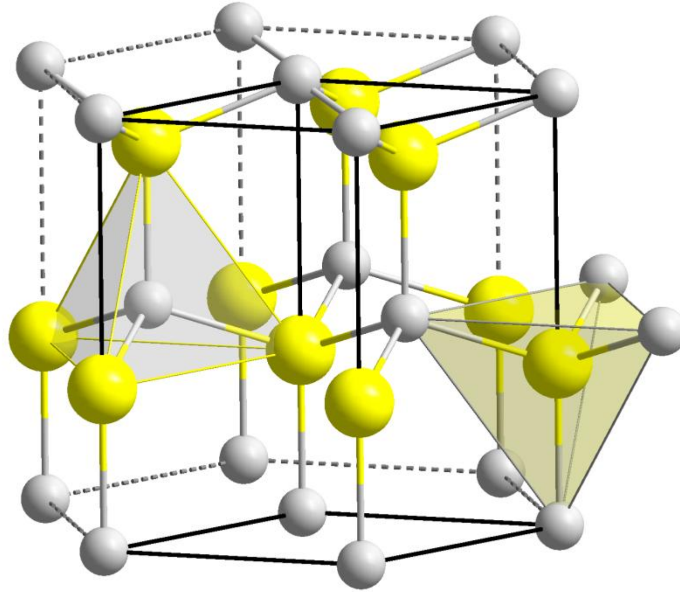

Fig. 1.1 Schematic illustration of the wurtzite lattice structure of III nitrides with N atoms (gray sphere), and group III-elements (In, or Ga or Al by yellow sphere) [After Ref. 9]

within the III-nitride materials system, which make them attractive for fabricating optoelectronic devices capable of operating in chemically harsh-environments. Because of compact crystal networks with relatively large bandgap, III-nitrides possess very high breakdown field (~4 MV/cm for GaN) which permit optoelectronic devices to be scaled down to an order of magnitude smaller than devices of conventional narrow bandgap materials. Furthermore, Ill-nitride semiconductors have a much higher electron saturation velocity (~2-3 x10^7cm/sec) which makes them attractive for designing high speed devices such as HEMTs and high speed photodetectors.

III-nitride based UV Solar-blind Photodetectors Development

The ultraviolet (UV) region of the electromagnetic spectrum is commonly considered to cover the spectral range from λ~10 to 400 nm and is generally subdivided into three spectral bands: UVA (λ=400–320 nm), UVB (λ=320–280 nm), and UVC (λ<280 nm). The ozone layer in

the terrestrial atmosphere strongly absorbs photons with wavelengths between 200 to 300 nm. Forthermore, the molecular gases such as O_2, CO_2, etc present in the Earth's atmosphere strongly absorb photons with wavelengths shorter than $\lambda=200$ nm. Therefore, UV radiations with $\lambda<200$ nm are called vacuum UV (VUV). Due to the strong absorption of photons from the sun with $\lambda<290$ nm by ozone and other molecular gases, the Earth surface receives very weak radiation of $\lambda<290$ nm. Photodetectors having a spectral response only for photons with $\lambda<290$ nm do not detect any effect of the solar radiation on Earth. Such photodetectors are called "solar-blind" photodetectors. Likewise, photodetectors having a spectral response only for $\lambda<400$ nm (i.e., don't see the effect of visible light) are called "visible-blind" photodetectors.

Photodetectors are an integral part of many optoelectronic systems. Since the beginning of UV research in the latter half of 19th century, photomultiplier tubes (PMTs) have been widely used for photon detection in the UV region of the electromagnetic spectrum. PMTs offer high-sensitivity in the UV spectral region and possess an internal photocurrent gain greater than 10^6. Combined with low dark currents and high detection speed, this makes PMTs very attractive for low light detection applications, especially in the UV region. However, PMTs are bulky, fragile, require high bias voltage (>1 kV), cooling hardware and expensive filters to attenuate unwanted long-wavelength signals in the visible spectral region, and are sensitive to magnetic fields. These disadvantages impede the use of PMTs for UV detection in space and outdoor applications.

UV-enhanced solid state Si semiconductor detectors (Schottky or p–i–n diodes) with a special anti-reflection coating designed for the UV wavelength range are viable alternatives. These Si based detectors have many important advantages such as compactness, light weight, high reliability, and compatibility with other semiconductor components. However, their dark currents are high (>nA range at room temperature) and quantum efficiencies in short wavelength

regions are low due to the narrow and indirect bandgap, respectively. Further, the prolonged use of these detectors in deep UV region degrades their efficiency due to the generation of surface states. Also, Si detectors are sensitive throughout the UV and visible wavelengths, which requires costly UV filters for visible- or solar-blind applications.

There is a demand for UV detectors that can overcome the technological limitations associated with PMTs and Si detectors for visible- or solar-blind applications. Photodetectors based on other semiconductors such as Ge, GaAs, and SiC have also been studied by researchers in order to combine the sensitivity of a PMT and the compactness, light-weight, minimum power usages of Si with ‘‘blindness’’ to longer wavelengths [11-12]. Ge and InGaAs offer no obvious advantages over Si. SiC has a bandgap of 3.4 eV and can be used for visible-blind applications, but 4H–SiC has only one fixed band-edge which cannot be tailored to solar-blind applications. Besides, due to indirect bandgap of SiC, its efficiency is expected to be lower than direct bandgap semiconductors.

The recent progress in high quality material growth techniques for wide bandgap semiconductors like $Al_xGa_{1-x}N$ (x = 0 to 1) with both conductivities (n- and p-type) makes it feasible to fabricate compact, robust, and highly sensitive III-nitride based UV photodetectors whose cut-off wavelength can be tuned from 365 nm (GaN) down to 200 nm (AlN). Interest in the development of wide band gap semiconductor UV photodetectors has been driven by its wide range of potential applications in defense, commercial, and scientific arenas. These include covert space-to-space communications, secure non-line-of-sight communications, early missile threat detection, detection of UV scintillation for medical imaging, monitoring of pollutants like nitrous oxide and sulfur dioxide in the ionosphere, in space-based instrumentation for UV astronomy, and in UV photolithography for semiconductor processing. For most of these

applications, the detectors need to be highly sensitive to weak UV signals, but blind to strong visible radiation. The initial development of III–nitride photodetectors was started in the early 1990s because of the easy growth and fabrication of photodetector structures. In the last two decades, significant progress had been made in the development of AlGaN-based photodetectors. These UV detectors, unlike those based on traditional narrow band gap semiconductors such as Si and GaAs, are making strides in detecting UV radiation from 365 nm to x-rays, as well as alpha particles with improved sensitivity, high spectral selectivity and responsivity, and low noise. Recently, as the growth of high Al content AlGaN alloys has matured, interest has focused not only on detectors operating in the solar-blind region of the UV spectrum but also on the extreme UV region down to x-rays wavelength region. It was demonstrated by Miyake et al [13] that AlGaN alloys outperform GaN in terms of photoresponsivity in the EUV and VUV region due to their wider energy bandgaps. As an example, for λ <193 nm, the responsivity of $Al_{0.5}Ga_{0.5}N$ detector is 16 times higher than that of GaN detector mainly due to larger bandgap of $Al_{0.5}Ga_{0.5}N$ than GaN. Thus, it is expected that the photon detection efficiency of AlGaN based detectors in EUV and VUV regions increases with an increase of Al content and is the highest for pure AlN.

In the past, Al rich $Al_xGa_{1-x}N$ alloys (x>0.5) and pure AlN were considered as insulating materials due to their ultra high bandgaps, which limits device design and functionality. Mostly, AlN was used as submount for optoelectronic devices due to its better thermal conductivity. Due to tremendous efforts devoted by many researchers to the growth of Al rich AlGaN alloys and pure AlN, the crystalline and optical qualities of these materials have improved significantly. They have been used as a buffer layer (grown at lower temperatures with relatively lower crystalline quality) and dislocation filter layer (relatively thick, about few μm, grown at high

temperature) for the growth of AlGaN based optoelectronic devices on foreign substrates such as Si, Al_2O_3 and SiC. There have been a few reports of AlN based sound acoustic wave (SAW) devices. Recently, it was demonstrated that AlN epilayers with an optical quality comparable to GaN can be grown on both sapphire and SiC substrates by MOCVD. Several groups have also achieved significant progress towards the realization of conductive AlGaN alloys with high Al contents. Furthermore, it was also demonstrated that n-type AlN with reasonable electrical conductivity [14] can be achieved with Si doping. These progresses stimulated the research work for the realization of active devices based upon pure AlN. More recently, LEDs based on pure AlN with an emission wavelength of 210 nm have been demonstrated [15]. These recent progresses have demonstrated the high promise of AlN as an active material for optoelectronic device applications. Many groups have previously demonstrated UV photodetectors based on AlGaN alloys with superior performances. However, the shortest cut-off wavelength achieved with AlGaN so far is 229 nm. Recently, BenMoussa et al. [16] compared the spectral photoresponses in VUV region of photodetectors based on $Al_xGa_{1-x}N$ alloys for whole compositional range. The growth, fabrication and packaging of AlN MSM photodetector was done by our group and the results are shown in Fig. 1.2 below.

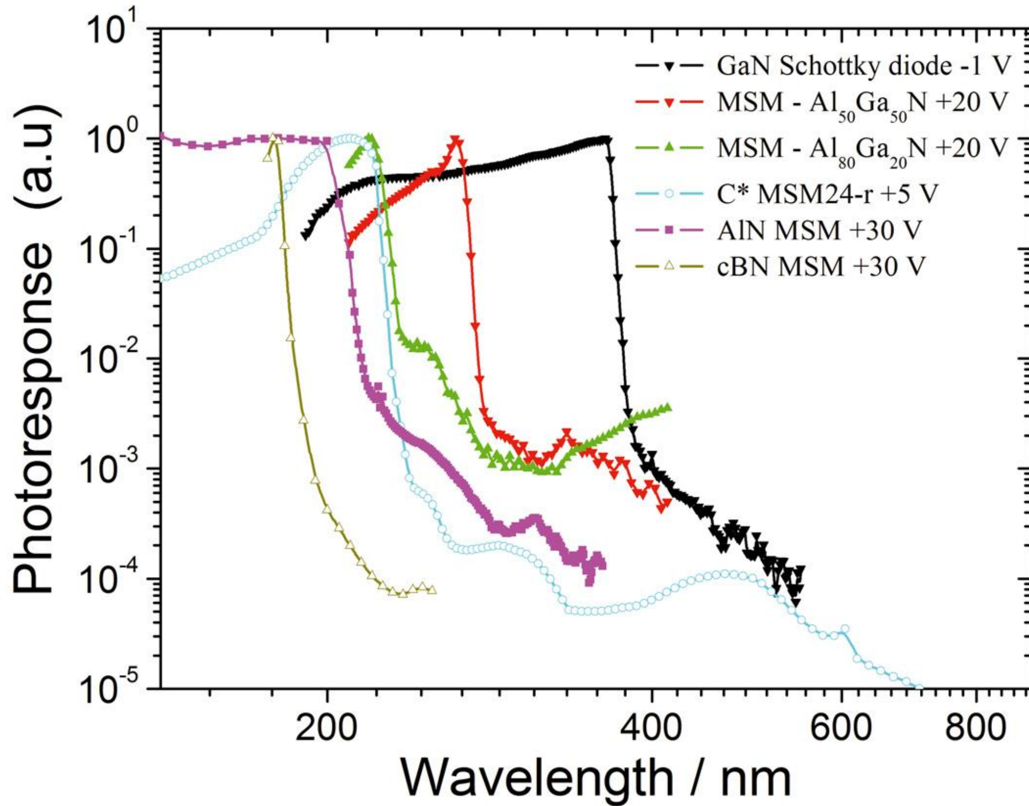

Fig.1.2 Comparison of photoresponses of $Al_xGa_{1-x}N$ photodetectors in whole alloys composition range, and also included are cBN photodetectors. (After Ref. 16)

From Fig. 1.2, it is seen that pure AlN based MSM photodetectors outperform other photodetectors with lower x (Al) content in $Al_xGa_{1-x}N$ alloys, including cubic boron nitride (cBN) based photodetectors.

Many research studies conducted to the development of GaN-based visible-blind and AlGaN-based solar-blind detectors have been published over the past 15 years. Material properties of the AlGaN system, growth and fabrication details, and operating principles of photodetectors have already been discussed in several publications [17-21]. In chapters 3 and 4 of this dissertation work, we present growth, fabrication and characterization of AlN based MSM, Schottky and avalanche photodetectors. AlN, the widest bandgap material in the $In_xAl_yGa_{1-x-y}N$ quaternary system, has an energy corresponding to λ=200 nm, making it useful as

a transparent substrate for DUV optoelectronic devices. Photodetectors based on AlN can potentially provide improved receiver sensitivity, lower noise, and lower dark current densities for short-wavelength radiation in the VUV and EUV spectral regions than photodetectors based on other more conventional semiconductors as well as AlGaN alloys with lower Al contents . In addition, due to their structural, chemical, and thermal stability, the devices based on AlN are well suited to high-temperature and harsh-environment applications.

1.3 InGaN Alloys and Nanostructures for Photovoltaic Applications

The energy reaching the earth's surface from the sun in one hour is more than the total global energy consumption in one year (~15 TW). Solar cells are devices that convert solar energy directly into electricity by the photovoltaic effect discovered by the French scientist Henri Becquerel in 1839. Solar cells are regarded as one of the alternative renewable, carbon-free electric energy resources to address the issues of fossil fuel shortage and global warming. Most solar cells are composed of semiconductors with solid state characteristics that cause the separation of photo-generated carriers (electron-hole pairs) with current flow in the external circuit. Although the total solar energy received on the earth is a huge amount, the solar energy density (solar energy per unit area) is very small (~1kW/m^2) and thus requires a large area of energy converters to supply the energy demand. Therefore, high efficiency solar energy conversion is very crucial not only to meet energy demands but also to achieve cost competitive production.

One of the major causes for low energy conversion efficiency in a solar cell is the energy loss due to a difference in incident photon energy and the bandgap energy (E_g) of the photovoltaic material. If $h\nu < E_g$, no absorption would takes place and if $h\nu > E_g$ only a part of

the energy equal to E_g would be converted into electric power, wasting the remaining part as heat. Tremendous efforts have been devoted to look for PV materials with suitable energy bandgaps that cover the whole solar spectrum (solar spectrum spans from~300 to 2000 nm with highest intensity in 500-600 nm range). Efforts have also been made for designing multi-junction (MJ) solar cells by bandgap engineering and heterostructure design in different material systems [22-23]. Multistacking of PV materials of different bandgap energies is one of the commonly

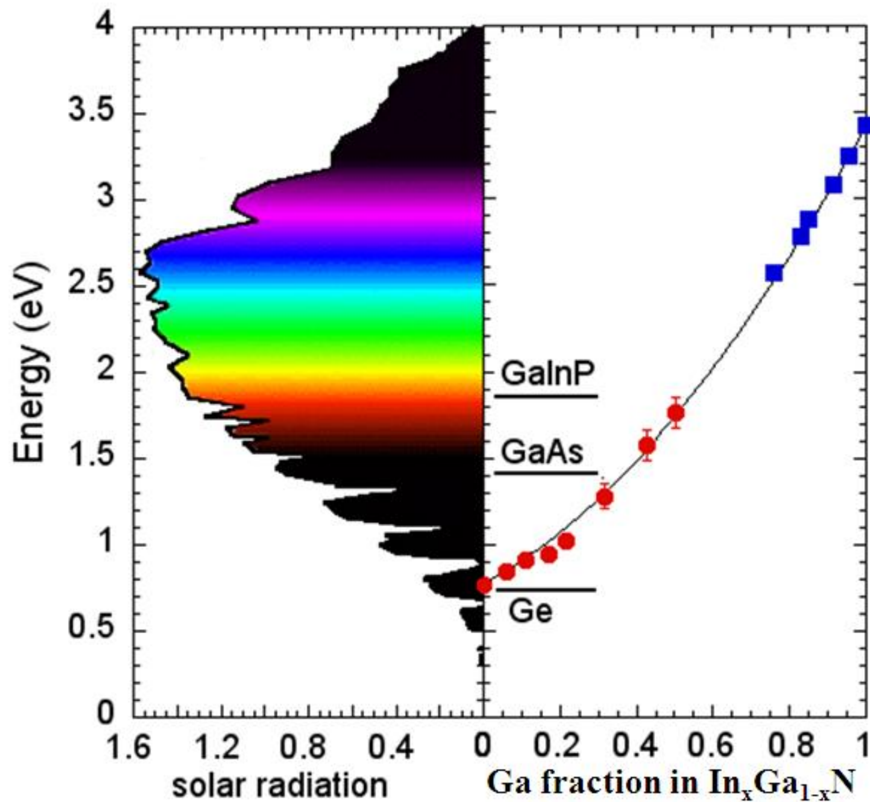

Fig. 1.3 Bandgap energy of InGaN alloys system cover the entire solar spectrum. The gap energies of conventional multijunction (MJ) solar materials (Ge, GaAs, and GaInP) are also shown in the right hand panel for comparison. (After Ref. 29)

used techniques to achieve high efficiency semiconductor solar cells with minimum energy loss. Multijunction (MJ) solar cells can absorbs photon energy from the solar spectrum more widely and efficiently, taking advantage of the tunability of bandgap energies and lattice constants with the compositions of individual layer.

$In_xGa_{1-x}N$ alloys recently emerged as a new solar cell material system due to their tunable bandgaps (varying from 0.7 eV for InN to 3.4 eV for GaN) and superior photovoltaic characteristics (direct energy bandgap in the entire alloy range and high carrier mobility, drift velocity, radiation resistance, and optical absorption of ~10^5 cm^{-1} near the band edge) [24-28]. Figure 1.3 shows the bandgap energy as a function of Ga content (1-x) in $In_xGa_{1-x}N$ alloys which covers almost the whole solar spectrum range. The bandgap energies of widely used materials such as Ge (0.66 eV), GaAs (1.43 eV) and GaInP (1.9 eV) to design high efficiency MJ solar cells has been indicated in Fig. 1.4 as a reference. Although the growth of high optical and crystalline quality In rich InGaN alloys without phase separation is challenging, the growth of MJ solar cells using a single ternary alloy system of InGaN is attractive due to the flexibility of selecting bandgap energies (simply changing In content) for different junctions, which is not possible for currently used MJ solar cells based on Ge, InGaAs, and InGaAsP. Furthermore, InGaN alloys have great potential for use in solar cells for space applications as they possess a higher degree of radiation resistance [29, 30].

Incorporation of low-dimensional semiconductor structures such as quantum dots (QDs), quantum wells (QWs), nanowires, nanotubes, etc in solar cell structures has been utilized to achieve high-efficiency photovoltaics [31-34]. QWs and QDs have been proposed as an effective way to exceed the Shockley–Queisser limit of ~31% power conversion efficiency for homojunction devices [31, 32, 35]. Incorporation of QDs and MQWs in the active layer of p-i-n structure solar cells is beneficial for achieving long wavelength absorption because they are not limited by selection rules for optical transitions in QWs and the size effects also help to mitigate strain effects in the active layer. Well established technology for the growth and fabrication of highly efficient InGaN based MQW or QD emitters with emission wavelength ranging from the

green to UV region is an obvious advantage for the design and growth of MJ solar cells. InGaN QWs and QDs in the light absorption layer are expected to yield higher conversion efficiency.

1.4 Er doped $In_xGa_{1-x}N$ alloys based Emitters and Optical Amplifiers

The incorporation of rare-earth atoms into a semiconductor host has received much attention in the last 30 years due to the potential applications of rare-earth doped materials in areas ranging from optoelectronic to all-optical semiconductor devices. A majority of the research done for rare-earth doping has been focused on the element Er, since Er^{3+} has sharp spectral emissions from the visible to near infrared region due to its intra-4f transitions as depicted in Fig. 1.4 [36]. The transitions from the first excited state ($^4I_{13/2}$) to the ground state ($^4I_{15/2}$) occur at ~ 1.54 μm, which overlaps with the minimum loss window of silica fibers for optical communications. The problem with Er^{3+} emissions in narrow bandgap semiconductor hosts is the low emission efficiency at room temperature due to a strong thermal quenching effect. It has been well established that the thermal stability of Er emissions increases with an increase of the energy bandgap and the crystalline quality of the semiconductor host materials [37-40]. Furthermore, it has also been suggested that the neighboring environment created by more ionic host semiconductors increases the emission efficiency of intra-4f Er^{3+} transitions [38, 41, 42]. In light of these properties, III-nitride wide bandgap semiconductors appear to be excellent host materials for Er ions not only due to their structural and thermal stability but also due to the recent advancements in growth techniques for high crystalline quality nitride materials with both n- and p-type conductivities.

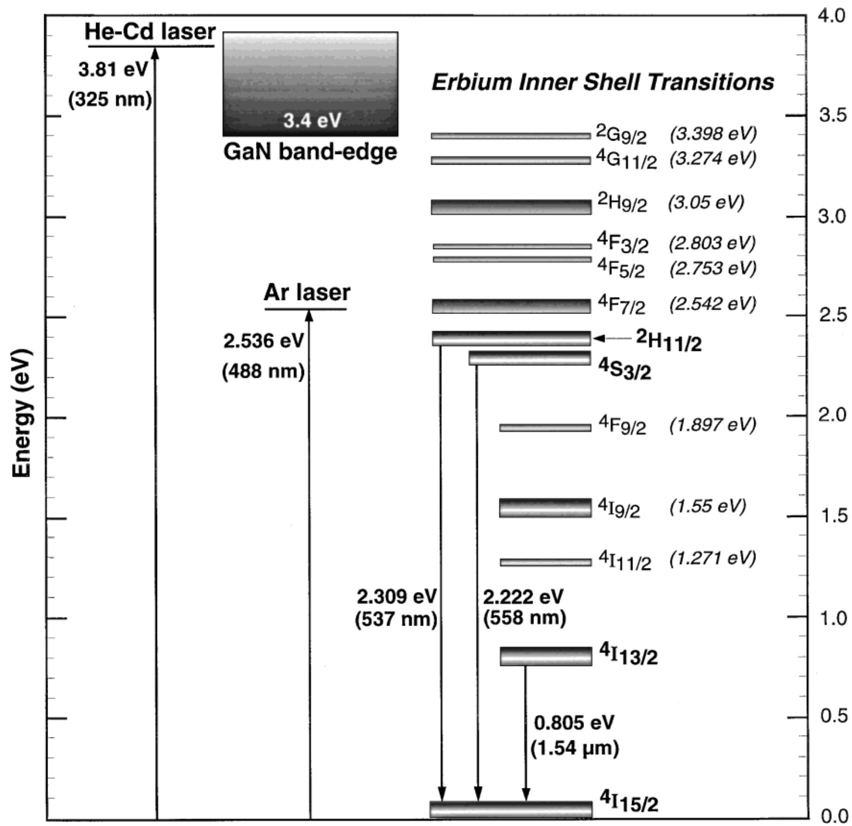

Fig. 1.4 Relevant energy levels in emission lines of GaN:Er films: excitation laser photon energies, GaN conduction band edge and Er 4*f* energy levels. [After Ref. 36]

Initially, Er was incorporated into GaN through ion implantation and reactive sputtering. Ion implantation leads to doping profiles and creates damage effects that often require post implantation annealing due to lattice damage. However, annealing does not completely recover the implantation damage. In GaN implanted with Er, the majority of Er^{3+} ions sit on the Ga substitution sites. Other sites associated with defects have also been identified. The research on Er:GaN done in the late 1990s concentrated on photoluminescence (PL), and PL excitation (PLE) spectroscopy of Er implanted GaN. While the GaN material was of poor quality, Er related PL emission at infrared wavelengths (~1540 nm) was reported [42-44]. Due to advances in materials growth, the quality of Er doped III-nitride (InGaN, AlGaN) epilayers has improved greatly. In addition to ion implantation, techniques used for the doping of these materials now include in situ processes such as molecular beam epitaxy (MBE) and metal organic chemical

vapor deposition (MOCVD). In situ incorporation of Er into semiconductors produces higher crystalline quality epilayers and improved Er related emission as compared to ex-situ incorporation. The successful in situ incorporation of Er in InGaN/GaN material systems by MOCVD with predominate emissions at 1.54 μm has been achieved. Monolithic integration of Er doped InGaN/GaN epilayers with nitride LEDs and LDs with emission wavelengths matching the band gap of host nitride materials opens the possibility of achieving planar waveguide amplifiers and emitters operating in c-band communication window (1530-1550 nm). Optical or current injected waveguide amplifiers based on Er doped InGaN/GaN are expected to have better performance in terms of linear gain, temperature stability and low noise, than either Er doped silica glasses or narrow bandgap semiconductor materials such as InP. Optical amplifiers and emitters operating at 1.54 μm based on Er-doped III-nitride semiconductors are expected to be electrically pumped, chip-scale, integratable, and low cost. These properties allow for the fabrication of novel electrically pumped optical amplifiers that possess the advantages of both semiconductor amplifiers (small size, electrical pumping, ability for photonic integration, etc) and Er-doped fiber amplifiers (minimal crosstalk between different wavelength channels in wavelength division multiplexing). Furthermore, it would lead to integration with other functional optical devices, such as wavelength routers, optical switches, light sources, and detectors, allowing for the construction of monolithic photonic integrated circuits (PICs). This prospect becomes especially attractive if Er-doped III-nitride materials can be grown on large area silicon substrates because such nitride-on-Si photonic material systems would be compatible with the standard processes of CMOS (complementary metal-oxide semiconductor) technology and could open up unprecedented applications including those envisioned for Si photonics.

1.5 Metals-Semiconductor Junction: Schottky and Ohmic Contacts

Metal-semiconductor (MS) junctions are a critical component for the performance of current injected semiconductor devices. The behavior of current transport between metal contact and semiconductor depends on the characteristics of the semiconductor and metal and the interface between them. MS junctions could be rectifying (Schottky barrier) or linear (Ohmic) type depending on the work functions of metals and semiconductors. Many of the characteristics of p-n junctions can be realized by forming an appropriate MS rectifying contact, which is simple to fabricate and the switching speed is much higher than that of p-n junction diodes. However, the poor quality interface could allow large leakage current under reverse bias. Schottky contacts are used in photodetectors, current rectifying diodes, and to control the channel conductivity in hetero-structure field effect transistors HFETs. MS junctions are also used as Ohmic contacts to transport current into and out of the semiconductor devices.

For an ideal metal-semiconductor contact, according to Schottky theory, the Schottky barrier height, Φ_b, depends only on the difference between contact metal work function, $\Phi_{m,}$ and electron affinity of semiconductor, χ, and is related as

$$\Phi_b = \Phi_m - \chi_s \qquad (1)$$

Φ_m and χ are fundamental property of metal and semiconductor, respectively. However, the work function of semiconductor, Φ_s, depends on doping levels and can be expressed as

$$\Phi_s = \chi_s + (E_C - E_F) \qquad (2)$$

where E_C and E_F are the conduction band edge and Fermi level of semiconductor, respectively.

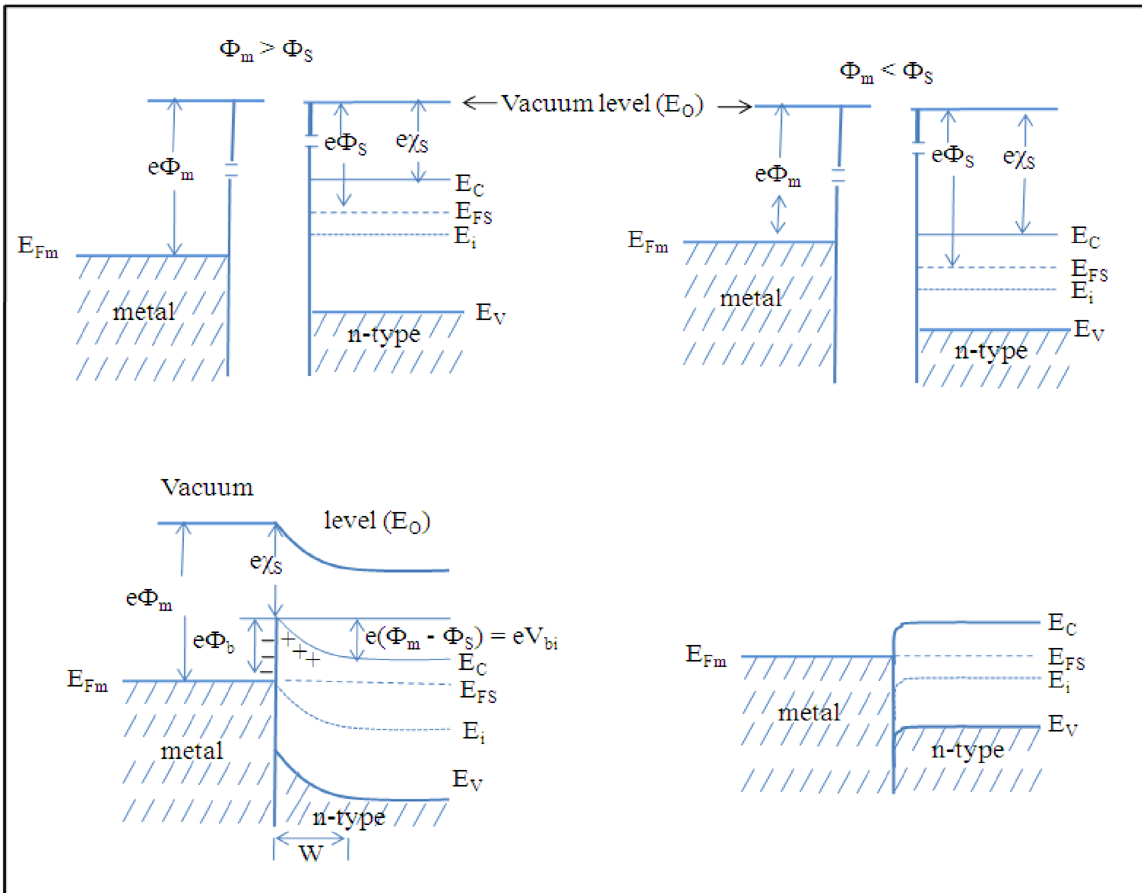

Fig. 1.5 Energy band diagram of metal and n-type semiconductor, (a) and (b) are flat band diagrams, (c) and (d) are under equilibrium after metal and semiconductor are in contact.

Fig. 1.5 shows energy band diagrams of metal and n-type semiconductor in isolated condition for (a) $\Phi_m > \Phi_s$, and (b) $\Phi_m < \Phi_s$. When metals and semiconductors are in contact, Fermi levels line up due to re-distribution of carriers which results in the band bending of the semiconductor due to the depletion of majority carriers. Under equilibrium condition, the band diagrams are shown for $\Phi_m > \Phi_s$, [Fig. 1.5 (c)] and $\Phi_m < \Phi_s$, (Fig. 1.5 (d)) respectively. For $\Phi_m < \Phi_s$, no barrier exists for electrons flowing from semiconductor to metal, but a small barrier exists for electron flow from metal to semiconductor, which is easily overcome by applied voltage, $V_A<0$. So, equal current can flow through the metal-n-type semiconductor junction for $\Phi m < \Phi_s$,. The same is true for metal-p-type semiconductor for $\Phi_m > \Phi_s$. Such junctions are

called Ohmic contacts. However, for practical devices, obtaining Ohmic contacts is difficult because it is very hard to find metals and semiconductors combinations with the desired relation between Φ_m and Φ_s. For a real device, the semiconductor near surface is highly doped so that the depletion region between MS junction becomes very thin due to band bending and thermionic emission and field emission become dominant. This results in large current under forward and reverse biases due to the tunneling of carriers, and the MS junction behaves like an Ohmic contact.

For practical devices, it is very hard to vary Φ_b by changing Φ_s of contact metals due to Fermi level pinning at MS interface. The exact mechanism of Fermi level pinning is not clear, but it is believed to be related to surface imperfections such as surface defects, surface roughness, dislocations, and the presence of surface states. The impacts of surface states on Φ_b were explained by Bardeen [45] and also have been explained in Ref. [46].

1.6 Overview of the Thesis

This dissertation summarizes most of the research work done for my graduate study, which has been divided into 7 chapters. Chapter 1 includes brief introductions for each topic covered in the dissertation. Chapter 2 describes the experimental setup, characterization tools employed, and the device fabrication steps used for optoelectronic/nanophotonic devices studied here. AlN based DUV MSM photodetectors along with their characteristic properties are presented in chapter 3 and AlN based Schottky photodetectors grown on SiC and sapphire substrates are discussed in chapter 4, which also includes the results of AlN avalanche photodetectors. Chapter 5 discusses the photovoltaic characteristics of InGaN MQW solar cells. Emitters and optical waveguide amplifiers operating at 1.54 μm based on Er doped

InGaN/AlGaN for optical communication applications are discussed in chapter 6. Chapter 7 includes the general conclusions and suggestions for further work for some of the topics.

CHAPTER 2-Experiment: Growth, Fabrication and Characterization Techniques

2.1 III-nitride photonic devices: Growth

Metal organic chemical vapor deposition (MOCVD) has emerged as an efficient technological growth method for the deposition of high quality III-nitride semiconductors and device structures. All III-nitride based devices described in this work have been grown by Thomos Swan commercial and custom build MOCVDs. The Thomos Swan MOCVD has a rotating disk reactor in which 6 two inch wafers can be grown at a time, whereas the home built MOCVD has a horizontal reactor in which one quarter of a two inch wafer can be grown. Compared to the commercial MOCVD, the home built MOCVD has a larger dynamic range for growth temperature, pressure, etc. In the home built MOCVD, the growth temperature can be as high as 1350 ^{o}C, which is highly preferable for the growth of high quality AlN.

The main part of the MOCVD is a reactor in which the complex reaction of different gas precursors takes place. The gases are brought into the chamber locally and allowed to react on the surface of a heated substrate to grow thin film crystals as well as volatile gas-phase byproducts. The column-III precursors used for MOCVD growth of the devices described in this work are trimethylgallium (TMG), trimethylaluminum (TMA), and trimethylindium (TMI). Ammonia is used as the nitrogen source. A carrier gas, either H_2 or N_2, is bubbled though the metalorganic (MO) sources and carries the MO precursors to the reaction chamber. The ammonia nitrogen source is kept in a separate high-pressure gas cylinder and is brought to the reactor through a separate line. All gas flow rates are controlled by mass flow controller. The growth of device structures begins with a low temperature AlN or GaN buffer layer that is grown directly on sapphire or SiC substrates. The quasi-crystalline buffer layer becomes three-

dimensional islands when heated to high temperature and its main role is to eliminate the strain caused by the large lattice mismatch between III-nitride and foreign substrates like sapphire. As growth proceeds, the islands become bigger and coalesce, forming threading dislocations at the interface. The buffer layer is followed by the growth of a relatively thick (few μm in thickness) high temperature GaN or AlN template layer, which helps to reduce dislocations and provide a fully relaxed bulk layer for further device structure growth. N-type, active region like QWs, and p-type layers are then grown according to the particular device type and its design.

Due to the native defects and nitrogen vacancies introduced during epitaxial growth, as grown GaN under normal growth conditions is n-type with a typical background electron concentration of $\sim 10^{17}$ cm^{-3}. Si is a universal *n*-type dopant for III-nitrides which occupies the Ga site and becomes an electron donor. Silane (SiH_4) is a widely used precursor for Si doping in MOCVD growth. The activation energy of Si in GaN is very shallow (~17 meV) and thus highly *n*-type conductivity can be achieved easily at room temperature. The activation energy for Si increases as the Al content in AlGaN alloys increases and makes it relatively difficult to achieve highly conducting Al rich AlGaN alloys.

Achieving highly conducting *p*-type GaN is still challenging. The most common p-type dopant for GaN is Mg and its precursor for MOCVD growth is Bis(cyclopentadienyl)-magnesium. The Mg atoms are incorporated in Ga sites and become electron acceptors. The activation energy of Mg in GaN is relatively large (~160 meV) and thus Mg acceptors are not easily ionized at room temperature. Further, due to the hydrogen-rich atmosphere during epitaxial growth in MOCVD, Mg atoms form Mg-H neutral complexes during epitaxial growth. As a result, as grown Mg doped GaN is highly resistive. A thermal annealing is used to remove the hydrogen and activate the Mg dopant after finishing the MOCVD growth. The annealing

condition we have used in this work is 450 ^{o}C for one hour under air ambient. This relatively long annealing time at lower temperature is preferred due to the minimal damage caused to the InGaN active layer as compared to high temperature annealing for short times. The annealing process breaks the Mg-H bonds and promotes hydrogen diffusion out of the crystal.

2.2 III-nitride Photonic Devices: Fabrication

After completing the growth of device structures (PDs, LEDs, LDs, solar cell and waveguide structures) by MOCVD, the two inch wafer is generally divided into 1 cm x 1cm pieces. Device fabrication includes the following major steps.

I) Wafer cleaning: Device processing begins with the cleaning of the wafer in organic solvents in order to remove contaminants from the wafer surface. The wafer is dipped in a beaker with acetone, and placed in an ultra-sonic bath for 10 minutes. Then, the wafer is rinsed with acetone and isopropanol several times. Finally, the wafer is flushed several times with de-ionized (DI) water. After this step, the wafer is dipped in buffer oxide etch (BOE) solution for 1 minute to remove oxides from the surface, which is followed by DI water rinse and blown dry using N_2 gas. It is then immediately loaded in the e-beam evaporator to deposit semi-transparent p-contact (Ni/Au for LED, LD, solar cell) or Schottky contact (Pt for Schottky PD).

II) Mesa definition: In order to define the device size, mesa etching is employed since III-nitride material is mechanically hard and the wet chemical etching method cannot remove III-nitride materials appropriately. This material requires a combined physical and chemical etching in a plasma etching system to get a reasonable etching rate. To define mesa, first photoresist is spin-coated on the cleaned and dried wafer. The choice of photoresist (negative or positive) depends on the photo-mask design. The thickness of photresist depends on how long we want to etch. Throughout this work, we have used SHIPLEY S1813 (relatively thin) and S1045

(relatively thick) positive photoresists as an etch mask. After spin-coating (photoresist coating speed and time is determined by the thickness requirement), the wafer is soft-baked at 90 ℃ for 30 minutes. The wafer is then placed on the mask aligner and, using the photomask "mesa" layer, is exposed under DUV light. Then, the wafer is dipped in 319 photoresist developer for a few minutes (the developing time depends on photoresist thickness and exposure time). During development, photoresist exposed to light dissolves in solution while unexposed resist remains on the wafer, the reverse is true for negative photoresist. After inspection under optical microscope, the wafer is hard-baked in an oven at 90 ℃ for 10 minutes and then immediately loaded in inductively coupled plasma (ICP) chamber for dry etching. The slope of sidewall in mesa etching can be controlled by the hot-baking time of the photoresist. We have used $Cl_2/BCl_3/Ar$ (16/4/5 sccm) plasma for etching all samples. The etching rate for GaN is ~ 0.5 μm per min, (for AlN ~ 0.3 μm/min), which also depends on RF powers. The wafer is then removed from the ICP chamber and put in AZ 400 T photoresist stripper solution at 110 ℃ for 30 minutes to remove remaining photoresist and ICP byproducts from the sidewalls, which could be a source of leakage current in the device. Then, the sample is flushed with DI water several times and dried using N_2 gas. The sample is then placed in a thermal processer at 450 ℃ for 60 minutes under air ambient to activate the Mg dopants as well as p-contact annealing. This annealing process is performed after the mesa etching because it could help to remove etch-damage on the mesa sidewalls,which can be a source of leakage current.

III) Device passivation: ICP etch damage on the sidewall of a mesa can be another source of leakage current, which cannot be completely recovered even after high temperature annealing. A plasma enhanced chemical vapor deposition (PECVD) is used to deposit silicon dioxide (SiO_2) on the samples at 300 ^{o}C as a passivation layer, which also serves as an antireflection (AR)

coating for devices like solar cells and PDs. PECVD uses silane (SiH_4) and nitrous oxide (N_2O) gases to arc plasma and deposit SiO_2. This passivation layer is also very crucial for devices operating under high current injection (LD) and high electric field (APD). After SiO_2 deposition, a window is opened using photolithography and selective area wet etching of the SiO_2 layer to deposit p- and n-contacts.

IV) Ohmic contact formation: For optoelectronic devices such as LEDs, LDs, solar cells, p-n and p-i-n photodetectors etc, both n and p contacts for current injection should be high quality Ohmic contacts in order to enhance performance and extend the lifetime of the devices. Forming good Ohmic contacts is crucial in device fabrication. Making Ohmic n- and p-contacts for III-nitrides has been investigated by many groups. From earlier investigation, it has been observed that a multi-metal contact provides the lowest contact resistance. The most frequently used n-contact metals to n-type GaN, InGaN and AlGaN are Ti/Al, Ti/Al/Ti/Au, Ti/Al/Pt/Au, and Ti/Al/Ni/Au. As deposited n-contact to n-GaN and InGaN are good Ohmic contacts and requires no contact annealing. However, as deposited n-contact to Al rich n-AlGaN alloys is rectifying and requires high temperature rapid thermal annealing. We have used Ti/Al/Ni/Au metallization for n contact to n- GaN and AlGaN alloys for all works done here. A typical annealing condition for n contact (Ti/Al/Ni/Au) to n-$Al_{0.7}Ga_{0.3}N$ is 900 ^oC for 30 sec under N_2 gas ambient.

Achieving high quality Ohmic contact to p-GaN is challenging and becomes more difficult for AlGaN alloys. The contact metal must have as large a work function as possible due to the large bang-gap of $Al_xGa_{1-x}N$ alloys. The commonly used metals for p contact metallization to p-GaN are Ni (5.15 eV), Pd (5.12 eV) and Pt (5.58 eV). We have used Ni/Au for p contact metallization to p-GaN throughout this work. Rapid thermal annealing is employed to lower the

contact resistance. The annealing condition for Ni/Au contact to p-GaN is ~550 ^{o}C for two minutes under flowing O_2 (80%) and N_2 (20%) gases.

In order to deposit n- and p-contacts, standard optical photolithography and lift-off techniques have been used. First, bi-layer photoresists LOR 5A (coating condition: 3000 rpm for 40 sec and soft-baked at 175 ^{o}C on hot-plate for 5 minutes) and S 1813 (coating condition: 2000 rpm for 40 sec and soft-baked at 100 ^{o}C hot-plate for 1 minutes) were coated on dry and clean wafer. Then, the photoresist coated wafer is exposed to DUV light for about 8 sec using mask aligner and the appropriate photomask. The wafer then is developed in 319 photoresist developer solution for about 3 minutes, rinsed with DI water and dried using N_2 gas blow. Low power O_2 plasma is used for 1 minute to clean up thin photoresist remains (if any) in the window opening area. Then, the wafer is placed into the e-beam evaporator for metal deposition. After metal deposition, the wafer is placed in AZ 400T photoresist stripper to lift-off metals deposited in unwanted areas. Now, the devices are ready for testing using wafer probing. The details of the fabrication process for each device discussed in this work are explained in their respective chapters.

The tools employed to fabricate III-nitride photonic devices are: (a) **Mask aligner**: A deep UV lithography system from ABM Inc has a line resolution of 0.25 μm. We use 220 nm DUV mirrors for the smallest feature size photolithography, (b) **Inductively Coupled Plasma (ICP) etching system**: Our facilities include Plasma-Therm’s 790 series ICP system. It has been extensively used throughout the work reported here. We use $Cl_2/BCl_3/Ar$ plasma to etch III-nitride materials and CF_4/Ar plasma to etch SiO_2, and (c) **Electron Beam Evaporation Deposition System**: We use the Edward’s Auto 306 e-beam evaporator deposition system for

metallization. It has 4 target holders so that 4 different layers can be deposited at one run. Most frequently, we use Au, Al, Ti, Ni, SiO_2 targets. Typically, it operates at 5 x 10^{-7} torr pressure.

2.3 Facets preparation for III-nitride laser diode and waveguide amplifier

Facets preparation for edge emitting lasers and waveguide amplifiers in the GaAs and InP material systems is easy because there is a mutual cleavage plane for substrate and epilayers. Cleaving is a robust method for forming smooth, vertical facets and is thus a highly preferred method in most semiconductor system. However, the formation of facets in III-nitrides grown on sapphire is very difficult because sapphire does not cleave readily. Cleaving c-plane sapphire substrate is very difficult because sapphire has many cleave planes that have approximately equal cleave strength and are within a small angular distance. Therefore, it is likely to occur a fracture from one cleave plane being redirected to another by a small amount of surface roughness or a slight misalignment of the applied pressure, which is more likely to occur for thick substrates. Therefore, sapphire substrate has to be polished down thinner than 70 to 80 μm. However, sapphire is very rigid, making it difficult to thin. In addition, it cracks easily when it is lapped thinner than approximately 90 μm.

The growth of III-nitrides on c-plane sapphire substrates has matured. This presents a challenge for the fabrication of cleaved-facets for nitride lasers and waveguide amplifiers grown on c-plane sapphire substrates. Because of this difficulty, etched facets have been used for nitride lasers grown on c-plane sapphire substrates. Cleaved facets are the preferred mirror choice and are easier to manufacture than etched facets because they are less affected by processing variations such as temperature, gas composition, plasma density, acceleration voltage, and pressure. Besides, dry etching often leaves the surface rough and not completely vertical. Both of these facet characteristics reduce the useful reflection.

Facets preparation for III-nitride lasers and waveguide structures grown on c-plane sapphire by mechanical polishing is an alternative method. This method requires a relatively long time to obtain optically flat and vertical facets and is not be suitable for large scale production. We have prepared optically flat facets for GaN waveguides and laser structures grown on c-plane sapphire substrates by mechanical polishing. In this method, first the sapphire substrate is polished down to 200 μm and divided into a rectangular bar of about 2 mm in width. Two bars with devices grown with sides facing each other with no gap (need to press with each other using tweezers) in between them are mounted vertically on a specially designed sample holder using wax. Then the sample holder is mounted on a polishing machine in which the tilt angle and the downward force can be controlled precisely. Initially, diamond particles of 30 μm size were used. After that, the diamond particles of 3 μm were used for a few hours. Finally, the sample was polished in cotton pad using silica soap solution (silica particle size 250 nm) for several hours. After finishing one side the samples were lifted off and mounted again for polishing of the other face. Figure 2.1 (a) shows the optical microscope image of ridge waveguide laser facets prepared by mechanical polishing. AFM image scanned on the polished facet revealed that the surface roughness is less than 1 nm (Fig. 2.1 (b)) over the scan size of 10 x 10 μm^2.

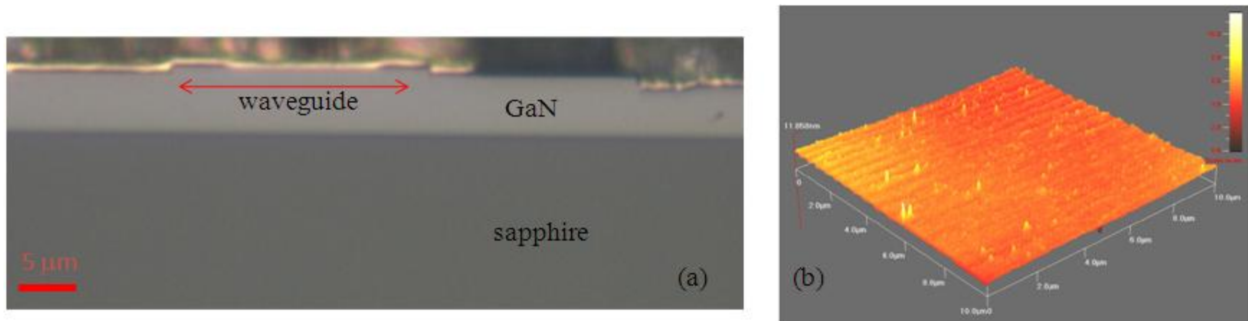

Fig. 2.1 (a) Optical microscopy image of laser facets prepared by mechanical polishing and (b) AFM image scanned on polished area which revealed surface roughness less than 1 nm for scan size of 10 x10 μm^2.

2.4 Highly Reflecting Dielectric DBR mirror preparation for LDs

Wide bandgap semiconductors have a relatively low refractive index. For example, GaN has a modal index of 2.5 in the visible wavelength region. The theoretical reflectivity for uncoated GaN/air interface is only 18% for a perfectly smooth facet. Further, the facet roughness can reduce the reflectivity significantly and increases the threshold current density for LDs. However, obtaining very smooth and vertical facets in GaN based laser structures grown on sapphire substrates is very challenging. In practice, almost all facets of III-nitrides grown on c-plane sapphire substrates prepared by dry etching, cleaving or polishing may have rough surfaces. None of these methods produces very high quality facets. The reflectivity of these facets can be improved significantly by depositing distributed Brags reflector (DBR) mirrors, which consist of a few periods of multilayer dielectrics with different refractive indices. The enhanced facets reflectivity decreases the threshold current density and hence increases the

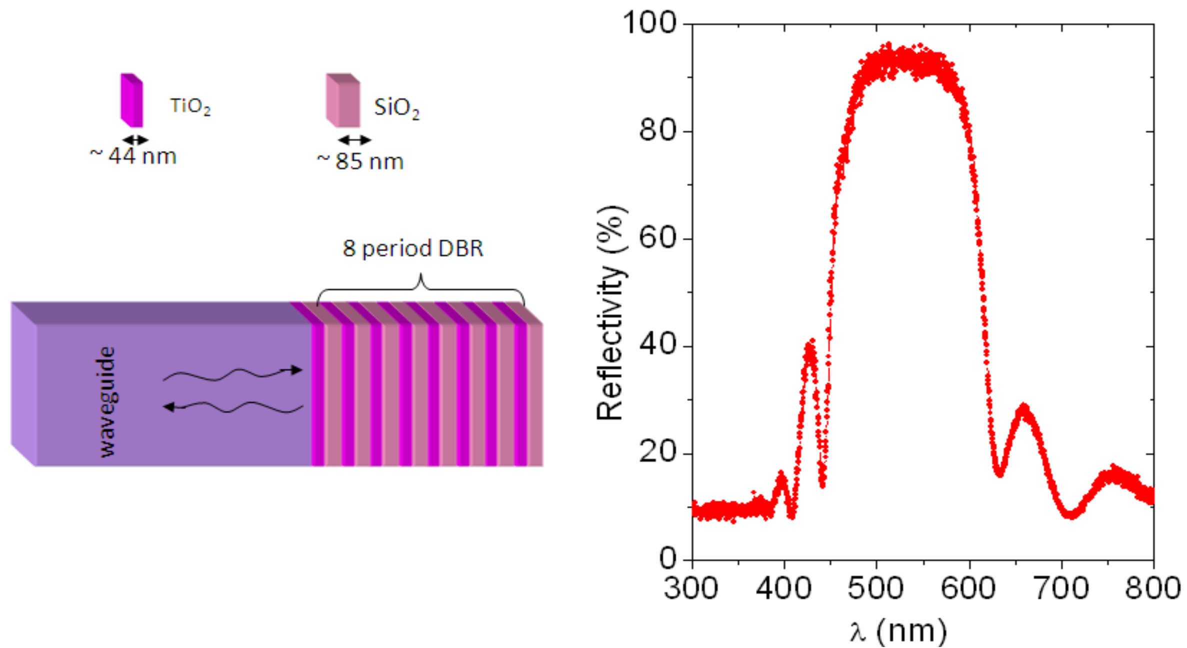

Fig. 2.2 (a) Schematic layer structure of SiO_2/TiO_2 DBR mirror and (b) reflectivity as a function of wavelength of 8 periods SiO_2/TiO_2 DBR mirror.

lifetime of LDs. The thickness of each dielectric layer should be equal to $\lambda/4n$, where n is the refractive index and λ is the wavelength at which maximum reflectivity is required. We have deposited 8 periods of SiO_2 (85 nm)/TiO_2 (44 nm) multilayers using e-beam evaporator. Thicknesses were calculated for λ=500 nm using the refractive index values of 1.48 and 2.90 for SiO_2 and TiO_2, respectively. The schematic layer structure of DBR mirror and its reflectivity spectrum are shown in Figs. 2.2 (a) and (b), respectively. The reflectivity is more than 90 % for between 500 to 600 nm. This DBR is very useful to reduce the threshold current density for InGaN based blue-green and green LDs.

2.5 Scanning Electron Microscopy (SEM)

Scanning electron microscope (SEM) is a very important tool for imaging and analyzing semiconductor materials and devices. Surface morphology and defects introduced in devices during fabrication can be analyzed at a very high magnification. The SEM used for this work is a LEO 440 SEM with accelerating voltage up to 40 kV interfaced with Nanometer Pattern Generating System (NPGS) for e-beam lithography and Oxford INCA Energy Dispersive X-ray Spectroscopy (EDX) to study the material composition and mapping. SEM can be controlled separately by INCA or NPGS software. Figure 2.3 shows the SEM interfaced with NPGS and EDX system.

Fig. 2.3 Photograph of SEM interfaced with NPGS (for e-beam lithography) and EDX (for composition determination) system located in our lab.

Conventional optical microscopes use a series of glass lenses to bend light waves and create a magnified image. The SEM creates the magnified images by using electrons instead of light waves. An electron gun located at the top column chamber emits a beam of high energy electrons which travel downward through a series of magnetic lenses designed to focus the electrons to a very fine spot. Near the bottom, a set of scanning coils moves the focused beam back and forth across the specimen, row by row. As the electron beam hits each spot on the sample, secondary electrons are emitted from its surface. A detector counts these secondary electrons and sends the signals to an amplifier. The final image is built up from the number of electrons emitted from each spot on the sample. The resolution of an optical microscope is

limited to (~350 nm) by the light wavelength. SEM shows very detailed 3-dimensional images at much higher magnifications than that is possible with a light microscope. This is because the deBroglie wavelength of electrons at this energy is less than 1 A^{o} and in principle, SEM resolution is only limited by this wavelength. The images created without light waves are rendered black and white. Figures 2.4 show SEM images of (a) as grown GaN surface showing defects, (b) fabricated strip waveguide laser, and (c) magnified but tilted view of sidewall of a waveguide prepared by ICP dry etching.

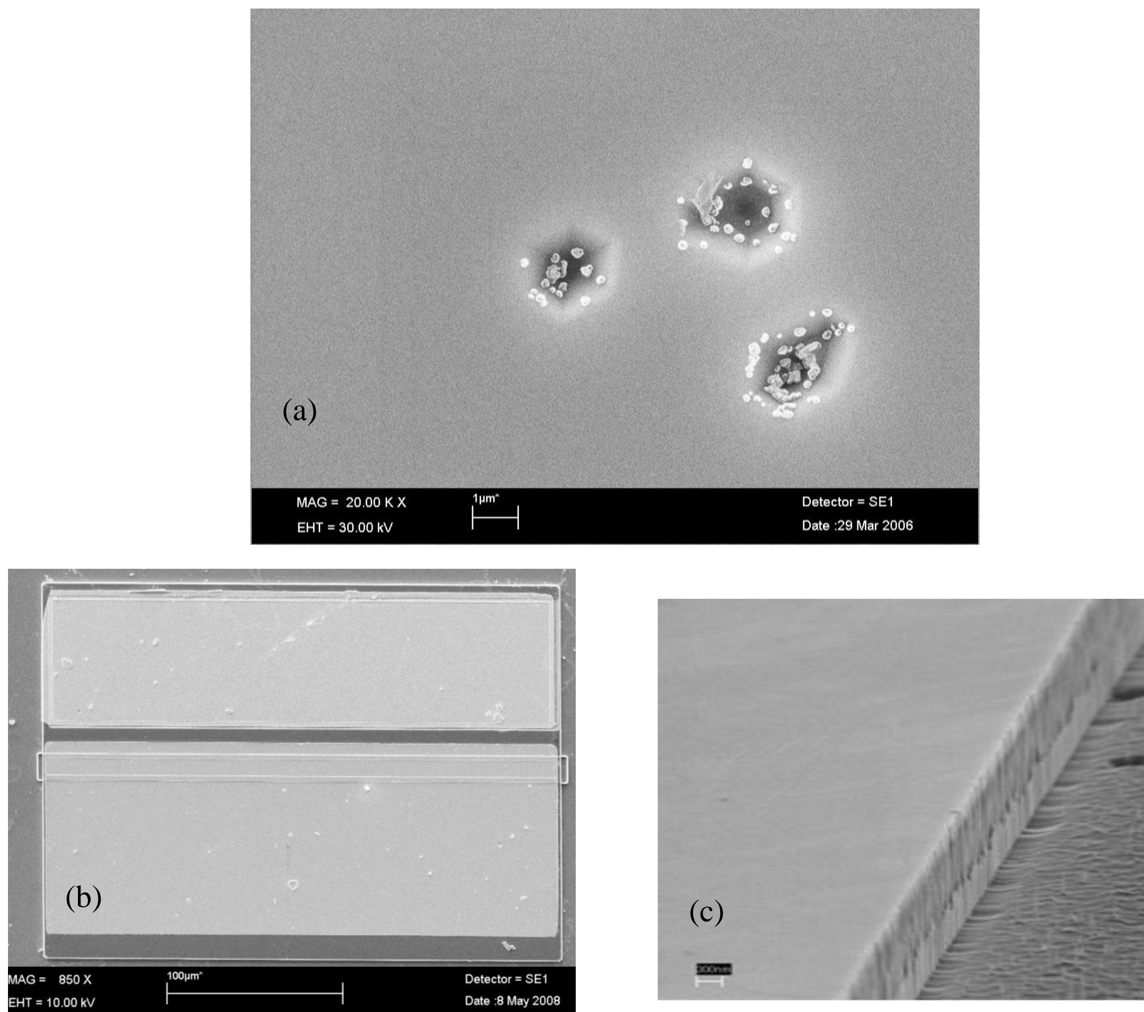

Fig. 2.4 SEM image of (a) as grown GaN surface showing the defects, (b) top view of fabricated LD, and (c) magnified and tilted view of side wall of dry etch waveguide.

SEM combined with NPGS from JC Nabity has been used for e-beam lithography. NPGS system is basically an extra computer loaded with NPGS software to control scanning of electron beams in SEM to write a desired pattern directly on the sample without using any mask as in optical lithography. E-beam lithography uses high energy electron beams rather than ultraviolet (UV) light to define features in the sample. To make pattern by e-beam lithography, first the sample surface is coated with "e-beam resist" a few hundred nanometers in thickness. Then the desired area of the sample, defined by the CAD pattern, is exposed to a high energy electron beam (~ 30 keV) inside the SEM. The e-beam exposed area of the sample undergoes a chemical change. Just like photographic film development, the sample is then "developed" by dipping in a chemical developer which washes out the soluble part of the coated film. A "positive" resist is one which is washed out during development if it has been exposed to the e-beam. The reverse is true for "negative" resist. Thus the sample is patterned with e-beam resist with the desired features on it. These patterns are then transferred to the sample either using dry/wet etching or deposition/lift-off techniques. NPGS can produce patterns from nanometer size up to the microscope field of view. The minimum feature size of patterns is limited by the resolution of SEM and its stability over the pattern generation period. Figure 2.5 shows an SEM image of photonic crystal (PC) patterns with e-beam resist after development.

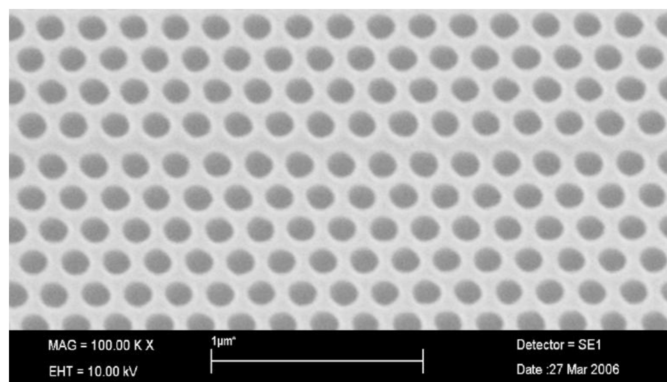

Fig. 2.5 SEM image of PC patterns written by e-beam after development in e-beam developer.

2.6 Atomic Force Microscopy (AFM)

Atomic force microscopy (AFM) is a high resolution surface profiling technique well established for the study of surface morphology and nanometer size features. The AFM probe (a sharp tip) is placed on a flexible cantilever on which a laser is focused to monitor the deflection of the cantilever. AFM systems map the deviations of thin film surfaces by detecting the deflection of the laser as it is scanned over the film surface. With the appropriate cantilever choice and feedback controls, AFM is capable of z-height resolution on the order of angstroms. AFM we have employed in this work is a Quesant Q-scope 250 systems capable of operating in both non-contact and contact modes with a z-height resolution of 0.5 nm. For hard semiconductor surfaces, it is always operated in contact mode, while for soft surfaces it is operated in non-contact mode. It scans a maximum area of 50 x 50 μm^2 and upto 6 µm in height. Figure 2.6 shows AFM images of (a) surface morphology of GaN after wet etching in phosphoric acid and (b) Er doped GaN waveguide.

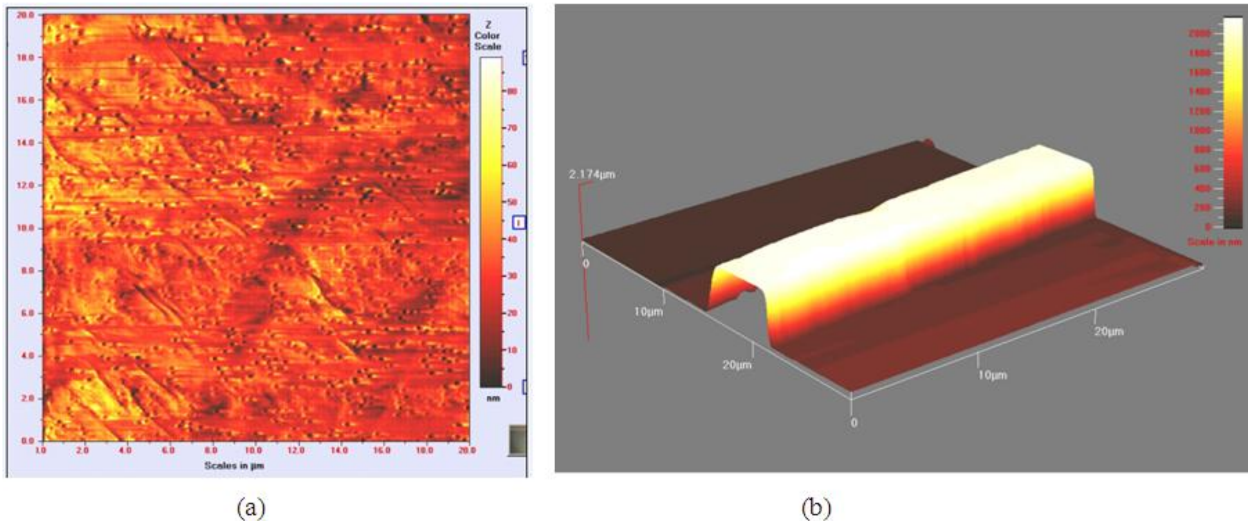

Fig. 2.6 AFM image of (a) GaN surface after wet etching using phosphoric acid showing etch pits and (b) a fabricated GaN waveguide.

2.7 Electroluminescence, Current-Voltage, and Light-Current Measurements

Electroluminescence (EL), the emission of light in response to applied current or strong electric field in semiconductor materials, comes from the radiative recombination of electron-hole pairs near the band-edge of the material or from impurities/defects present in the material. Figure 2.7 shows an actual photograph of a micro probe station set up in our lab, which is capable of measuring EL, I-V and L-I characteristics of LEDs and LDs. A variable bias and current was applied to the devices from a Keithley 2400 source meter. This set up also has a pulse generator (Agilent 8114A) used to supply power to the LD and has the capability to vary pulse width from 10 to 500 ns and period from 20 ns to 1 sec. This system is equipped with Nikon eclipse ME 600 microscope fitted with CCD camera. The microscope is used for device

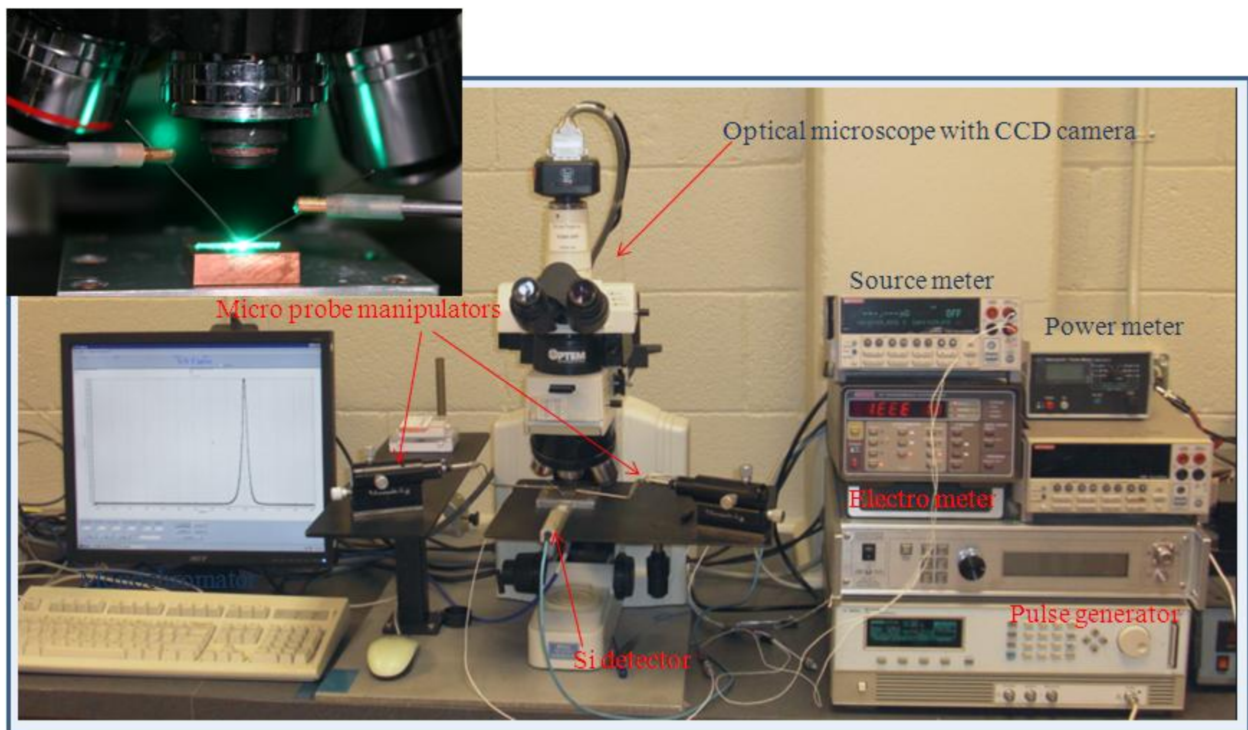

Fig. 2.7 Photograph of micro manipulator probe station equipped with optical microscope and CCD camera for measuring I-V, L-I and EL characteristics of LEDs, LDs, PDs, and solar cells. The inset is the photograph of a green LD probied using this set up.

positioning and probing at the surface. EL emission to detection system was transferred by an ocean optics USB 2000- mixed bifurcated fiber (200-800 nm). The inset in Fig. 2.7 shows the probing of a green LD.

2.8 Photoresponse Measurements for Photodetectors

In order to study the photoresponse characteristics of photodetectors, monochromatic light with wavelengths varying from below to above the bandgap of active photodetector materials is needed. When incident light with energy greater than the bandgap of semiconductor strikes the surface of the photodetector, electron-hole pairs are generated that are separated by applied external bias and flows as a current in the external circuits. The current in the photodetector in the absence of incident light is the leakage or dark current.

For UV photodetectors based on AlGaN semiconductors, the dark current is extremely small (in order of fA) due to a wide energy bandgap. Therefore, measurement system for such a small current should be designed carefully to minimize the interference from surroundings. All the connecting cables used for these experiments were triaxial and the connectors were also triaxial BNC connectors. Figure 2.8 shows an actual photograph of the set up, which includes all the required equipments. Light from a 150 W deuterium light source incidents on a triple grating of monochromator (SpectraPro 2300 i from Action Research Corp.), which disperses it into light of different wavelengths. The resolution of the monochromator is 1 nm. The photocurrent in photodetector corresponding to incident monochromatic light is measured by Keithley 617 electrometer and the bias to the photodetector is provided by Keithley 2400 source meter. This set up is also capable of measuring I-V characteristics with applied voltage up to 1000 V. This system has also been used to measure the absorption spectra of InGaN/AlGaN epilayer grown on sapphire substrates. For absorption measurement, the intensity of transmitted light through thin

films is measured by using a photo-multiplier-tube (PMT). To calculate the responsivity and quantum efficiency of PDs, spectral photocurrent is normalized by spectral incident light intensity and device area. All these equipments are computer controlled and data is recorded by a computer.

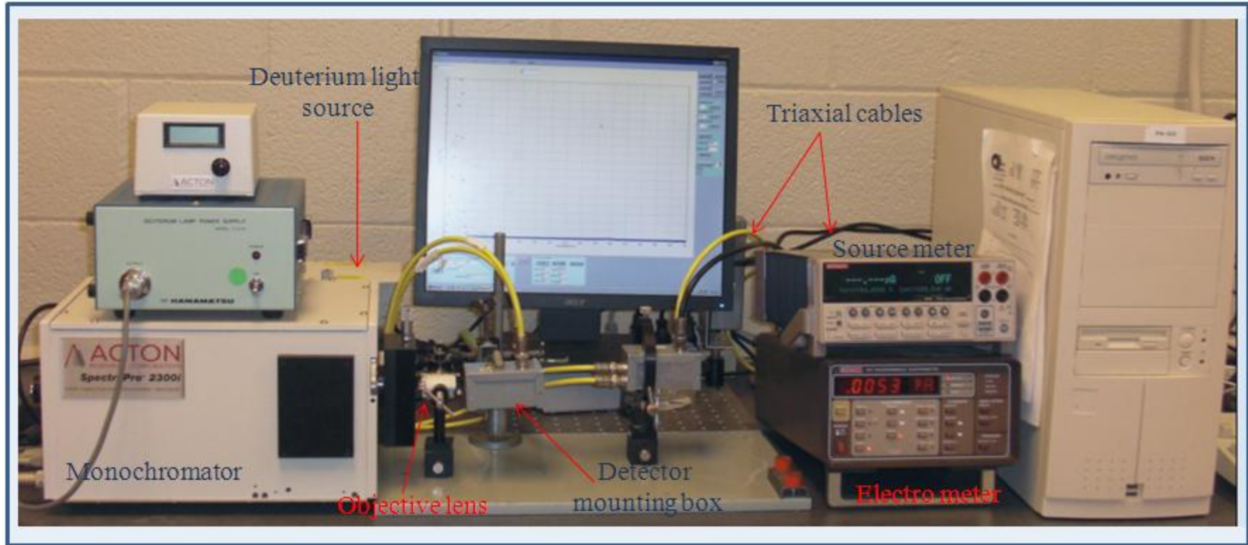

Fig. 2.8 Photograph of measurement set up for I-V and photoresponse of DUV photodetector located in our nanophotonic lab. This set up is also capable of measuring absorption spectra of thin film semiconductors.

2.9 Other Characterization Techniques

I) XRD is a very important technique to study the crystalline quality and defects of thin film semiconductor materials. It was used to measure the rocking curve of (002) and (102) plains of AlN. Our XRD (Rigaku RINT 2000V/PC series) can make 2Θ/Θ coupled scan and Θ or 2Θ individual scans. With new designed stage it can measure the rocking curve line width in (002), (103) and (102) directions with a resolution of 100 arcsec. The diffraction of an x-ray beam by a crystal is given by the Bragg's reflection law of $2d\sin\Theta = n\lambda$, where d is the spacing between the reflecting planes, Θ is the diffraction angle, and n is the order of the corresponding reflection.

The measured 2Θ angle varies from -10° to 158°. The source of x-ray is Cu and the wavelengths are 0.154056 nm and 0.154439 nm for CuK $_{\alpha 1}$ and CuK $_{\alpha 2}$, respectively.

II) **Photoluminescence (PL) spectroscopy:** PL spectroscopy is a very powerful and fundamental technique to determine the optical properties of semiconductor materials in a non-destructive and highly precise manner. In PL spectroscopy, photo-excitation by incident light (typically laser) causes the electrons to move within the material into allowed excited states. When these electrons return to their equilibrium states, the excess energy is released either through a radiative process (emission of photon) or a non-radiative process (phonon). The wavelength of the emitted light is the characteristics of levels involved in the transition between the excited state and the equilibrium state. The intensity of the emitted light is related to the relative contribution of the radiative process. Information about both the fundamental optical band edge transition and impurity or defect related transitions of semiconductor can be measured by PL directly and precisely. The deep UV laser system utilized in these experiments consists of 100 femtosecond Ti-sapphire laser (76 MHz repetition rate, λ=788 nm) with frequency quadrupled wavelength 197 nm (average power 5 mW), frequency tripled wavelength 263 nm (average power 20 mW), and frequency doubled wavelength 394 nm (average power 100 mW). This laser system allows us to measure optical processes in III-nitride materials in wavelengths spanning all the way down to the band edge emission of AlN ~ 200 nm.

CHAPTER 3-AlN MSM Photodetectors

3.1 Metal-semiconductor-metal Photodetectors

Metal-semiconductor-metal (MSM) photodetectors (PDs) are planer devices consisting of two interdigitated, finger like, Schottky barrier rectifying contacts deposited on top of an intrinsic semiconductor layer (light absorption layer). A typical structure of MSM PD is shown in Fig. 3.1. MSM PD has been established as an important optoelectronic device because of

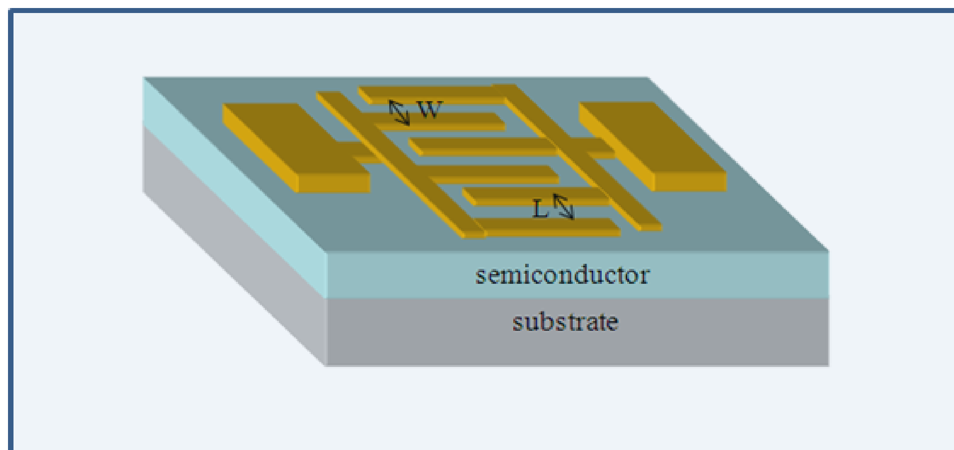

Fig. 3.1 Schematic diagram of MSM photodetector.

planer and simple device structure (easy for fabrication), high electrical bandwidth, high sensitivity, and compatible for large-scale planar integrated circuit technology [47-50]. The planer structure of MSM PDs is also advantageous for its integration with emitters and amplifiers. MSM PD works only under external bias which depletes the semiconductor between metal fingers as well as underneath the contacts. Since both contacts are rectifying, under external bias one junction is forward biased and the other is reverse biased. In the absence of incident light, the saturation current of the reverse-biased junction governs the device current which is called dark current, I_d. I_d depends not only on the crystalline quality of semiconductor, but also on the barrier formed at the metal-semiconductor interface. The dark current is small for

PDs with higher Schottky barrier heights. For MSM PD consisting of smaller band gap semiconductors such as Si or InGaAs, the extremely low Schottky barrier height with almost all metals requires the incorporation of a thin barrier enhancement layer with higher band gap energy, which helps to reduce the I_d. However, special care has to be taken about the extra potential drop in external current path due to the barrier height enhancement layer. An obvious advantage of MSM PDs based on wide band gap semiconductors like III-nitride (AlGaN) over narrow band gap semiconductor based PDs is the formation of a relatively large Schottky barrier height (for metals such as Au, Pt, and Pd etc) at the metal-wide bandgap semiconductor junction.

The incident photons with energy greater than the band gap of the active layer generate electron-hole pairs (EHPs), which are swept by fringing electric fields and collected by metal contacts, thereby generating an electric current in the external circuit. The speed and responsivity of PDs depend on the transit time and the number of photo-generated carriers that are able to reach the electrodes, within a specific time, respectively. The important parameters of MSM PDs are responsivity, speed, and dark current [46, 51, 52]. The relative importance of each parameter depends on the type of application, and they are not independent of each other. For instance, by changing the absorbing layer width of a detector whose bandwidth is limited by transit time, one can increase the bandwidth at the expense of responsivity.

3.2 Dark Current in MSM Photodetectors

The energy band diagram of MSM diode under applied voltage V is shown in Fig. 3.2. In principle, the dark current of MSM PD is determined by thermionic emission over the Schottky barrier. Under low bias voltage, electron injection at reverse-biased junction is the dominant conduction mechanism, however with increasing applied bias, hole injection at forward-biased junction also becomes significant and tends to dominate when the two depletion edges

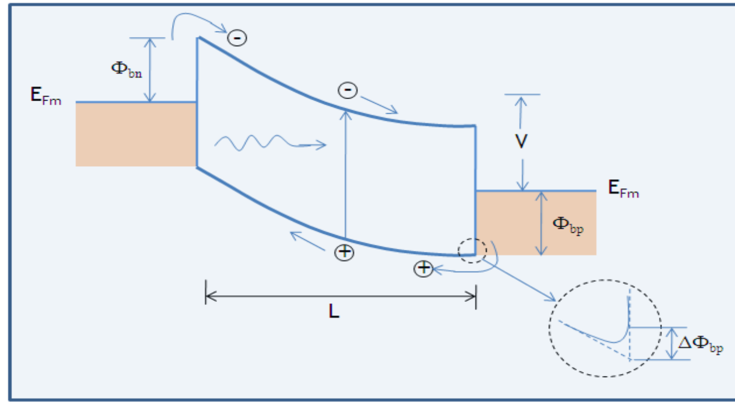

Fig. 3.2 Energy band diagram of metal-semiconductor-metal junctions.

corresponding to two adjacent metal fingers coincide (reach-through condition). The total current density under these conditions is given by

$$J = A_n^{**}T^2 e^{-q(\Phi_{bn}-\Delta\Phi_{bn})/k_B T} + A_p^{**}T^2 e^{-q(\Phi_{bp}-\Delta\Phi_{bp})/k_B T} \tag{3.1}$$

where A^{**}s are respective Richardson constants, Φs and ΔΦs are respective barrier heights and barrier height lowering due to image force as shown in the inset of Fig. 3.2. From Eq. 3.1 it is seen that the dark current is small for PDs with higher Schottky barrier heights.

3.3 Responsivity of MSM Photodetectors

The interdigitated electrode geometry is almost universally utilized for MSM PDs which provides lower device capacitance, but introduces the shadowing effect by blocking incident light from absorption in the active medium (depletion region). This reduces the external quantum efficiency, η, of the device by a factor associated with the fill factor

$$F = \frac{W}{L+W} \tag{3.2}$$

where L and W are the spacing between adjacent fingers and the width of the finger, respectively. However, using the semi-transparent metals (5-10 nm Au, Pt or Pd), the shadowing effect can be minimized. In contrast to photoconductive detectors (both electrodes are Ohmic

contacts) which have photoconductive gain, the Schottky barrier in MSM PDs preclude the reinjection of electron-hole pairs, which prevents the photoconductive gain and limits the internal quantum efficiency, η_i, unity or less for ideal MSM PDs. However, in real devices, surface states, defect or dislocations mediated gain mechanisms can occur due to the presence of high electric fields along the semiconductor surface in interdigitated metal contacts. Another gain mechanism could arise from image force lowering effects due to charge accumulation at potential barriers. The dynamics of these defects assisted gain are quite slow, which present obstacles for utilizing this mechanism to enhance responsivity of the device. In defect–free materials where these gain effects are absent, assuming the top-side illumination and opaque electrodes, the responsivity of MSM PD with active layer thickness, d, and absorption coefficients, α, in the reach-through condition (when the semiconductor between metal fingers is fully depleted) is given by

$$\mathcal{R} = \left\|\frac{I_{ph}}{P_{in}}\right\| = \frac{q\lambda}{hc}(1-R)\eta_i\left(1-e^{-\alpha d}\right)(1-F)$$

$$\mathcal{R} = \frac{\eta_i\lambda(\mu m)}{1.24}(1-R)\left(1-e^{-\alpha d}\right)(1-F)$$

$$\mathcal{R} = \frac{\eta\lambda(\mu m)}{1.24}\ \frac{A}{W} \tag{3.3}$$

where R is the reflectivity of semiconductor-air interface, which can be minimized by depositing anti-reflection coating (AR) to enhance responsivity. In accordance with Eq. (3.3), for an ideal case, $\Re$ should increase linearly with λ for fixed η, however for real devices, η depends upon α which in turns depends on λ of incident light. Therefore the long side cut-off wavelength, λ_c of spectral response is determined by the absorption band edge or band gap of the semiconductor which is given by

$$\lambda_c = \frac{1.24}{E_g\,(eV)} \quad (\mu m) \tag{3.4}$$

For PDs based on direct band gap semiconductors without any defects, the spectral cut-off is expected to be sharp. However, the presence of defects and impurities in the band gap of the semiconductor gives the unwanted below band gap spectral response whose dynamics is also quite slow and imposes potential obstacles in the usefulness of the device. In short wavelength regime, the value of α is very large for most semiconductors and all the incident light is absorbed near the surface which decreases the responsivity of p-n and p-i-n PDs in the short wavelength region. However, for MSM PDs, the depletion region is well extended up to the surface and hence the responsivity is expected to be nearly constant well above the band gap of the semiconductor.

3.4 Band Width and Speed of MSM PDs

For semiconductor based photodetectors, only photons with energies greater than the band gap of the semiconductor are able to generate electron-hole pairs. The electronic response of the detector following electron-hole pair generation is governed by the drift and diffusion of charge carriers in the semiconductor, which usually depends on the design and structure of a particular photodetector. Besides it also related to the optical and crystalline quality of the semiconductor material. Photodetecors suitable for high speed applications are generally based on junction diode which basically depends on the electron-hole pairs generated within the depletion region, and in some cases on the photo-generated carriers within the diffusion length of the depletion region. Photo-generated carriers within the depletion region are swept by the electric field due to applied bias or built-in potential, while carriers generated outside the depletion region first should diffuse in the depletion region before being swept through the

depletion region. The movements of these photo-generated carriers give rise to a transient displacement current in the diode terminals and also contribute a drift or conduction current. Therefore, the intrinsic speed of the junction based photodetector is determined by the drift and diffusion processes. The diffusion process degrades the photodetector's speed; however, the diffusive component can be minimized or eliminated through device design for enhanced device speed. The speed of a detector is also limited by extrinsic effect such as RC time constant, (R external load resistance and C the capacitance of photodiode) of the circuit. For real devices design, both extrinsic and intrinsic factors must be considered when both mechanisms are comparable in time scale.

In MSM PDs, the electric field distribution associated with an interdigittated contacts geometry exhibits significantly low capacitance, which provides the possibility of a larger RC-limited bandwidth. In addition, MSM PDs are primarily lateral carrier transport devices, which allow the control of carrier transit time by interdigitated finger spacing defined by lithography while quantum efficiency is controlled independently through epitaxial layer design.

3.5 AlN based deep UV MSM PDs

Considering the requirements and constrains for space applications-reliability, radiation hardness, light weight, and minimal power usage; the next generation of space observatories require orders-of-magnitude performance advances in detectors and enabling technologies. AlN appears to be an ideal material for the development of deep ultraviolet (DUV), vacuum UV (VUV), and extreme UV (EUV) detectors because AlN possesses the widest direct energy band gap (~6.1 eV) among all semiconductors and offers the ability for band gap engineering through the use of alloying and heterostructure design. AlN detectors would help to circumvent many of

the limitations imposed by Si technology. The 6.1 eV band gap permits the visible background to be intrinsically suppressed and the detectors to operate at room temperature, which drastically relieves the harsh requirements of optical filters and cooling hardware and greatly simplifies system design. The compact crystal network of AlN inherently provides radiation hardness. We have previously demonstrated that AlN epilayers with an optical quality comparable to GaN can be grown on sapphire by metal organic chemical vapor deposition (MOCVD) [53-55]. Due to its high thermal conductivity and transparency in the DUV spectral range (λ>200 nm), AlN epilayers have been widely employed as templates for the development of DUV light emitting diodes (LEDs) with emission wavelengths λ<300 nm [56-61]. Several groups have also made significant progress toward the realization of conductive AlGaN alloys with high Al contents [62-65]. Most recently, LEDs based upon pure AlN with an emission wavelength of 210 nm have been demonstrated [15]. These recent progresses have demonstrated the high promise of AlN as an active material for DUV optoelectronic device applications. Many groups have previously demonstrated UV photodetectors based upon AlGaN alloys with superior performance [66-77]. However, the shortest cutoff wavelength achieved with AlGaN so far is 229 nm [33]. In this work, we report on the growth and exploitation of pure AlN for DUV photodetector fabrication. We have demonstrated the operation of 200 nm DUV photodetectors through AlN metal-semiconductor-metal (MSM) photodetectors with very high DUV to visible rejection ratio.

3.6 AlN epilayer Growt and Characterization

Undoped AlN of about 1.5 μm thick were grown by MOCVD on sapphire substrates. The sources of Al and N are trimethylaluminium (TMAl) and blue ammonia, respectively. For UV detector applications, the presence of impurities will decrease the UV to visible rejection ratio. We employed deep UV photoluminescence (PL) spectroscopy to investigate the optical

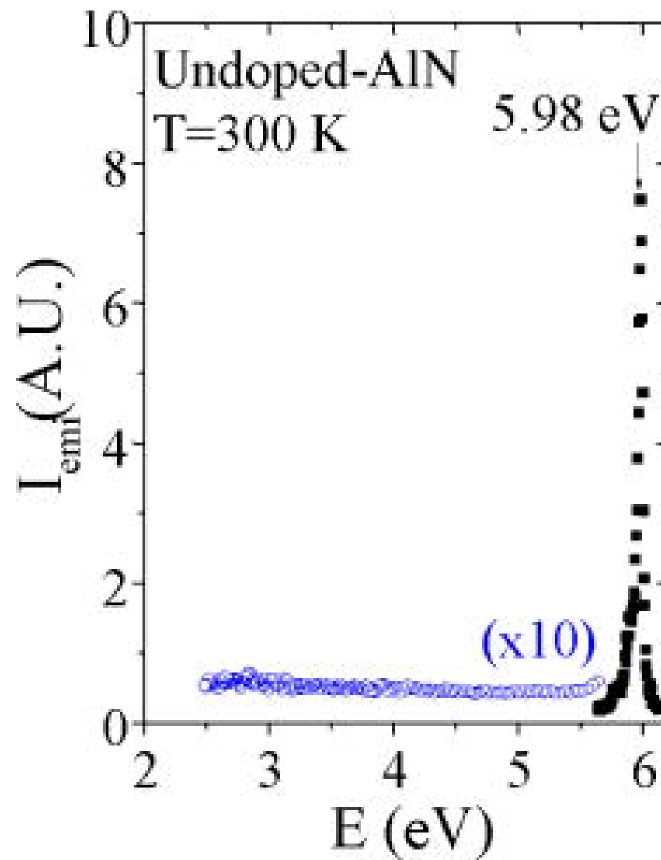

Fig. 3.3 Room temperature photoluminescence spectrum of an AlN epilayer used in this study.

properties of AlN epilayers. Figure 3.3 shows a typical room temperature PL emission spectrum of an undoped AlN epilayer under a 197 nm DUV laser excitation. The PL spectrum was collected in surface emission mode and the average excitation power density at 197 nm is on the order of 100 W/cm^2. The spectrum consists of a very strong band edge emission line with no visible impurity transitions, ensuring very good optical quality and high purity in the material. The dominant emission line at 5.98 eV is due to the recombination of free excitons, which have a binding energy of about 55-75 meV in AlN [53-55].

In general, the presence of a high density of dislocations will also degrade the performance of detectors such as high leakage currents. We use x-ray diffraction (XRD) measurements to evaluate the crystalline quality. For wurtzite AlN, high density of screw

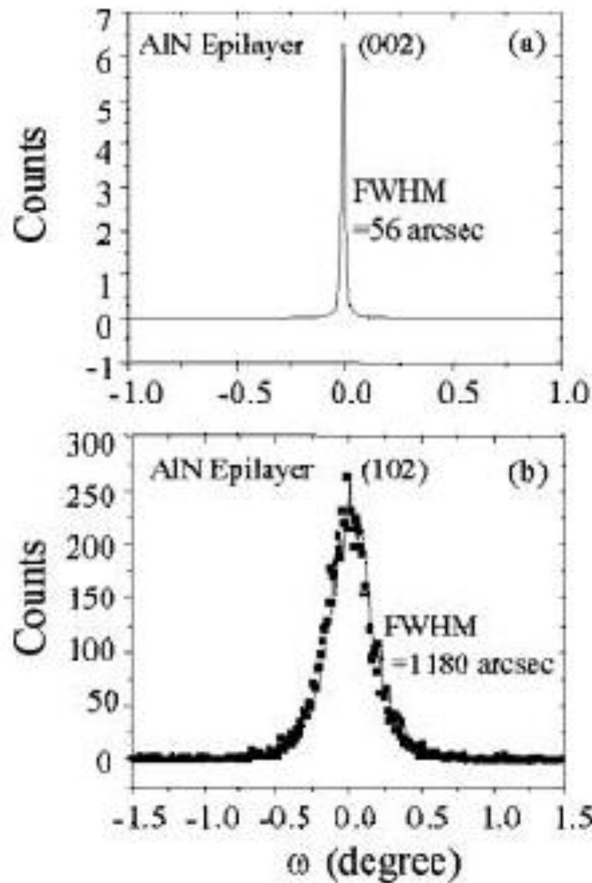

Fig. 3.4 X-ray diffraction ω scans (rocking curves) of the (a) symmetric plane (002) and (b) asymmetric plane (102) of an AlN epilayer used in this study

dislocations will result in a broadening of the full width at half maximum (FWHM) of symmetric x-ray scans, such as the (002) rocking curve. However, the majority of dislocations in AlN are of edge type, which primarily distorts the asymmetric planes, such as (102). Figures 3.4 (a) and (b) show, respectively, the XRD scans (rocking curves) of symmetric plane (002) and asymmetric plane (102) of an AlN epilayer used in this study [78-79]. The results show that the FWHM of the (002) reflection peak is quite narrow (~50 arcsec), while the (102) reflection peak (~1200 arcsec) is broader than those of high quality GaN epilayers grown on sapphire (< 400 arcsec). The estimated screw and edge dislocation densities were about 5×10^{7} and 4×10^{9} cm^{-2},

respectively, which indicates that there is still a lot of room for further improvement in terms of the edge dislocation density reduction.

The surface morphology of the AlN epilayer used to fabricate MSM photodetector was characterized using atomic force microscopy (AFM). Figure 3.5 is an AFM image of as grown AlN epilayer. The root mean square roughness of AlN epilayer over the scan size of 10 x10 μm^2 was ~ 0.8 nm. In order to study the presence of defects or dislocations in AlN, we used

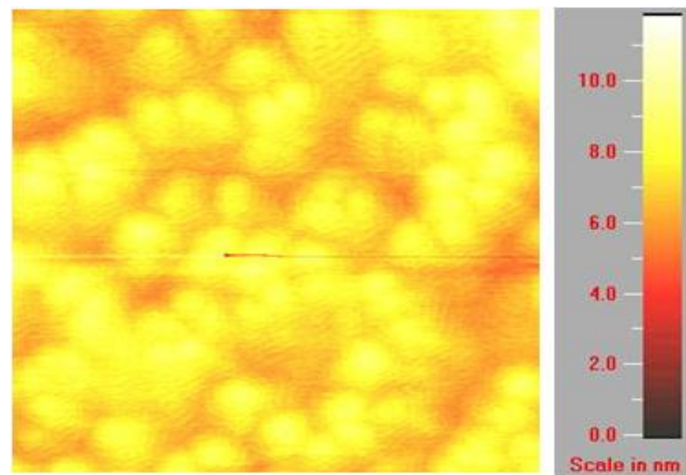

Fig. 3.5 Atomic Force Microscopy image (10 x 10 μm^2) of as grown AlN.

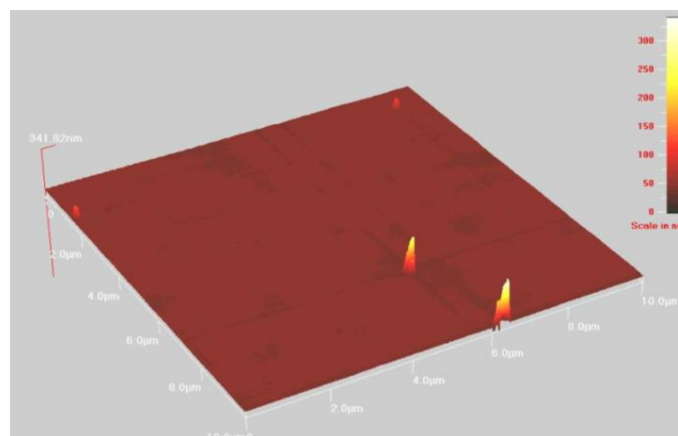

Fig. 3.6 Atomic Force Microscopy image (10 x 10 μm^2) of etched AlN epilayer.

inductively coupled plasma (ICP) to etch down the AlN epilayer by about 250 nm using $Cl_2/BCl_3/Ar$ plasma. The AFM image of the etched surface is shown in Fig. 3.6. The etch pit density in our AlN epilayer was ~ $4x10^6$ cm^{-2}.

3.7 AlN MSM PDs Fabrication

The device fabrication process consists of the following steps. First, samples were cleaned using acetone, isopropanol and ultrasonic-bath followed by several de-ionized water rinses and drying by N_2 gas. Photolithography was used to define interdigitized Schottky contact area. After photolithography, the sample was dipped in BOE solution for 30 sec followed by de-ionized water rinse and then immediately loaded into e-beam evaporator. A 10 nm Pt was deposited at a base pressure of ~$1x10^{-7}$ torr followed by lift-off in photoresist stripper. Then,

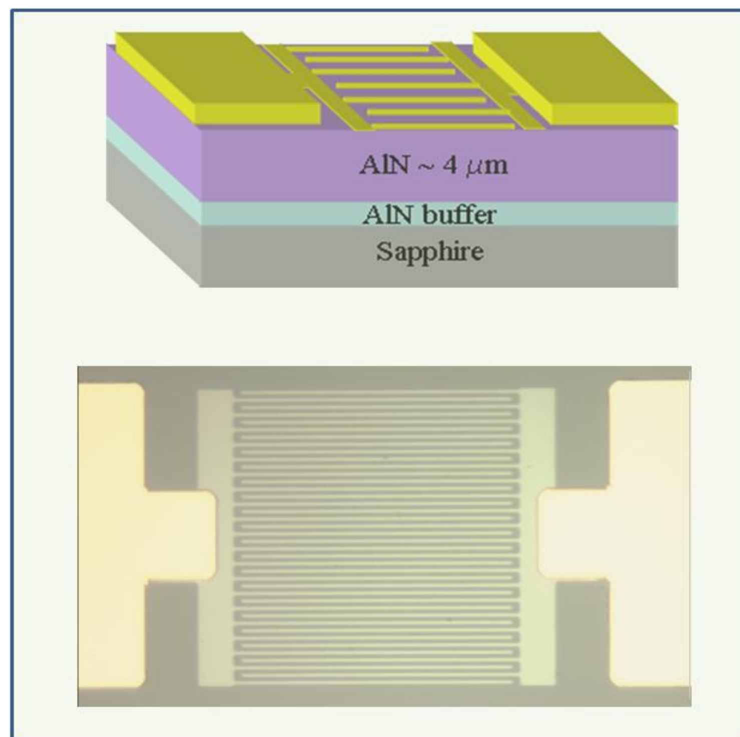

Fig. 3.7 (a) Schematic layer structure and (b) optical microscopy of fabricated AlN MSM PD, image of device with 80 x 80 μm^2 active area having finger width and spacing of both 1 μm.

bonding pads were formed using photolithography and e-beam evaporation of 20 nm Pt and 200 nm Au followed by lift-off in photoresist stepper. The schematic layer structure and optical microscopy image of MSM detector are shown in Fig.3.7 (a) and (b), respectively. Finally, the wafer was back polished, thinned down to ~ 100 μm and diced into discrete devices, which were bonded in 10 pin ceramic flatpack for characterization.

3.8 AlN MSM PDs Characterization

The first step to characterize MSM PD is to study the I-V characteristics in the absence of light. The typical dark *I-V* characteristics of AlN based MSM detectors are shown in Fig. 3.8. The dark current for these devices are below 100 fA up to a bias voltage, $V_{b,}$ of 300 V. The devices showed a breakdown voltage greater than 320 V. Beyond 320 V, the dark current increased very

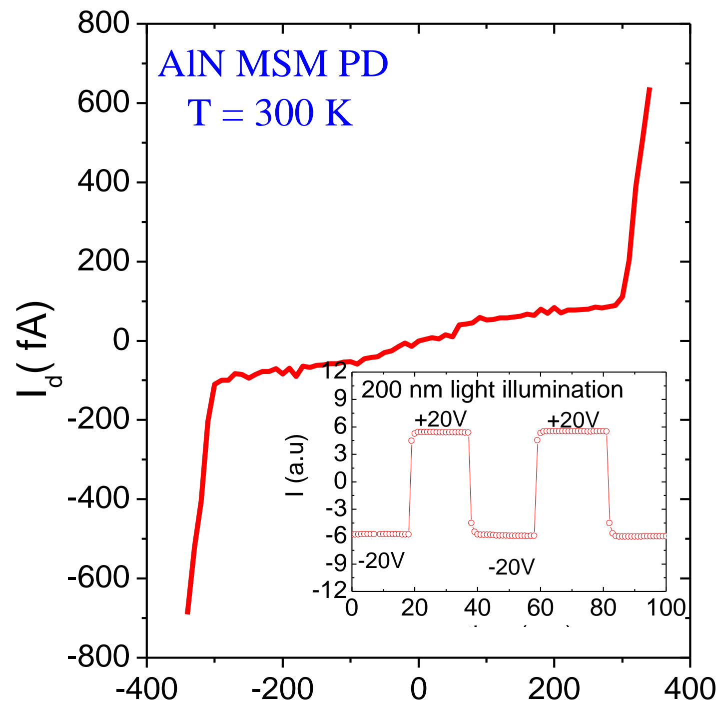

Fig. 3.8 Dark I-V characteristics of AlN MSM photodetector. The inset shows the signal stability of AlN MSM PD at V_b = -20 and + 20 V, respectively under 200 nm light illumination.

sharply, which damaged the devices. We also studied the photocurrent stability of the device under 200 nm light illumination by switching the bias voltage between -20 and + 20 V (for example), respectively. The result is shown in the inset of Fig. 3.8 which indicated that the signal is stable and that the magnitude of signal is almost the same under both conditions. MSM PD is a symmetrical device and an equal magnitude of signal for opposite biases is expected. The result shown in the inset of Fig. 3.8 also indicated that there is no persistent photoconductivity in AlN MSM PD.

Figure 3.9 Shows the I-V curves in semi-log scale in dark (solid line) and with 200 nm light illumination (- ●-●-) up to V_b =200 V. The photocurrent at V_b = 10 V is about 0.3 nA,

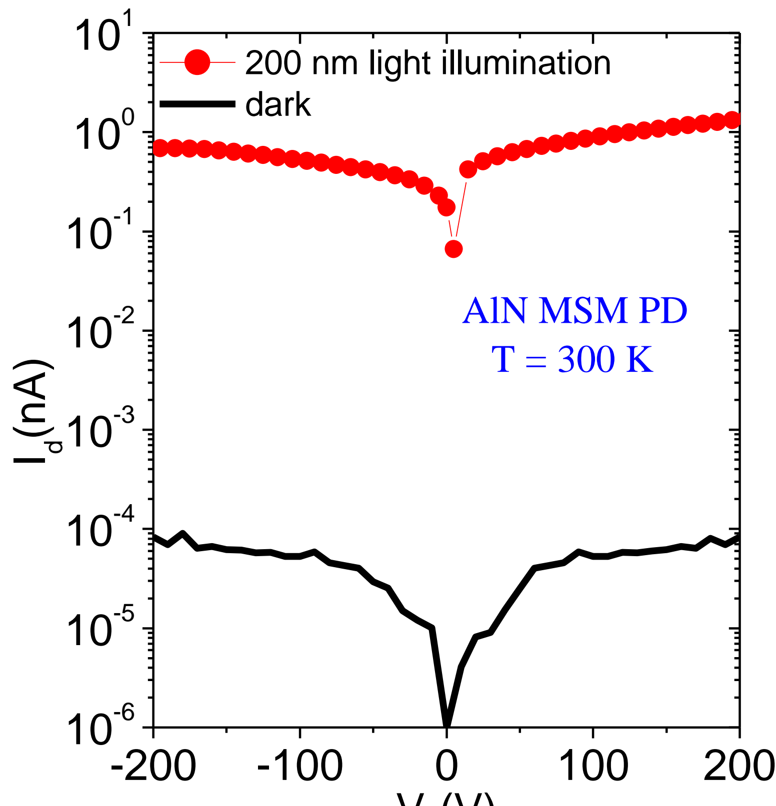

Fig. 3.9 I-V characteristics of AlN MSM photodetector in dark and under 200 nm DUV light illumination (semi-log scale).

which continuously increases and reaches about 1.3 nA at V_b = 200 V. The ratio of photocurrent to dark current up to V_b = 30 V is about five orders of magnitude for incident power density of 0.05 μW/mm^2 at 200 nm. These characteristics are direct attributes of the outstanding material properties of AlN, including large energy band gap and dielectric constant.

The most important figure of merit of PD is the responsivity. The spectral responses have been measured at different bias voltages, and an example is shown in Fig. 3.10. These AlN MSM detectors exhibit a peak responsivity of 200 nm, an extremely sharp cut-off wavelength around 207 nm, and more than four orders of magnitude of DUV to UV/visible rejection ratio as probed by our system setup. The detector responsivity increases almost linearly with the bias voltage, as

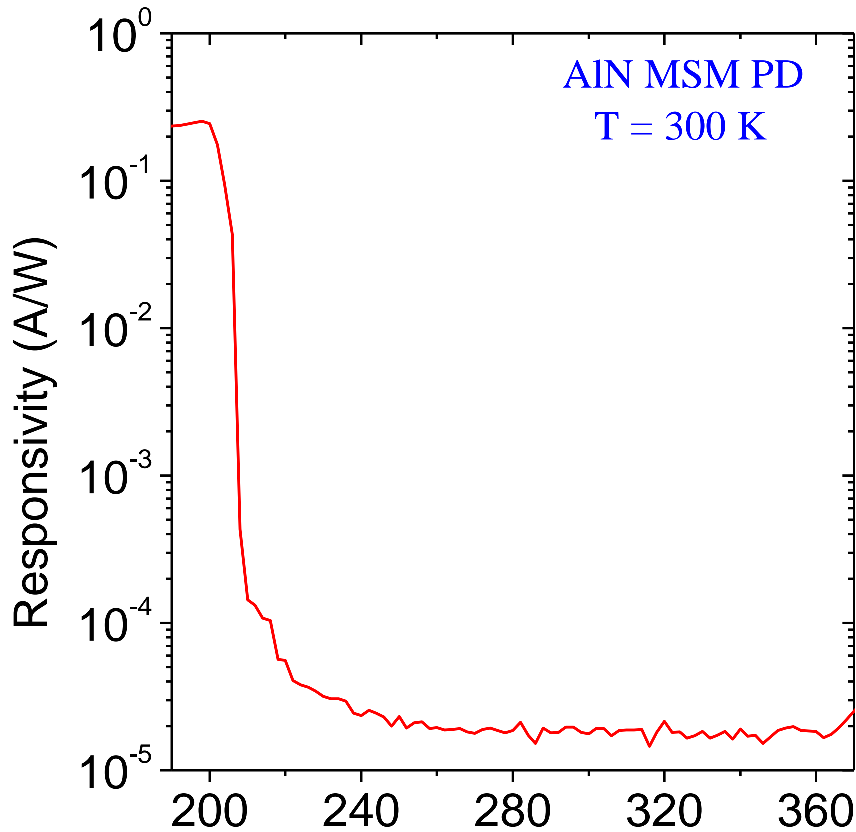

Fig. 3.10 Photoresponse of an AlN MSM detector at V_b = -30 V. Peak responsivity is at 200 nm.

illustrated in Fig. 3.11. The responsivity varies from 0.1 to about 0.4 A/W when the bias voltage is increased from 0 to 100 V. This linear increase of responsivity with bias has been previously observed in an AlN MSM photodetector grown by magnetron reactive sputtering deposition on GaN substrate [80].

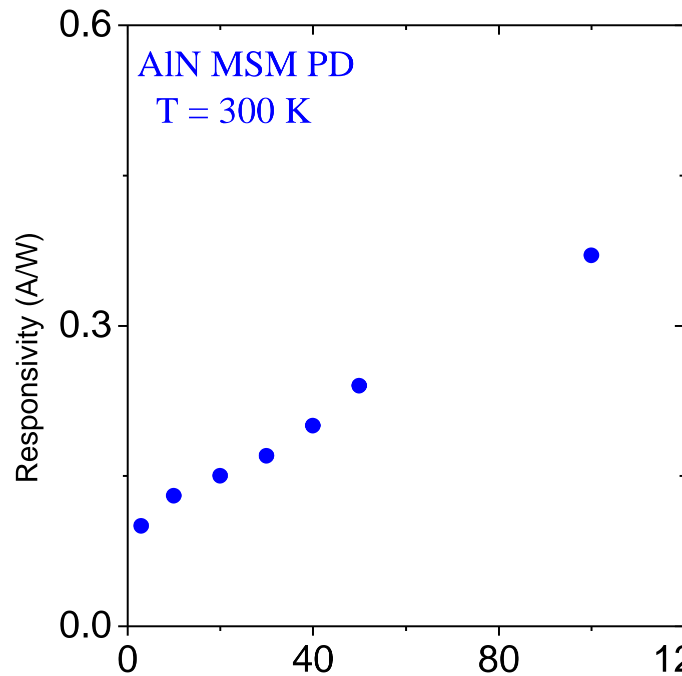

Fig. 3.11 Responsivity of AlN MSM photodetector as a function of applied bias.

The result of Fig. 3.11 suggests that MSM detector has gain, which may be attributed to the presence of dislocations or deep level defects in epilayers and its mechanism remains to be investigated. Nevertheless, this is so far the shortest cutoff wavelength achieved for semiconductor detectors. Previous work has shown that the AlGaN photodetectors significantly outperform GaN photodetectors in the VUV spectral region due to the larger energy band gap of AlGaN [13]. Since AlN has the largest energy band gap among the AlGaN alloys, our results thus illustrate the high promise of AlN based photodetectors for DUV, VUV, and EUV detection

applications. Due to the scarcity of published data on Schottky contacts formation on AlN, we believe that a great deal of improvement in device performance can be attained if further efforts were devoted to optimizing the contact schemes and surface preparation conditions. Nonetheless, the results obtained so far have demonstrated the extraordinary benefits of AlN as an active material for DUV, VUV, and EUV detector applications.

In conclusion, we have carried out the growth of high quality AlN epilayers on sapphire substrates by MOCVD and exploited its potential as an active DUV material through the demonstration of AlN MSM photodetectors. The AlN MSM photodetectors exhibit peak responsivity of 200 nm and a very sharp cutoff wavelength at around 207 nm. AlN MSM DUV detectors are also shown to possess outstanding features including extremely low dark current, high breakdown voltage, and high DUV to visible rejection ratio.

CHAPTER 4-AlN Schottky and Avalanche Photodetectors

4.1 Schottky Barrier Photodetectors

The Schottky barrier diode is a majority carrier device which has been widely used as an efficient photodetector in the visible to UV region. The dark current in a Schottky barrier photodetector (SBPD) is mainly due to thermoionic emission of majority carriers over the potential barrier formed at the metal-semiconductor junction and it does not suffer from charge storage of the minority diffusion current, which limits the high speed applications in a p-n and p-i-n photodetectors. The potential barrier formed at the metal-semiconductor junction is intrinsically determined by the difference of work functions between metal and semiconductor. In real devices, it is pinned by interface states present in the junction. The SBPD is usually operated under reverse bias condition; however, it can also be operated in photovoltaic mode i.e. under zero bias condition, which is an obvious advantage over MSM PD. In a simple configuration, the device can be mesa-shaped with n+ or p+ semiconductor layer for Ohmic contact, an intrinsic semiconductor light absorbing layer (relatively lower background carrier concentration), and a thin semi-transparent metal deposited on the top of the light absorbing layer for Schottky barrier contact formation. A thin dielectric anti-reflection coating is deposited on the metal, and contact pads are deposited through the window opening in the same dielectric layer. Schotttky PD can be designed either as lateral charge transport device (for device structure grown on insulating substrate) or vertical charge transport device (for device structure grown on conducting substrate in which back contact can be deposited).

The temporal time response and the frequency band-width of the device are determined by the transit time of carriers in the depletion layer (light absorption layer) and the external circuit parameters. The thickness of the light absorbing layer is designed in such a way that the

active layer is fully depleted under small (few volts) reverse bias and both electrons and holes drift at their respective saturation velocities. When photons with energy $h\nu > E_g$ are absorbed in the depletion region, photo-generated electron-hole pairs are drifted with their saturation velocities towards respective electrodes by the built-in electric field in the depletion layer. For many applications, SBPDs are superior to other detectors and are similar to high speed p-i-n photodiodes. SBPD is very simple device to operate and easy for design and fabrication.

4.2 AlN based Schottky deep UV Photodetectors

Aluminum nitride (AlN) has emerged as a very important photonic/optoelectronic material due to recent advances in high quality material growth [53,55,81]. Light emitting diodes with emission wavelength of 210 nm have been demonstrated using pure AlN [15]. Furthermore, we have recently demonstrated that 200 nm metal-semiconductor-metal (MSM) deep ultraviolet (DUV) photodetectors based on pure AlN [82]. DUV photodetectors have a wide range of applications including secure space communication, missile threat detection, UV radiation monitoring in environment, and biological agent detection. As a consequence of its having the widest direct band gap (6.1 eV) among III-nitride semiconductors, combined with its outstanding electro-optical and physical properties, AlN also appears to be very promising for the development of vacuum UV and extreme UV detectors where Si-based photodetectors have reached their limits. To date, AlGaN based Schottky, *p-i-n*, and MSM photodetectors grown both on SiC and sapphire substrates with excellent performances have been reported [11,67-68,74,77,83-90]. In contrast to Al-rich AlGaN based *p-i-n* photodetectors, AlGaN Schottky barrier detectors are majority carrier devices, which do not face the challenging requirement of high quality *p*-type AlGaN layer for low resistance Ohmic contact formation. Furthermore, the ease of growth, fabrication, efficient photo-generated carrier collection near the semiconductor

surface, and high responsivity at zero bias are the other advantages of Schottky barrier photodetectors. The shortest cutoff wavelength of $Al_xGa_{1-x}N$-based Schottky barrier photodetectors achieved so far is 265 nm, corresponding to an Al mole fraction x~0.5 [90]. AlGaN-based Schottky barrier photodetectors grown on SiC substrates for Al mole fraction of ~ 0.4 were shown to possess a zero bias detectivity of 7.9×10^{14} cm $Hz^{1/2}$ W^{-1} and dark current density of 2.2×10^{-10} A cm^{-2} at −5 V [91].

4.3 AlN based Schottky deep UV Photodetectors grown on SiC Substrate

The growth of high quality AlN epilayer directly on conductive SiC substrates naturally provides a hybrid Schottky barrier photodetector structure that does not require the growth of *n*-type AlN layer. AlN layer has outstanding interfacial properties when deposited on SiC due to an excellent lattice match to SiC (mismatch~1%) [92-95]. Compared to AlGaN/*n*-AlGaN Schottky barrier photodetector structures grown on sapphire substrates, AlGaN/*n*-SiC hybrid Schottky barrier photodetector structures are expected to possess higher crystalline quality (and hence lower dislocation density) and minimal doping induced defects. On the other hand, compared to photodetectors based on pure indirect band gap SiC, AlGaN/*n*-SiC hybrid Schottky barrier photodetector structures are expected to provide higher detectivity and variable cutoff wavelength due to their adjustable direct band gaps. We discuss here the growth, fabrication, and characterization of AlN/*n*-SiC hybrid Schottky barrier photodetectors. The fabricated photodetectors exhibit very high reverse breakdown voltages, extremely low dark currents, high responsivity, high DUV to UV/visible rejection ratio, and high thermal energy limited detectivity at zero bias.

4.4 AlN SBPDs on SiC Substrate: Growth & Fabrication

Undoped AlN epilayers of about 1 μm in thickness were grown on heavily doped *n*-type Si-face 4*H*-SiC substrates by MOCVD. Trimethylaluminum and ammonia (NH_3) were the sources for Al and N, respectively. Atomic force microscopy revealed a very smooth surface

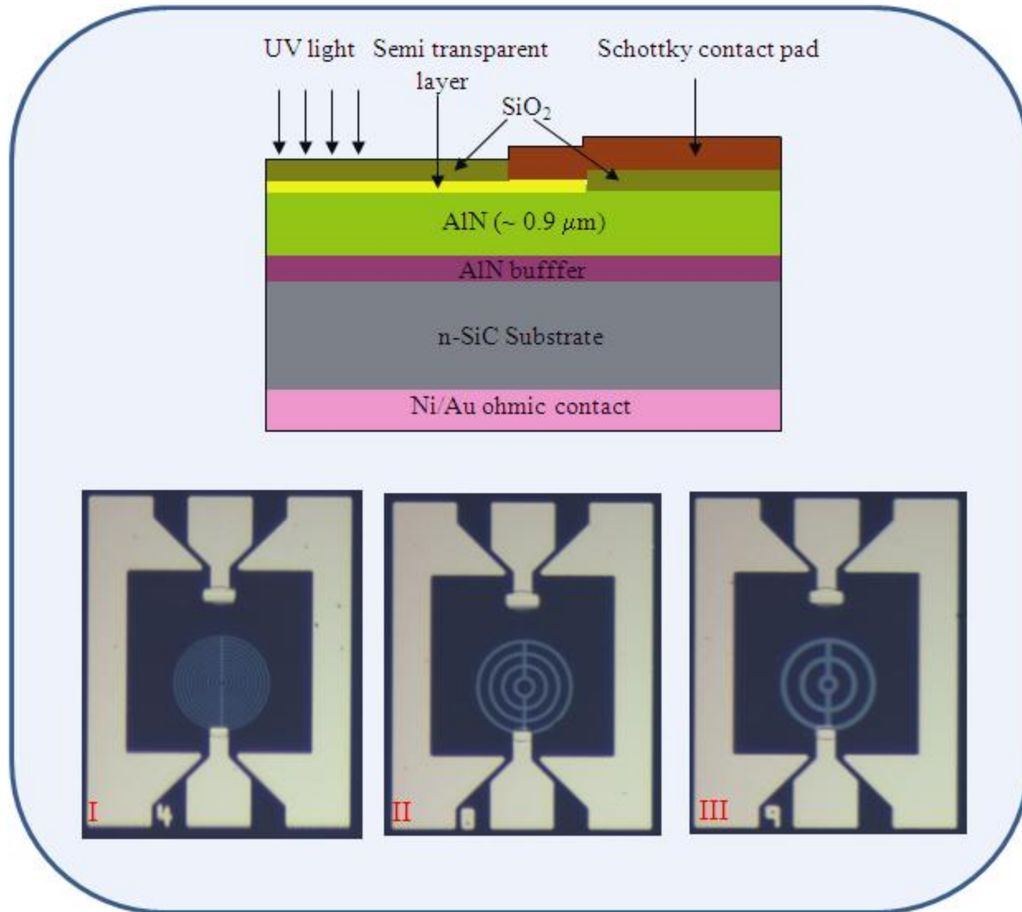

Fig. 4.1 (a) Schematic layer structure of AlN/*n*-SiC hybrid Schottky barrier photodetector and (b) optical microscopy images of fabricated photodetectors with a device size of 100 μm in diameter, but having different ring width and spacing.

morphology of AlN epilayer with a root-mean-square value of about 0.6 nm. The device fabrication process consisted of the following steps. Ohmic contact was formed on the SiC substrate side by e-beam evaporation of 150 nm Ni and 50 nm Au, followed by a rapid thermal annealing at 950 ℃ for 60 s. Before annealing, 100 nm SiO_2 was deposited on AlN epilayer by

plasma enhanced chemical vapor deposition (PECVD) for protection of AlN epilayer during high temperature annealing, which was later removed by wet etching. Photolithography was used to define the semi-transparent Schottky contact area. A 10 nm Pt was deposited by e-beam evaporation to form Schottky contacts. The Schottky contact is designed with inter-connected concentric circular patterns with different width and spacing between them so that the light reflection by semi-transparent metal is reduced with optimized light absorption in active layer. Then, 100 nm SiO_2 was deposited by PECVD for passivation. Photolithography and selective area wet etching of SiO_2 were used to open window for Schottky contact pad deposition. A Ni (40 nm)/Au (160 nm) bilayer were deposited using e-beam evaporation to form Schottky bonding pad. Finally, devices were bonded in ten-pin flat packs for characterization. Figure 4.1(a) shows the schematic layer structure of the fabricated SBPD employed in this study, in which undoped AlN epilayer serves as an active layer. Fig. 4.1(b) shows the optical microscopy images of fabricated devices. The size of the top Schottky contact is 100 μm in diameter (d=100 μm) with different circular pattern widths and spacings. Our measurement system consisted of a deuterium light source, monochromator, Keithley 2400 source meter, and 617 electrometer for spectral response and *I-V* characteristic measurements as discussed in previous chapter.

4.5 AlN SBPDs on SiC substrate: Device Characterization

Figure 4.2 shows the typical dark current-voltage (*I-V*) characteristics of the device. The fabricated device showed a reverse breakdown voltage (V_B) exceeding 200 V, which corresponds to a breakdown field exceeding 2.2×10^6 V/cm. These devices also exhibit very low dark currents (I_d), which is below 10 fA at a reverse bias voltage (V_b) of −50 V. I_d is in picoampere range at V_b= −200 V. Beyond −200 V, I_d starts to increase rapidly. The differential resistance R (=dV/dI) in the range of V_b between 0 and −50 V was in excess of 5×10^{16} Ω. These features are direct

attributes of the outstanding material properties of high quality AlN epilayers including large energy band gap and dielectric constant. Spectral photoresponse measurements have been carried out for d=100 μm devices at different bias voltages. Figure 4.3 shows the spectral

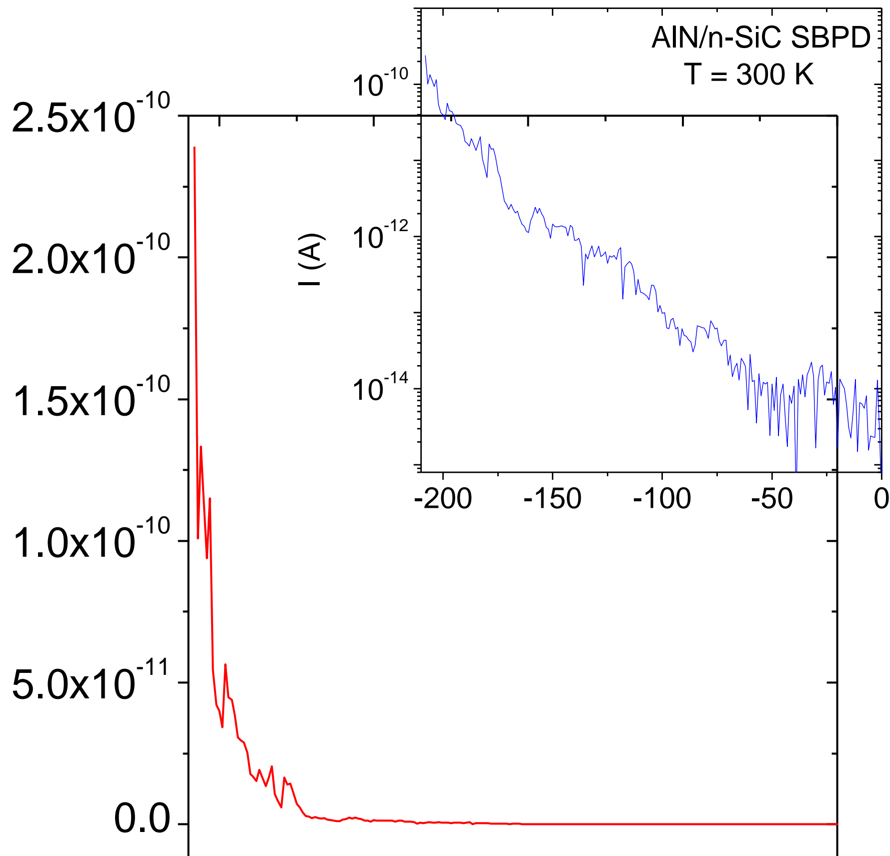

Fig. 4.2 *I-V* characteristics of an AlN/*n*-SiC hybrid Schottky barrier photodetector. The inset shows the same plot in semi-log scale.

photoresponse in the wavelength range from 190 to 360 nm measured under V_b=−10 V. These AlN-based Schottky photodetectors have peak responsivity of about 0.12 A/W at 200 nm and a very sharp cutoff around 210 nm. This is the shortest cut-off wavelength and highest breakdown voltage attained so far for AlGaN based Schottky barrier photodetectors. These cutoff wavelength and peak response wavelength are comparable to those of the AlN based

MSM photodetectors we previously reported [82]. Also, a DUV to near UV rejection ratio of more than four orders of magnitude has been observed. Furthermore, we did not observe photoresponses from SiC substrate. This can be attributed to the large conduction- and

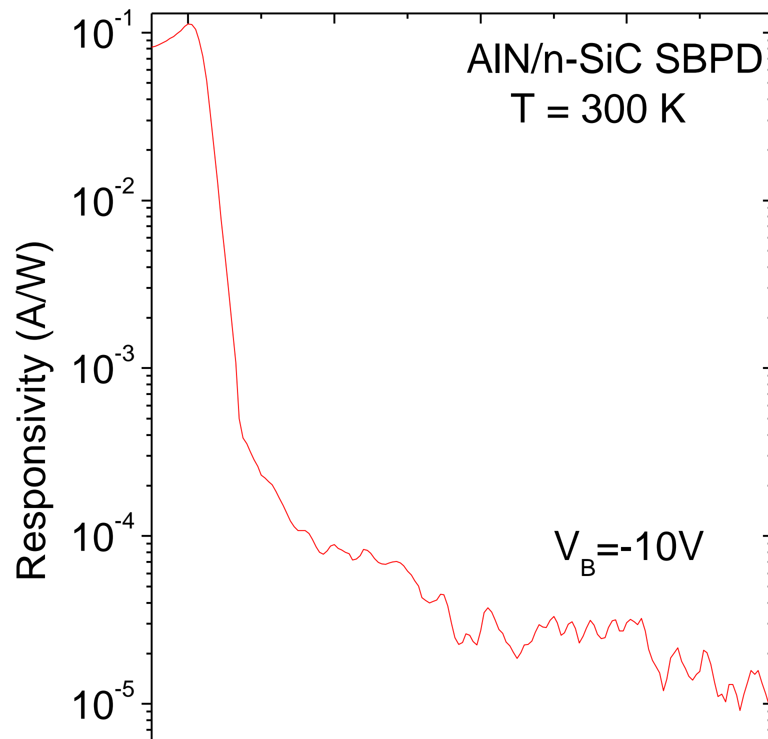

Fig. 4.3 Spectral photoresponse of an AlN/*n*-SiC hybrid Schottky barrier photodetector measured at V_b=−10 V.

valance-band offsets at the AlN/SiC interface, which were estimated to be around 1.3 and 1.7 eV, respectively [95]. The large band offsets, in general, will prevent the collection of photoexcited carriers in the lower band gap contact layer [89], which is *n*-SiC in this case.

The bias (V_b) dependent spectral responsivity has also been studied. In Fig. 4.4, we plot the spectral photoresponses measured in the bias range from 0 to −25 V. The peak responsivity at λ=200 nm as a function of V_b is shown in the inset of Fig. 4.4. The responsivity initially increases by a factor of 1.4 when V_b changes from 0 to −5 V and it then increases slightly by a factor of only 1.2 when V_b increases from −5 to −25 V. Such a weak V_b dependent responsivity observed in the bias range of −5 to −25 V seems to indicate that the 1 μm thick undoped AlN active layer was almost fully depleted up to V_b=−5 V. The device also exhibits a relative high responsivity of only 1.2 when V_b increases from −5 to −25 V. Such a weak V_b dependent responsivity observed in the bias range of −5 to −25 V seems to indicate that the 1 μm thick undoped AlN active layer was almost fully depleted up to V_b=−5 V. The device also exhibits a relative high responsivity of 0.078 A/W at 200 nm in the photovoltaic

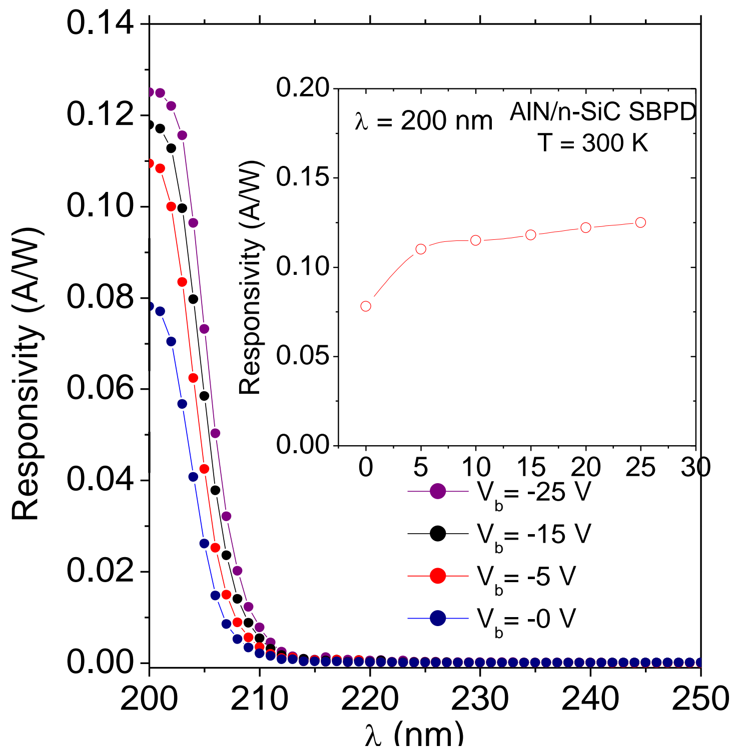

Fig. 4.4 Spectral photoresponses of an AlN/*n*-SiC hybrid Schottky barrier photodetector measured at different bias voltages V_b. The inset shows the peak responsivity at 200 nm as a function of V_b. The responsivity in the photovoltaic mode (zero bias) is 0.078 A/W.

mode (zero bias). Figure 4.4 also shows that the cutoff wavelength of the device is slightly red shifted with increasing the reverse bias voltage.

For solar blind photodetectors based on wide band gap semiconductors, the detectivity performance is thermally limited because the noise current due to background radiation is far less than the noise current due to thermal energy. Therefore, the thermal energy limited specific detectivity is given by

$$D = R_\lambda \left(\frac{R_0 A}{4kT}\right)^{\frac{1}{2}} \tag{4.1}$$

where R_λ is the zero bias responsivity, R_0 is differential resistance, k is Boltzmann's constant, A is the detector active area, and T is the absolute temperature [96]. With resistance-area product R_0A=3.93×10^{12} Ω cm^2, the room temperature specific detectivity of our AlN/*n*-SiC hybrid Schottky barrier photodetectors is deduced to be about 1.0×10^{15} cm Hz$^{1/2}$ W^{-1}, which is one of the highest values reported so far for AlGaN UV photodetectors. This very high detectivity is due to the extremely low leakage current and high zero bias responsivity. The very high breakdown electric field and extremely low dark current over a wide range of applied reverse bias obtained for these AlN/*n*-SiC hybrid Schottky photodetectors suggest that it is feasible to build avalanche photodetector structures on AlN/*n*-SiC templates by further improving material quality and device design, primarily through further reduction of the dislocation density, and optimizing device area and active layer thickness.

In summary, we report on the growth, fabrication, and characterization of AlN/*n*-SiC hybrid Schottky photodetectors and demonstrated the potential advantages of AlN as an active material for DUV optoelectronic device applications. These photodetectors exhibit very high reverse breakdown voltage (>200 V), extremely low dark current (less than 10 fA at V_b −50 V),

high responsivity, high thermal energy limited detectivity, and high DUV to UV/visible rejection ratio.

4.6 AlN SBPD on Sapphire Substrate

Research interest in deep UV photodetection has increased significantly in recent years due to the expanding applications of these devices in civil, military, medical and research fields. Some major applications include solar UV monitoring, UV astronomy, engine control, flame sensing, missile plume detection, space communication etc. The requirement of compact, light weight, robust and intrinsically suppressed visible response (no need of external filter to stop high intensity visible background light response) for these applications can be satisfied by AlGaN based photodetectors due to its tunable band gap between 3.4 eV (GaN) to 6.1 eV (AlN), radiation and chemical resistant, and direct wide band gap. Due to tremendous efforts and advanced material growth techniques, the screw and edge threading dislocation densities in Al rich AlGaN grown on sapphire or SiC substrates has been reduced significantly to the order of ~ 10^6 cm^{-2} and 10^8 cm^{-2}, respectively [97, 98]. The improved material qualities of Al rich AlGaN has resulted in better conductivities of p- and n- type in this material system. Deep UV emitters (LEDs, LDs) [99-101] and detectors (MSM, Schottky, p-i-n etc) [67, 68, 82-86] based on AlGaN have already been demonstrated. Compared to photoconductors and p-i-n photodiode, Schottky barrier photodetectors have a relatively simple device structure, easier fabrication steps, high device response speed and improved responsivity in deep UV photon detection applications. Furthermore, it does not require p-type conducting layer, which is still a challenging problem for Al rich AlGaN alloys. To date, the shortest reported cutoff wavelength for AlGaN based SBPD grown on sapphire substrate is 290 nm, which corresponds to 40 % Al concentration in AlGaN alloys [102].

In general, AlN grown on SiC substrates are expected to have higher crystalline quality due to the better lattice match between AlN and SiC (mismatch is ~1%). However, the SiC substrate is relatively expansive and its band gap of 3.4 eV limits the use of photodetector devices grown on SiC to frontal illumination in deep UV application. On the other hand, sapphire substrates are relatively cheap and the growth of photonics device structures based on high quality AlGaN materials on sapphire substrates has been well established. Therefore, AlGaN based Schottky barrier photodetectors on sapphire substrate show great promise for the fabrication of deep UV sensor arrays for developing DUV, where illumination of light through substrate side greatly simplifies the device design. In this section, we present the growth, fabrication and characterization of AlN based Schottky barrier photodetectors on sapphire substrates.

4.7 AlN SBPDs on Sapphire substrate: Growth & Fabrication

The Schottky photodetector structure was grown by MOCVD. Trimethylaluminum and ammonia (NH_3) were the sources for Al and N, where as SiH_4 was used for Si doping, respectively. The growth of the device structure started with the deposition of a low temperature AlN buffer layer followed by high temperature growth of about 1 μm AlN, which served as a dislocation filter layer. Then about ~ 1.1 μm Si doped $Al_{0.77}Ga_{0.23}N$ n-contact layer was deposited which was followed by the growth of ~ 200 nm slightly Si doped AlN for active layer (light absorption layer). Due to the high absorption coefficients (> $10^5 cm^{-1}$) of AlN near intrinsic band edge, 200 nm thick AlN is sufficient for complete absorption of DUV light within that thickness. The lower bandgap of n-Ohmic contact layer is advantageous to prevent a response from the n-contact layer due to the photo-generated carriers in Ohmic contact whose transport mechanism is mainly diffusion which causes the long tail in response curve. The device

fabrication process consisted of the following steps. The device mesas were defined by optical lithography and dry etching of top AlN layer down to n-contact layer using inductively coupled plasma (ICP) techniques. Ohmic contact was formed on the n-$Al_{0.77}Ga_{0.23}N$ layer by depositing Ti/Al/Ni/Au (30/120/30/100) using e-beam evaporation and rapid thermal annealing at 950 ^{O}C for 30 sec under nitrogen gas flow. Photolithography was used to define the semi-transparent Schottky contact area. A 10 nm Pt was deposited by e-beam evaporation to form Schottky contacts on the mesa area. The Schottky contact is designed with inter-connected concentric circular patterns with different width and spacing between them so that the light reflection by semi-transparent metal is reduced with enhanced light absorption in active layer. Then 100 nm SiO_2 was deposited by PECVD for passivation. Photolithography and selective area wet etching

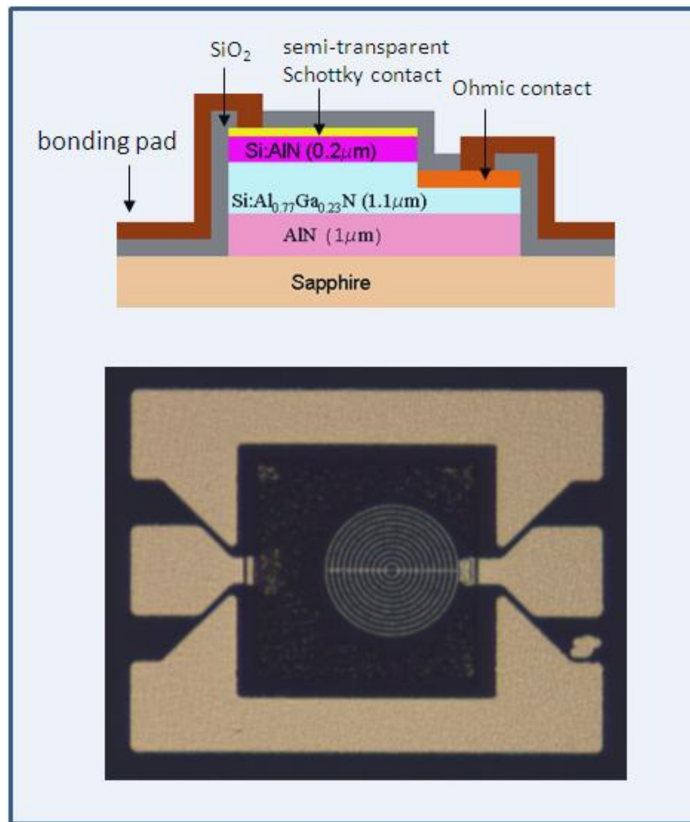

Fig. 4.5 (a) Schematic layer structure of AlN Schottky barrier photodetector on AlN/sapphire template and (b) optical microscopy image of a fabricated photodetector with a device size of 100 μm in diameter.

of SiO_2 were used to open window for Schottky contact pad deposition. A Ni (40 nm)/Au (160 nm) bilayer were deposited using e-beam evaporation to form Schottky bonding pad. Finally, devices were bonded in ten-pin flat packs for characterization. Figure 4.5 (a) shows the schematic layer structure of the fabricated SBPD employed in this study, in which undoped AlN epilayer serves as an active layer. Fig. 4.5 (b) shows the optical microscopy images of fabricated devices. The size of top Schottky contact is 100 μm in diameter with different circular pattern widths and spacing. Our measurement system is same as discussed in the previous chapter.

4.8 AlN SBPDs on AlN/Sapphire template: Device Characterization

Figure 4.6 shows the typical dark current-voltage (*I*-*V*) characteristics of 50 μm in

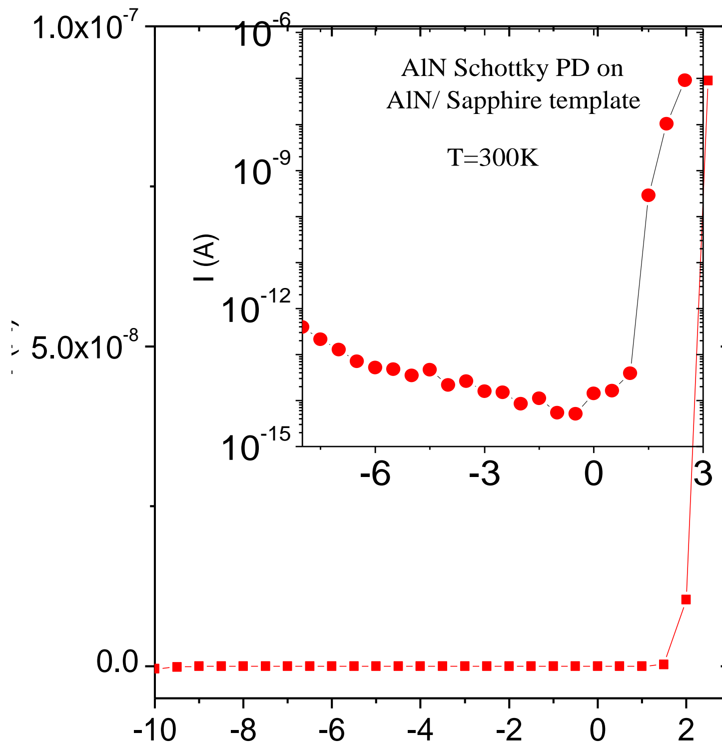

Fig. 4.6 *I*-*V* characteristics of an AlN Schottky barrier photodetector on AlN/sapphire template. The inset shows the same plot in semi-log scale.

diameter mesa size device. The device showed a turn on voltage of about 2 V, and the dark current around – 2 V is about 10 fA which continuously increases to picoampere range when applied bias reaches to – 8 V. The dark current for this device V_b = -10 V is about 2 orders of magnitude higher than that of AlN based Schottky diode grown on SiC substrate , which is discussed in the previous section. The higher dark current in these devices could be due to Si doping in active layer. The differential resistance R (=dV/dI) near V_b = 0 V was in excess of 1×10^{15} Ω. These features are the direct attributes of the outstanding material properties of AlN epilayers including large energy band gap and dielectric constant.

Spectral photoresponse measurements have been carried out for d = 50 μm devices at different bias voltages. Figure 4.7 shows the spectral photoresponse in the wavelength range from 190 to 350 nm measured under V_b= −5 V. These AlN-based Schottky photodetectors

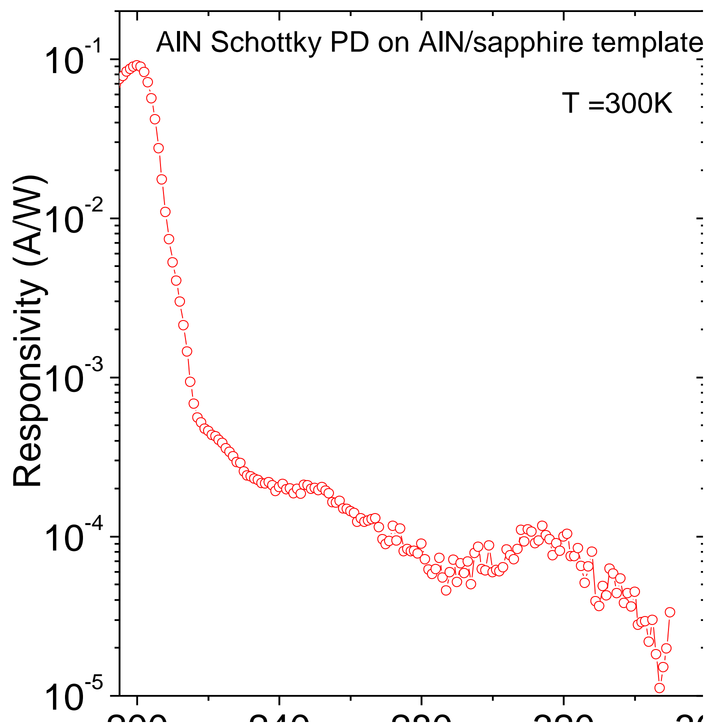

Fig. 4.7 Spectral photoresponse of an AlN Schottky PD on AlN/sapphire template measure at V_b = −5 V.

have peak responsivity of about 0.09 A/W at 200 nm and very sharp cutoff around 210 nm. This is the shortest cutoff wavelength achieved so far for AlGaN based Schottky barrier photodetectors grown on sapphire substrates. These cutoff wavelength and peak response wavelength are comparable to those of AlN based MSM photodetectors and AlN hybrid Schottky PD grown on sapphire and SiC substratess, respectively, which are presented in the previous sections. From Fig. 4.7, it is observed that DUV to near UV rejection ratio (the ratio of responsivity at DUV to that at near UV wavelength) is more than 3 orders of magnitudes. These features of AlN based DUV Schottky photodetectors are promising to fabricate DUV PD arrays to develop DUV cameras which have a wide range of applications in security and other fields.

Measurements have also been carried out to determine the external quantum efficiency (EQE) of the device. The EQE for 50 μm device under different reverse bias voltages are shown

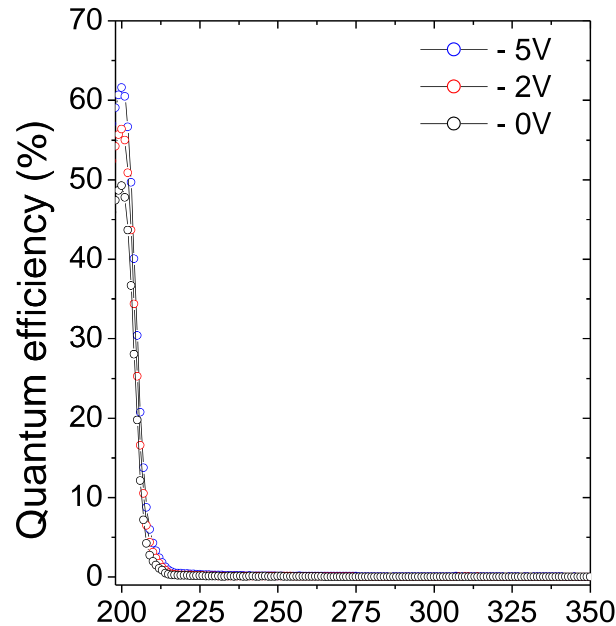

Fig. 4.8 Spectral EQE of an AlN Schottky PD under different reverse bias voltages.

in Fig. 4.8. The EQE at 200 nm under zero bias (photovoltaic mode) is about 50 %, which increases to 60 % for V_b = -5 V.

4.9 Reverse breakdown field comparison for AlN on n-SiC and AlN/sapphire substrates

In order to gain insight about material quality, reverse breakdown fields (electric field beyond which the device reverse bias current increases abruptly and destroy the device for AlN

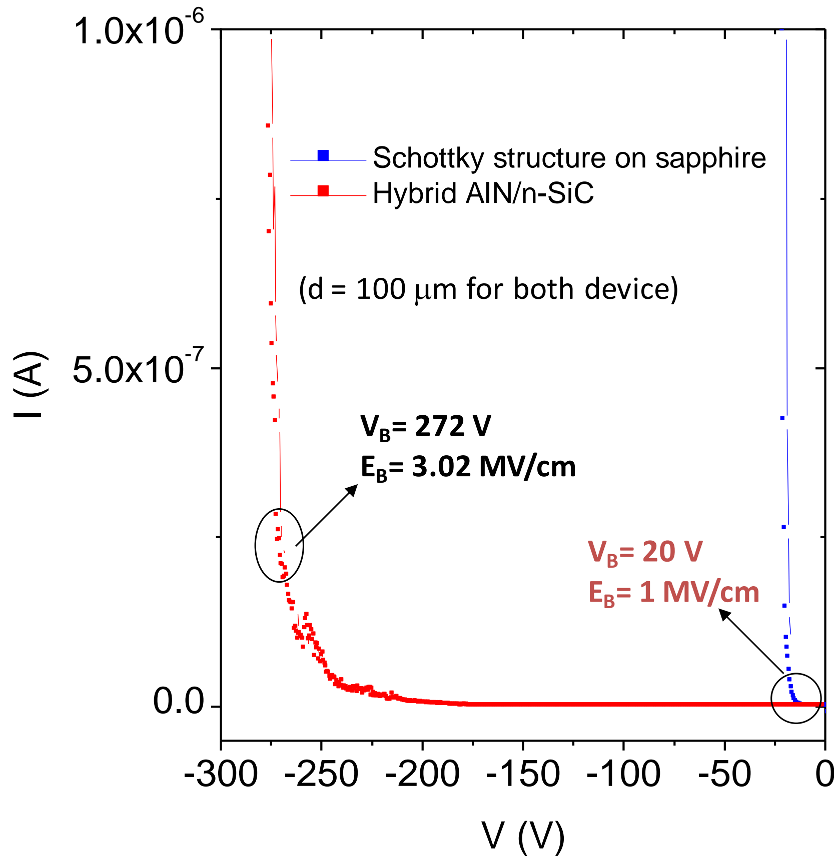

Fig. 4.9 Reverse break down field comparison for AlN grown on n-SiC and AlN/sapphire template.

Schottky PDs grown on AlN/sapphire template and n-SiC substrates have been compared. The results in Fig.4.9 show that the device breakdown field for AlN grown on sapphire (E_B = 3.2 MV/cm) is three times greater than that of AlN (E_B = 1 MV/cm) grown on AlN template. The higher breakdown field for AlN grown on n-SiC substrates is attributed to better crystalline

quality i.e. less threading dislocations density, due to the better lattice match of AlN with SiC compared to sapphire. Further, the device on AlN/sapphire template is mesa etched which could lead to edge breakdown and reduces the breakdown field.

4.10 AlN Avalanche Photodetectors

AlN has attracted tremendous interest as a material for deep ultraviolet (DUV) optoelectronic devices because of its ultrahigh direct bandgap. Recent advances in epitaxial growth techniques have made it possible to grow high quality AlN epilayers on different substrates [53, 55, 81, 103]. A few active DUV devices based on pure AlN have also been demonstrated, including 210 nm LEDs [15] and 200 nm PDs [82, 104]. It was shown that AlN based photodetectors possess an extremely low dark (leakage) current with a detectivity that is comparable to that of photomultiplier tubes (PMTs) [104]. Due to the intrinsic solar blindness, radiation hardness and high temperature stability, AlN based DUV detectors have applications in many areas of science and technology including secure space communication, hazardous chemical and biological agent detection, and UV radiation monitoring in environment and flame sensing. Furthermore, the outstanding optoelectronic and mechanical properties make AlN a promising candidate for the development of detectors operating down to the extreme UV region with excellent responsivity where Si based technology have reached their limits.

The highly matured existing PMT technology offers very high sensitivity, low dark current, and internal photocurrent gain greater than 10^6 for radiation detection applications. However, PMTs are bulky, fragile, require high bias voltage (>1000 V), cooling hardware and expensive filters, and are sensitive to magnetic fields. AlGaN based intrinsic solar blind solid state detectors with high internal photocurrent gain can overcome many of the shortcomings of

PMTs by offering compactness, high sensitivity, moderate bias, and ability for chip-level integration with other optoelectronic devices. Many researchers have already demonstrated AlGaN based MSM, Schottky, and *p*-*i*-*n* photodiodes with excellent performances for DUV detection applications [11, 68, 74, 77, 83-89]. However, there are only a few reports on AlGaN based avalanche photodiodes (APDs) with reasonable internal photocurrent gain utilizing either *p*-*i*-*n* or Schottky device structures [105-108]. The shortest cut-off wavelength reported so far is 276 nm for $Al_xGa_{1-x}N$ (x=0.4) based APDs [105, 106]. Most of the earlier reported AlGaN based APDs are closer to lateral charge transport devices in which surface defect charge and electric field crowding at electrode edges can degrade the device performance [109, 110]. True vertical AlGaN based APDs have not been reported so far. High quality interface and a better lattice match (mismatch <1%) between AlN and SiC [92, 93] together with the conductive nature of SiC substrate provide the feasibility to build vertical conducting AlN/*n*-SiC DUV APDs. In these devices, under a high reverse bias, the high electric field across the AlN epilayer accelerates the charge carriers in the vertical direction, during which the charge carriers gain sufficient kinetic energy leading to impact ionization. Below, we describe the growth, fabrication, and characterization of vertical conducting AlN Schottky APDs with a large linear mode photocurrent gain.

4.11 AlN avalanche Photodetectors: Growth and Fabrication

The layer structure of DUV APDs consists of an AlN epilayer grown on *n*-SiC substrate. AlN epilayers of about 0.9 μm were grown on *n*-type 4*H*-SiC substrates by metal-organic chemical-vapor deposition. The device fabrication starts with the deposition of Ohmic contact on the SiC substrate side by e-beam evaporating a Ni (200 nm)/Au (50 nm) bilayer, followed by

950 ℃ annealing for 60 s in N_2. Schottky contact area was defined by evaporating a 6 nm thick Pt layer followed by photolithography and lift-off. Then, a 100 nm SiO_2 passivation layer was deposited by PECVD. Schottky bonding pads were formed by evaporating a Ni (40 nm)/Au

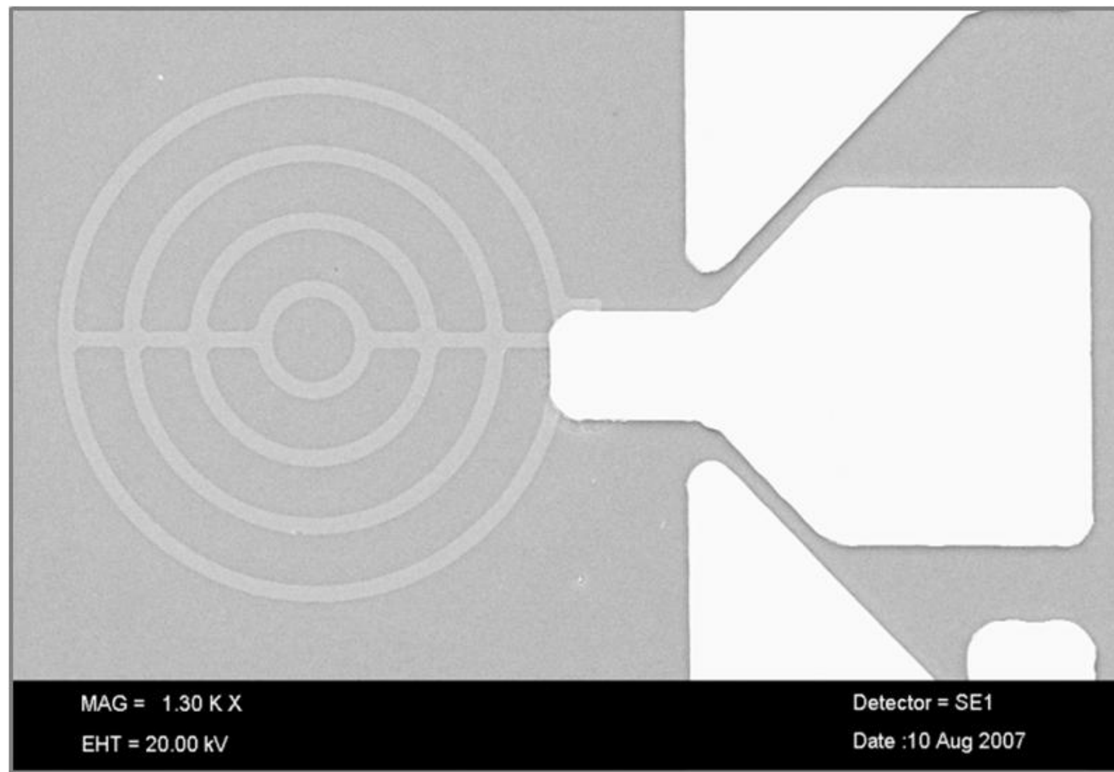

Fig. 4.10 SEM image of a fabricated AlN APD with d=100 μm in diameter.

(160 nm) bilayer after opening window on SiO_2 passivation layer using photolithography and selective area wet etching of SiO_2. The fabricated devices were 100, 50, and 30 μm in diameters. Finally, devices were bonded in ten-pin ceramic flat packs for characterization. Figure 4.10 shows the schematic layer structure and scanning electron microscopy (SEM) image of a fabricated AlN APD. The top undoped AlN epilayer serves as both the light absorption and carrier multiplication layer with a cut-off wavelength of λ_c= 210 nm, which corresponds to the room temperature band-edge absorption of 5.96 eV of AlN.

4.12 AlN avalanche Photodetectors: Characterization

Figure 4.11 shows the reverse biased current-voltage (*I-V*) characteristics for d=100 μm device under dark (solid line) and DUV (200 nm) light illumination. The dark current (I_d) is extremely small and below 10 fA up to a reverse bias (V_b) =−60 V. I_d is about 10 pA around V_b= −180 V. Beyond $V_b = -180$ V (or E_b=2 MV/cm), I_d increases exponentially with increasing V_b. These devices exhibit a reverse breakdown voltage (V_B) exceeding −250 V corresponding to a breakdown field (E_B) exceeding 3 MV/cm. Large V_B and small I_d values provide the necessary conditions for observation of the avalanche effect in these detectors. The upper curve in Fig. 4.11 represents the *I-V* characteristic under 200 nm DUV illumination with an incident power density

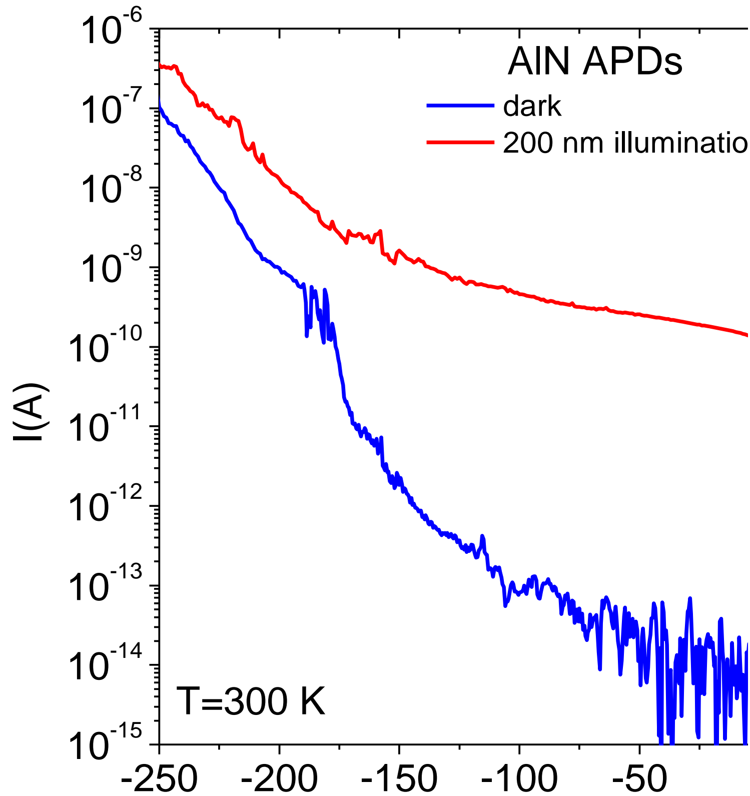

Fig. 4.11 I-V characteristics of AlN APD with d=100 μm in dark and under 200 nm light illumination.

(P_{inc}) of about 0.05 μW/mm^2. The photocurrent (I_{ph}) starts to increase rapidly as V_b increases from 0 V and saturates at around V_b= −10 V. This behavior suggests that the 0.9 μm active AlN epilayer is fully depleted up to V_b= −10 V. Beyond V_b= −10 V, I_{ph} increases slowly up to V_b= −180 V. Therefore, I_{ph} at V_b −10 V was taken as unity gain photocurrent. Similar to I_d, I_{ph} also increases exponentially beyond V_b = −180 V, which suggests the avalanche multiplication of photo-generated carriers due to the presence of a high electric field in the multiplication layer. The electric field at which the avalanche multiplication starts to occur was about 2 MV/cm. A field of about 1 MV/cm for the observation of the onset avalanche gain in $Al_xGa_{1-x}N$ (x~0.4) based Schottky and *p-i-n* photodetector structures has been previously reported [105, 106]. We also estimated that the critical field to initiate impact ionization in AlN using the relation $E = V_d/\mu$, where μ is the electron mobility and V_d is the drift velocity, which is given by [111] $V_d = (3E_g/m_e)^{1/2}$, where E_g and m_e are the band-gap energy and electron effective mass of AlN, respectively. With E_g= 6.1 eV, m_e=0.48 m_0, and μ = 135 cm^2/Vs [112, 113], the critical electric field is about 1.9 MV/cm, which agrees very well with our experimentally observed value of 2 MV/cm. From the *I-V* curves measured under dark and DUV illumination, photocurrent multiplication or gain (M_{ph}) as a function of V_b can be calculated according to

$$M_{ph} = \frac{(I'_{ph} - I'_d)}{(I_{ph} - I_d)} \tag{4.2}$$

where I'_{ph} and I'_d are multiplied photo- and dark currents, respectively, whereas I_{ph} and I_d are primary (unmultiplied) photo- and dark currents at the unity gain region. Figure 4.12 shows M_{ph} as a function of V_b. M_{ph} does not increase significantly between V_b = −10 and −180 V and starts to increase exponentially beyond V_b = −180 V and reaches about 1200 at V_b= −250 V (which corresponds to an electric field of about 3 MV/cm). These vertical carrier transport

photodetectors without mesa etch sidewall precludes the edge related gain mechanism. Furthermore, the exponentially increasing nature of M_{ph} with V_b occurring only at very high

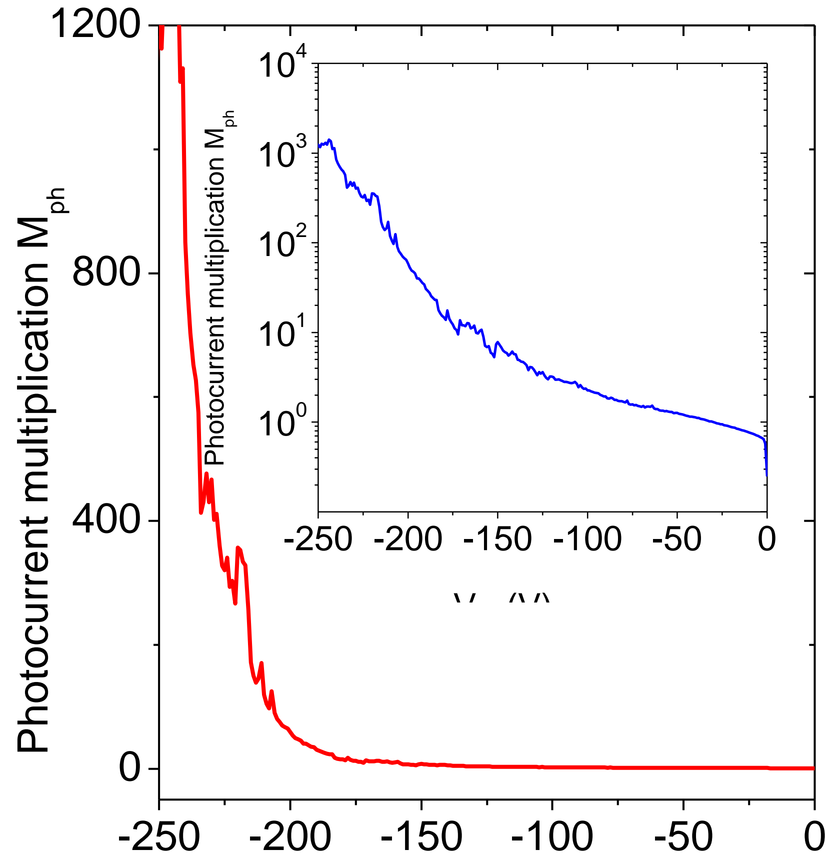

Fig. 4.12 Photocurrent multiplication or gain of an AlN APD with d=100 μm, M_{ph}, as a function of the reverse bias voltage V_b. M_{ph} increases only slowly at $|V_b|<180$ V, but increases exponentially at $|V_b|>180$ V and reaches about 1200 at $V_b=-250$ V. The inset is the same plot in the semi-log scale.

reverse field rules out the possibility of photoconductive gain, which may take place even at lower V_b and increases only linearly with applied voltage [106]. Furthermore, we have measured I_d at different temperatures and observed that I_d was temperature dependent, which suggests that the gain mechanism is not related to Zener tunneling [105]. Therefore, the linear mode photocurrent gain observed in our devices is related to the soft avalanche multiplication of

carriers due to impact ionization. The results are believed to be related to the better quality of AlN compared to AlGaN alloys, in which alloy scattering reduces carrier mobility [114]. The critical electric field for the onset avalanche is inversely proportional to carrier mobility for a given drift velocity. It also may be related to the advantages of vertical conducting devices, where surface defect charge and carrier scattering by charged dislocations have less severe effects on device performance. Moreover, the ratio of I_{ph} to I_d is more than four orders of magnitude up to $V_b = -100$ V.

We have also studied the variation of V_B with the device size for these photodetectors. The reverse *I-V* characteristics for d=100, 50, and 30 μm devices are shown in Fig. 4.13, which clearly indicate that the breakdown voltage increases as the device size inreases. This is a direct

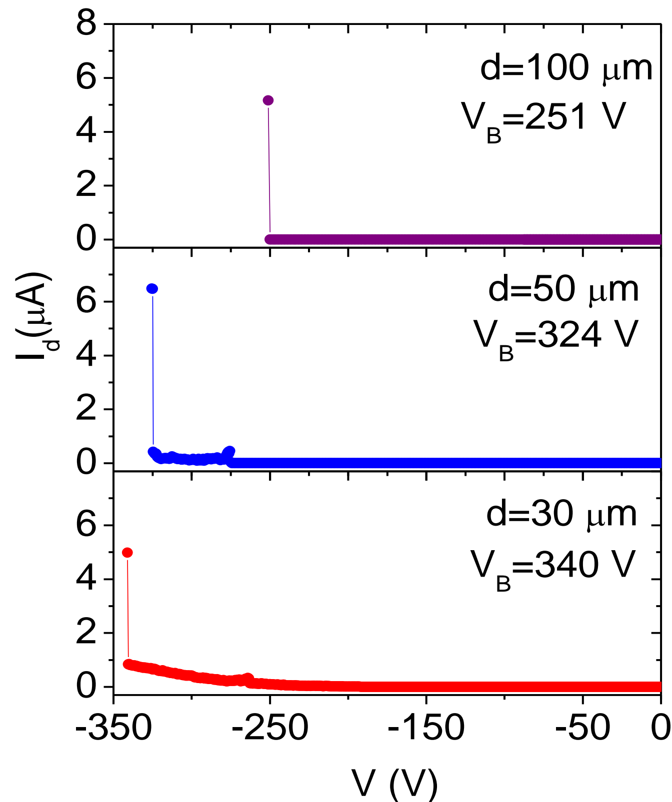

Fig. 4.13 Reverse bias *I-V* characteristics of AlN APDs with d =100, 50, and 30 μm in diameter. The breakdown voltage V_B increases with device size.

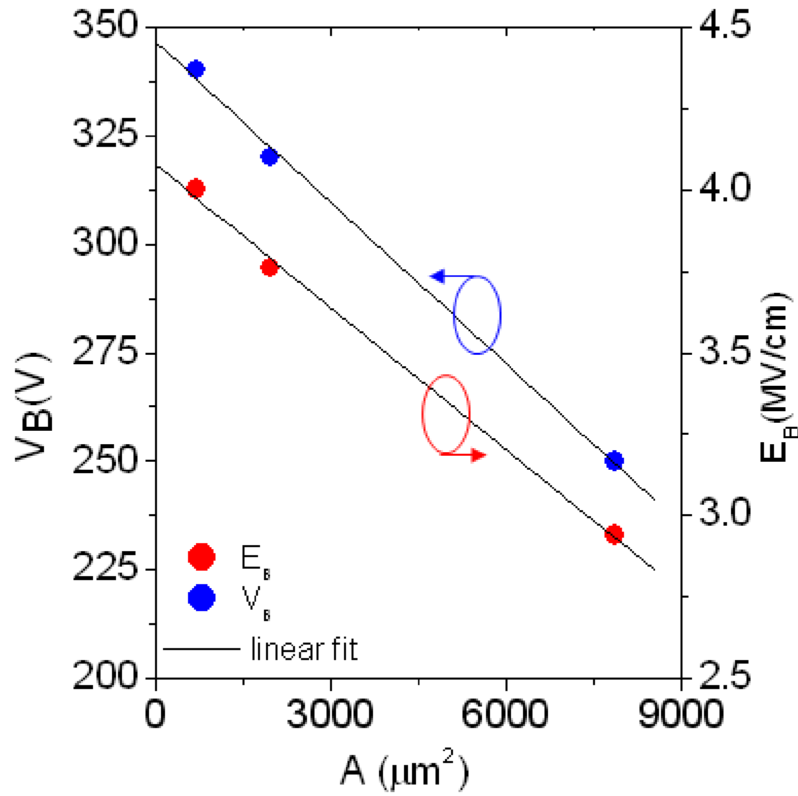

Fig. 4.14 Reverse breakdown voltage (V_B) and breakdown field (E_B) as functions of the device area $A(=\pi d^2/4)$ for AlN APDs. The solid lines are the linear least square fits of data. The breakdown field of dislocation-free AlN epilyer (E_B at d=0) is about 4.1 MV/cm.

consequence of the presence of threading dislocations in the device, because the breakdown voltage should be device size independent if the material is defect-free. This point is further elucidated in Fig. 4.14, which clearly demonstrates that V_B increases almost linearly with decreasing device area [A= ($\pi d^2/4$)]. Since the total number of dislocations increases linearly with the device area, the behavior shown in Fig. 4.14 is related only with the presence of threading dislocations. The result thus suggests that the device performance can be further improved by improving material quality through dislocation reduction and device size and geometry optimization. The breakdown field of dislocation-free AlN epilayers can be obtained by extrapolating V_B to A=0, which is about 4.1 MV/cm.

In summary, we have demonstrated the linear mode operation of AlN based APDs which possess the shortest cutoff wavelength of 210 nm. The photocurrent multiplication reached a value of 1200 under −250 V (E_b=2.8 MV/cm) reverse bias. Also, the device size dependent breakdown field suggests that Geiger mode operation could be achieved by further reducing the dislocation density and optimizing device size and geometry. These results further demonstrate that AlN is an excellent active DUV material for future DUV optoelectronic device applications.

CHAPTER 5-InGaN/GaN MQWs Solar Cells

5.1 Introduction

Solar cells have been established as a major candidate for obtaining energy from the sun, the only long-term natural resource. A solar cell is a solid state device which directly converts sunlight into electricity with high conversion efficiency and is virtually free of pollution. Solar cells work on the principle of the photovoltaic effect, which generates voltage when the device is exposed to light. So far solar cells have been made from many semiconductors such as Si, Ge, CdS, GaAs using different device configurations and employing single-crystal, poly-crystal, and amorphous thin-film structures. The solar cell is assumed to have ideal diode I-V characteristics and the performance of solar cell under illumination can be completely described by I-V characteristics. The equivalent circuit and typical I-V curves of a solar cell are shown in Figs. 5.1 (a) and (b), respectively.

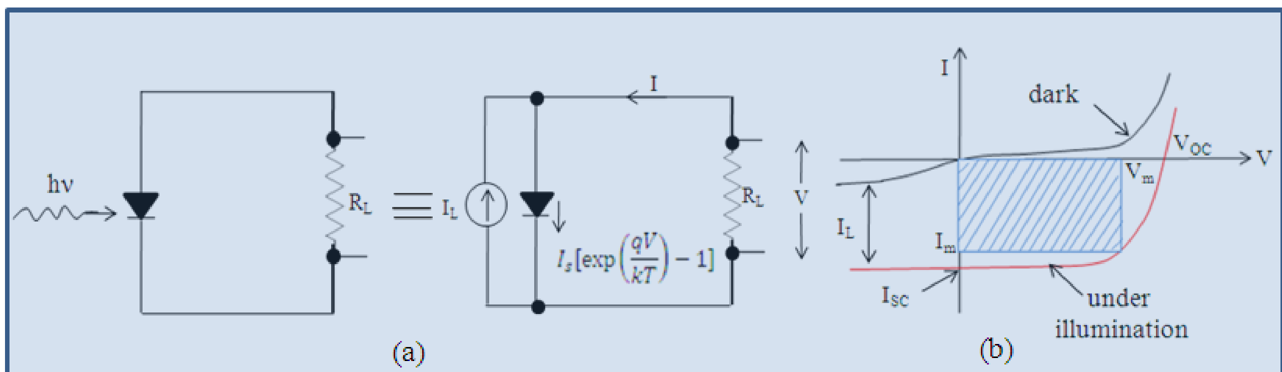

Fig. 5.1 (a) Idealized equivalent circuit and (b) a typical I-V characteristics of solar cell under illumination.

The source current (I_L), results from the excitation of excess carriers generated by solar radiation, and diode saturation current (I_S) is related to the total current (I) by the relation:

$$I = I_S \left[\exp\left(\frac{qV}{kT}\right) - 1\right] - I_L \quad (5.1)$$

where k is Boltzman constant and V is the voltage across the diode. The complete electrical behavior of a solar cell can be described by three parameters: short circuit current (I_{SC}), open circuit voltage (V_{OC}), and fill factor (FF).

I_{SC}, obtained by setting V=0 in Eq. (5.1), is equal to the light generated current I_L if the diode series resistance R_s=0 (ideal case). However, for real devices, a finite value of R always exist, and reduces I_{SC}. V_{OC} can be obtained by setting I=0 in Eq. (5.1), which is given by

$$V_{OC} = \frac{kT}{q} \ln\left(\frac{I_L}{I_S} + 1\right) \quad (5.2)$$

For a given I_L, V_{OC} increases logarithmically with decreasing I_s, but I_s decreases exponentially with the energy bandgap of the semiconductor. So solar cells using large bandgap materials have higher V_{OC}. The maximum V_{OC} is approximately equal to the built-in potential, which is close to the energy bandgap.

The overall performance of a solar cell is determined by the fraction of the total power of incident light that can be converted into electrical power. Under illumination, the junction is forward biased and the external load resistance (R_L) determines the operating point in the I-V

curve. In general, solar cells are operated under conditions of maximum power output. $P_{max}=V_mI_m$ which is related to FF by the relation

$$FF = \frac{V_m I_m}{V_{OC} I_{sc}} \tag{5.3}$$

Now the power conversion efficiency of a solar cell is given by

$$\eta = \frac{V_m I_m}{P_{in}} = \frac{FF\, V_{OC} I_{sc}}{P_{in}} \tag{5.4}$$

where P_{in} is the total incident power. For real devices, the efficiency is determined by important material parameters such as lifetime, the mobility of minority charge carriers, and the surface recombination velocities.

5.2 InGaN/GaN MQWs Solar Cells with Long Operating Wavelength

InGaN alloys have been widely utilized as active materials for LEDs and LDs, covering emission wavelengths from near UV to green spectral regions [115-120]. InGaN alloys recently emerged as a new solar cell materials system due to their tunable energy bandgaps (varying from 0.7 eV for InN to 3.4 eV for GaN, covering almost the whole solar spectrum) and superior photovoltaic characteristics (direct energy band gap in the entire alloy range and high carrier mobility, drift velocity, radiation resistance, and optical absorption of $\sim 10^5$ cm^{-1} near the band edge) [24, 26-29].

Although InGaN based solar cells offer tremendous potential for terrestrial as well as space photovoltaic applications, there are only a few reports on InGaN based solar cells.

Furthermore, most recently reported InGaN solar cells have In contents lower than 15% and band gaps near 3 eV, or larger, and therefore deliver diminishing quantum efficiency at wavelengths longer than 420 nm [24, 26-29]. An earlier theoretical calculation has indicated that the requirements for an active material system to obtain solar cells having solar energy conversion efficiency greater than 50% can be fulfilled by InGaN alloys with In content of about 40% [121]. Additionally, III-nitride multijunction solar cells with near ideal bandgaps for maximum solar energy conversion efficiency must incorporate InGaN layers with higher In contents or lower energy bandgaps.

However, the realization of high crystalline quality InGaN films in the entire composition range is highly challenging. One of the biggest problems is attributed to the large lattice mismatch between InN and GaN (mismatch ~10%) resulting in low solubility and phase separation [122, 123]. Recently, our group has shown that by directly depositing on GaN/Al_2O_3 or AlN/Al_2O_3 templates without buffer layers, single phase InGaN epilayers across the entire

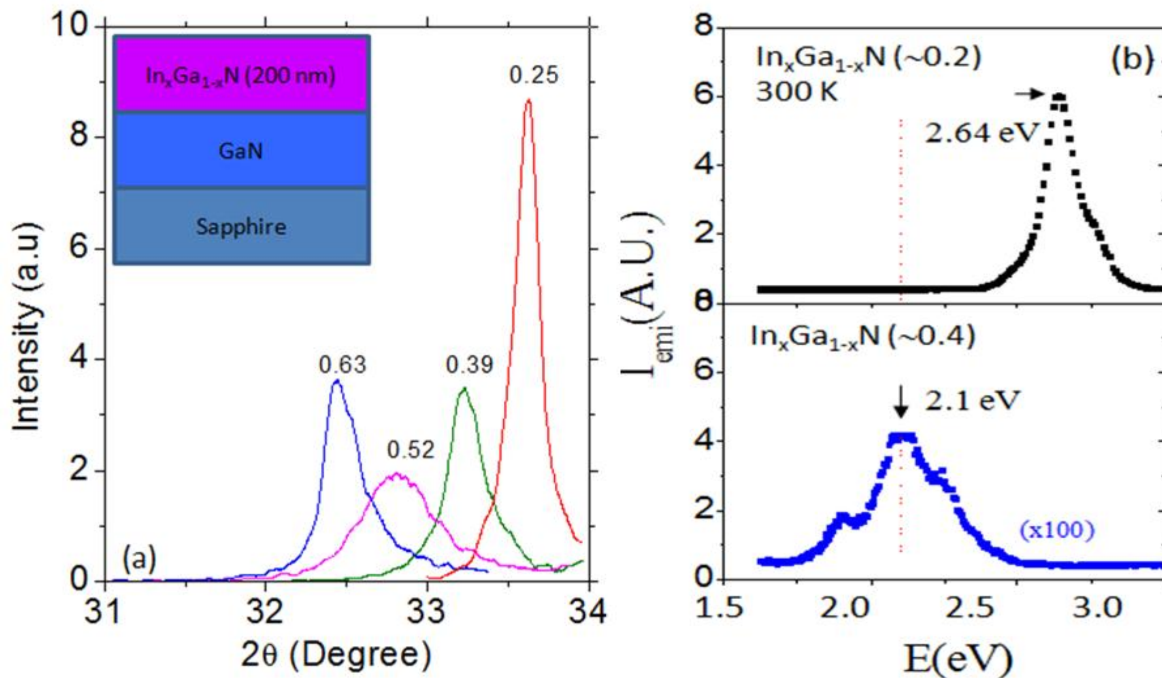

Fig. 5.2 (a) XRD Θ-2Θ curves of (002) planes (b) PL emission spectra of representative $In_xGa_{1-x}N$ epilayers (0.2 μm thick) grown on GaN/Al_2O_3 templates.

alloy range could be produced by MOCVD [124]. This fact is illustrated in Fig. 5.2 (a), where x-ray diffraction (XRD) data for Θ-2Θ scans of the (002) plane for several representative $In_xGa_{1-x}N$ epilayers (200 nm thick) are shown. All curves scanned down to the InN peak position exhibit no multiple peaks, implying that our $In_xGa_{1-x}N$ epilayers are not phase separated. The results represent a significant advancement of the MOCVD growth of InGaN alloys. However, the film homogeneity is still poor in the middle composition range. The full width at half maximum of the rocking curves of ω-scans on the (002) reflection increases from around 1000 arcsec at x~0.2 to about 3000 arcsec at x~0.5 for films of about 0.2 μm in thickness [124]. The PL emission properties of $In_xGa_{1-x}N$ epilayers also deteriorate with an increase in x. For instance, as shown in Fig. 5.2 (b), the overall PL emission intensity of $In_{0.4}Ga_{0.6}N$ films is about 100 times lower than that of $In_{0.2}Ga_{0.8}N$. This trend of reduced crystalline quality with increasing x makes the realization of solar cells based on $In_xGa_{1-x}N$ with x>0.25 highly challenging. Evidence that strain could suppress phase separation in InGaN has been reported by various groups. It was shown that InGaN alloys across the entire composition range without phase separation can be grown when the layer is embedded within an InGaN/GaN double heterostructure [125, 126]. In this work, we discuss on the fabrication and characterization of InGaN solar cells by utilizing $In_xGa_{1-x}N$/GaN MQWs with the attempt to alleviate to a certain degree the phase separation issue and demonstrate solar cell operation in wavelengths longer than that of previous attainments.

5.3 InGaN/GaN MQWs Solar Cells: Growth & Fabrication

The solar cell layer structure is shown in Fig. 5.3 (a), and the light absorbing region consists of eight periods of $In_xGa_{1-x}N$ (3 nm)/GaN (8 nm) MQWs. The MQWs were grown under the established MOCVD growth conditions of $In_xGa_{1-x}N$ epilayers [124] with targeted x values of

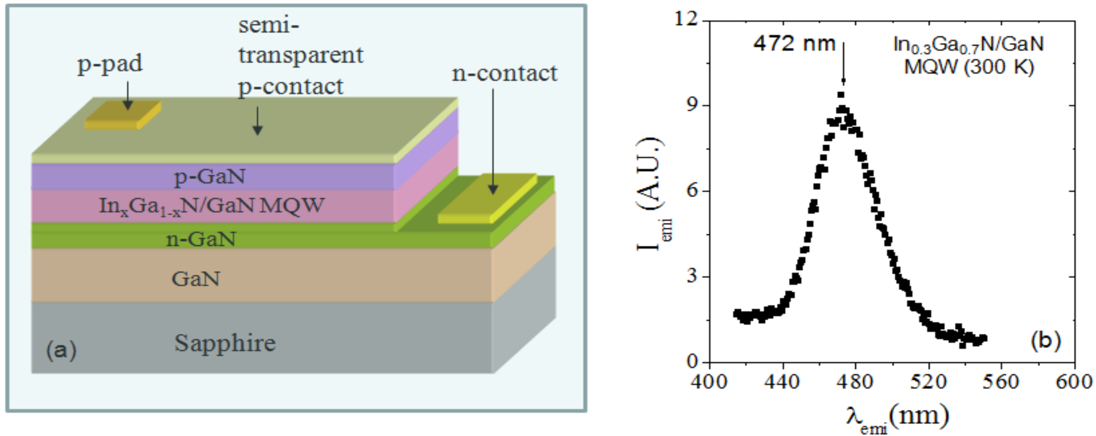

Fig. 5.3 (a) Schematic layer structure of solar cells based on InGaN/GaN MQWs (b) PL emission spectrum of an $In_xGa_{1-x}N$/GaN MQW (x~0.3) solar cell structure.

0.3 and 0.4, with the aim of obtaining photovoltaic responses in longer operating wavelengths than previously demonstrated [24, 26-29]. The PL spectrum for an $In_xGa_{1-x}N$/GaN MQW solar cell structure with the targeted In content of 0.3 is shown in Fig. 5.3 (b) and exhibits an emission line around 472 nm (or ~2.63 eV). The thickness of *p*-GaN (*n*-GaN) is ~150 nm (~0.5 μm). The device structure was grown on a GaN epilayer (3 μm)/sapphire template. We adopted the device fabrication steps by implementing a thin Ni/Au (2/6 nm) semi-transparent current spreading layer to minimize the *p*-contact resistance on the *p*-GaN window. An optical microscopy image of a

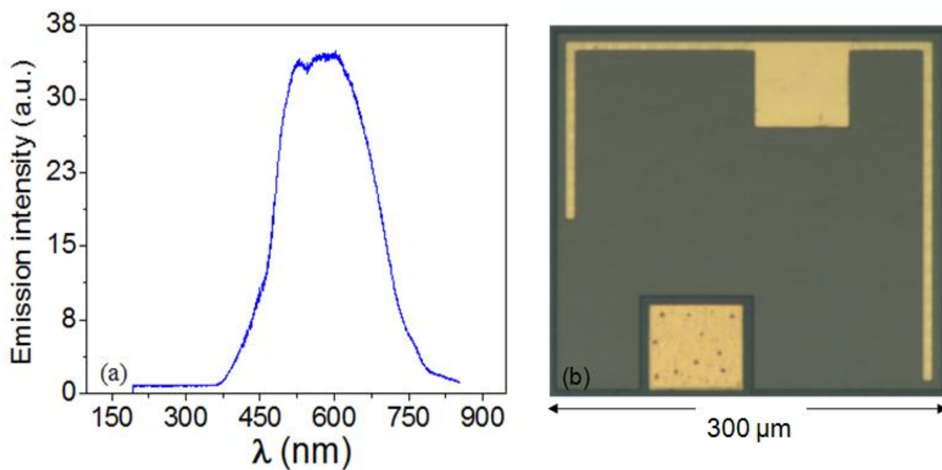

Fig. 5.4 (a) spectrum of the white light source used for *I*-*V* characteristics measurements (b) optical microscopy image of a fabricated device.

fabricated InGaN/GaN MQW solar cell is shown in Fig. 5.4 (b). The devices were characterized using a microprobe station with a source meter (Keithley 2400). For current- and power-density versus voltage characteristics measurements, the solar cell was illuminated by a white light source (with no optical filters), which has an emission spectrum, as shown in Fig. 5.4 (a). For quantum efficiency versus excitation wavelength characterization, monochromatic illumination was obtained by using the same white light source in conjunction with a monochromator (with a spectral resolution of about 2.5 nm).

5.4 InGaN/GaN MQWs Solar Cells: Device Characterization

Current versus voltage (*I-V*) characteristics of two fabricated $In_xGa_{1-x}N$/GaN MQW solar cells with targeted In contents (x) of about 0.3 and 0.4 in the well region are shown in Fig. 5.5 (a). V_{oc} for devices with x~0.3 and 0.4 are about 2.0 and 1.8 V, respectively. These values are in reasonable agreement with the bandgaps of $In_{0.3}Ga_{0.7}N$ and $In_{0.4}Ga_{0.6}N$. However, the

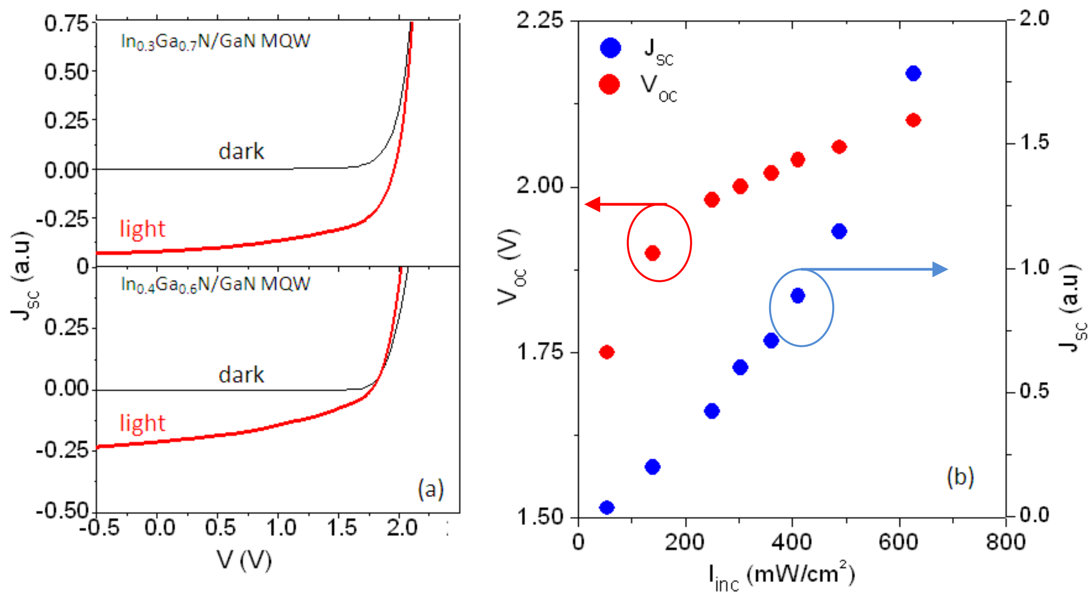

Fig. 5.5 (a) I-V characteristics for a solar cell with $In_xGa_{1-x}N$/GaN MQW (x~0.3 & 0.4) as the active region. (b) J_{sc} (left) and V_{OC} (right) as functions of incident light intensity for $In_{0.3}Ga_{0.7}N$/GaN MQW solar cell.

performance of the lower energy bandgap device (with $In_{0.4}Ga_{0.6}N$/GaN MQWs as active region) is much poorer than that of the higher energy bandgap device (with $In_{0.3}Ga_{0.7}N$/GaN MQWs as active region), despite the fact that $In_{0.4}Ga_{0.6}N$/GaN MQWs are expected to have a much better spectral overlap with the excitation source. This degradation in solar cell performance corroborates the XRD and PL results illustrated in Fig. 5.2 and is a direct consequence of reduced material quality with increasing x, which leads to a higher loss of the photo-generated charge carriers. The photovoltaic characteristics observed here are also consistent with the well established fact that the quantum efficiencies of III-nitride green LEDs are much lower than those of blue LEDs. We have also studied the variation of V_{OC} and J_{SC} with incident light intensity and the results are shown in Fig. 5.5 (b). It is observed in Fig. 5.5 (b) that V_{OC} increases logarithmically (as Eq. 5.2) with I_{inc}, where as J_{SC} increases almost linearly with I_{inc}, which is expected as photo-generated carriers are proportional to I_{inc}.

Current- and power-density versus voltage characteristics for the higher performance

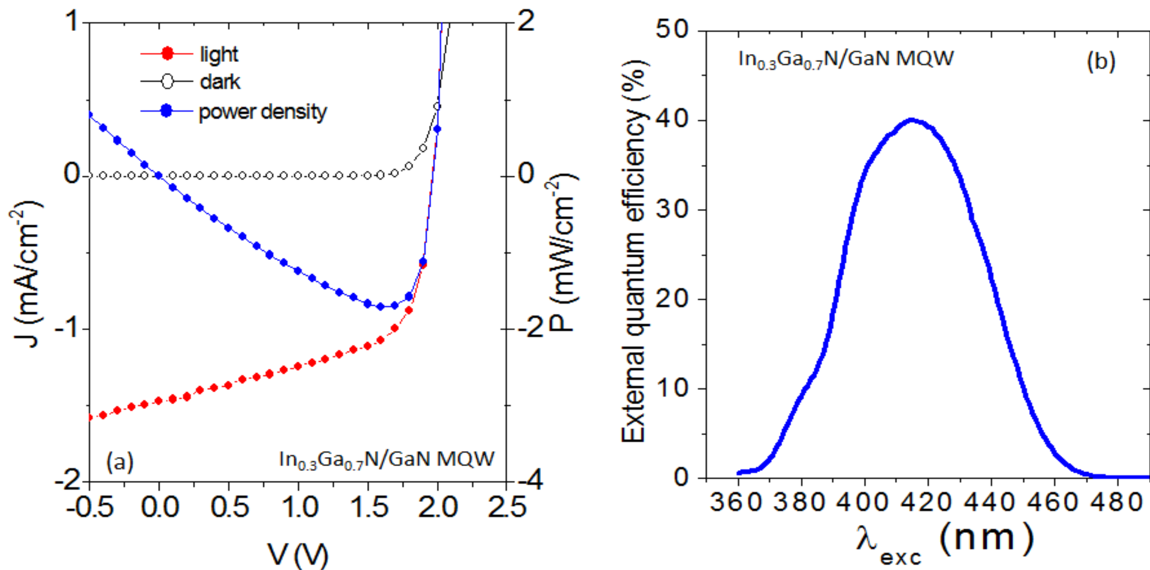

Fig. 5.6 (a) Current- and power-density vs voltage characteristics for a solar cell with $In_xGa_{1-x}N$/GaN MQW (x~0.3) as the active region. (b) External quantum efficiency vs excitation wavelength for the same device.

device (with $In_{0.3}Ga_{0.7}N$/GaN MQWs as active region) are plotted in Fig. 5.6 (a), from which a fill factor of about 60% is obtained. The quantum efficiency as a function of excitation wavelength for the same device is shown in Fig. 5.6 (b), which demonstrates that the device delivers a quantum efficiency of 40% at 420 nm and 10% at 450 nm. The response in the shorter wavelength region (<300 nm) is limited by the use of *p*-GaN window [28] and could be improved if a larger energy bandgap material such as *p*-AlGaN or *p*-InAlGaN were incorporated. Three major quantum efficiency limiting factors include the following: (1) Absorption in the semitransparent *p*-contact layer—the current spreading *p*-contact layer was simply adopted from LED fabrication and the *p*-contact schemes need to be optimized for solar cell applications. (2) Thin light absorption layer—the optical absorption layer thickness is too thin in the present MQW structure. The well/barrier thickness and period of the MQW active region need to be optimized to maximize light absorption but minimize other detrimental effects due to the incorporation of relatively high In content InGaN alloys in the well region. (3) Low crystalline quality of InGaN alloys with relatively high In contents—this remains as one of the most challenging issues for the nitride research community. Nevertheless, this is the first demonstration of InGaN based solar cells with good external quantum efficiencies at such long operating wavelengths, which suggest that MQW is a viable approach to design high efficiency solar cells based on InGaN with relatively high In contents for optimal solar energy conversion.

In summary, we have discussed the growth and fabrication of InGaN/GaN MQW based solar cells incorporating InN factions of 30% and 40%. The devices exhibit a fill factor of about 60% and deliver an unprecedented external quantum efficiency of 40% at 420 nm and 10% at 450 nm.

CHAPTER 6-1.54 μm Emitter and Optical Amplifier based on Er doped InGaN/GaN

6.1 Introduction

Due to advances in semiconductor photonic device fabrication techniques and design, much research has been devoted to the incorporation of Erbium (Er) into semiconductors aimed at achieving photonic integrated circuits with multiple functionalities [40, 127], which are not possible to attain from either Er-doped silica glasses or narrow bandgap semiconductor materials such as InGaAsP. The optical sources and amplifiers operating at 1.54 μm based on Er-doped semiconductors, if obtained, will be electrically pumped, integratable, and cost effective, along with the performance benefits of linear gain, temperature insensitivity, and low noise. These characteristics are extremely attractive for local- and wide-area networks, cable TV distribution, and anticipated fiber-to-the-home applications where multiple amplification steps are required.

Although the wavelength of emission is not affected by the solid host, the transition probability (i.e., emission intensity) is affected by the neighboring environment. It has been universally observed that the 1.54 μm emission from Er in semiconductors of smaller bandgaps has a low efficiency at room temperature (RT) due to a strong thermal quenching effect. In general, the thermal stability of Er emission increases with an increase in the energy bandgap and the crystalline quality of the semiconductor host material [37]. Of the various wide bandgap semiconductor systems, III-nitrides appear to be an excellent host system for Er ions due to their structural and thermal stability as well as their ability to create efficient light emitting devices.

Until recently, it has been a great challenge to incorporate Er ions into III-nitride materials to produce predominantly 1.54 μm emissions by any growth method. Previous work

has been concentrated on the optical property studies of Er dopants with samples doped either by ion implantation or by *in situ* doping using the molecular beam epitaxy (MBE) growth technique [36, 37, 43, 128-134]. GaN and AlGaN epilayers doped with Er ions have shown a highly reduced thermal quenching of the Er luminescence intensity from cryogenic to elevated temperatures when compared to other semiconductor host materials such as Si and GaAs [135]. There have also been reports of Er incorporation into by MBE, leading to 1.54 μm electroluminescent devices [36]. However, all such devices require high field injection of electrons under reverse bias (several hundred volts) to produce infrared (IR) emission at 1.54 μm (no 1.54 μm emission was observed under forward bias conditions). Under such reverse bias conditions, the excitation of Er ions was through an impact energy transfer mechanism. Furthermore, these devices suffer from strong emission lines in the visible region, severely limiting their prospects for practical devices in optical communication applications. Compared to ion implantation, *in situ* doping provides, in principle, precise control of Er dopants position in the device structure. In contrast to other epitaxial growth techniques, MOCVD is the established growth method in the III-nitride semiconductor industry and almost all commercial III-nitride photonic devices including light emitting diodes (LEDs) and laser diodes (LDs) are grown by MOCVD technique [1].

Our group has synthesized by MOCVD GaN:Er epilayers that predominantly exhibit the desired optical emission for optical communication at 1.5 μm [136]. However, true current-injected 1.5 μm LEDs operating under low forward bias voltages have not been realized. We discuss here the MOCVD growth of GaN:Er and InGaN:Er epilayers which predominantly exhibit the desired 1.5 μm emission and fabrication of current-injected 1.54 μm LEDs by heterogeneous integration of GaN:Er (or InGaN:Er) epilayers with III-nitride LEDs. These 1.54

μm LEDs require only a few volts of bias (determined by the nitride LEDs) for operation and are fully compatible with existing optoelectronic devices for scalable integration.

6.2 Growth of GaN:Er and InGaN:Er

GaN:Er and $In_{0.06}Ga_{0.94}N$:Er epilayers of about 0.5 μm in thickness were grown by MOCVD on (0001) GaN/sapphire templates. Growth of these epilayers began with a thin GaN buffer layer, followed by a GaN epilayer template with a thickness of about 1.2 μm and an Er doped GaN layer. The growth temperature of the GaN template and Er doped GaN layer was 1040 ^{O}C. The Er doped $In_{0.05}Ga_{0.95}N$ sample structure was very similar to that of Er doped GaN. Growth of the epilayer began with a thin GaN buffer layer and a 1.2 μm GaN epi-template followed by an Er doped $In_{0.05}Ga_{0.95}N$ layer grown at 760 ^{O}C. The layer structures of GaN:Er and $In_{0.06}Ga_{0.94}N$:Er employed in this study are shown in Figs.6.1 (a) and (b), respectively.

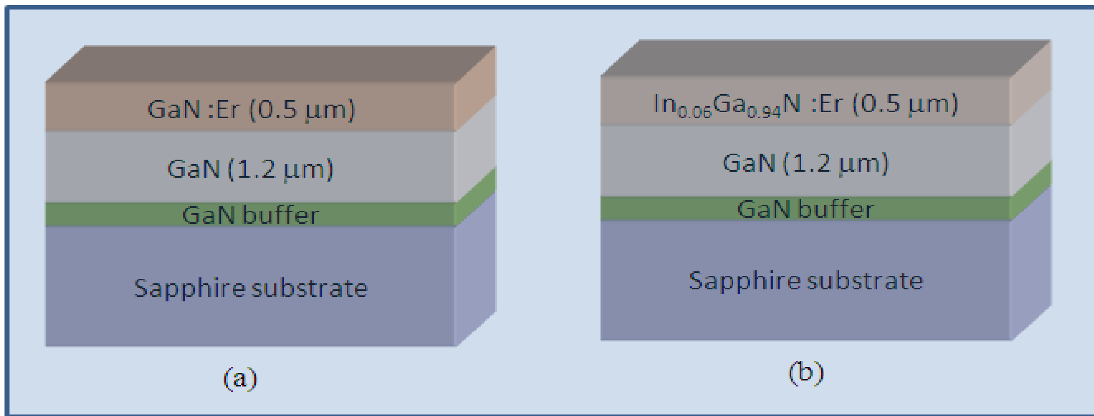

Fig. 6.1 Schematic layer structure of (a) GaN:Er and (b) $In_{0.06}Ga_{0.94}N$: Er epilayers.

6.3 Photoluminescence Excitation (PLE) spectroscopy of GaN:Er and InGaN:Er epilayers

In order to design efficient photonic devices, we have measured the photoluminescence excitation (PLE) spectra probed at 1.54 μm and optical absorption spectra of these epilayers to gain further understanding of the mechanisms for obtaining efficient 1.54 μm emission. For PLE spectra measurements, a set of commercially available nitride LEDs was used as the optical

pumping sources with the emission wavelengths (352, 362, 371, 378, 381, 398, 411, 450, 470, and 520 nm) ranged from below to above the bandgap of the GaN and InGaN host epilayers. The typical full width at half maximum (FWHM) of each LED was 15–20 nm. For PLE measurements, Er-doped epilayers were mounted on top of nitride LEDs with a distance of about 2 mm from LED's top surface. The IR emission was detected by an InGaAs detector in conjunction with a monochromator, while visible emission was detected by a multichannel plate photomultiplier tube (PMT) in conjunction with another monochromator. The absorption spectra were measured using a deuterium light source in conjunction with a monochromator and PMT.

Figure 6.2 (a) shows the RT emission spectra of a GaN:Er epilayer under excitation with nitride LEDs of different wavelengths. The emission spectra were taken with the under constant

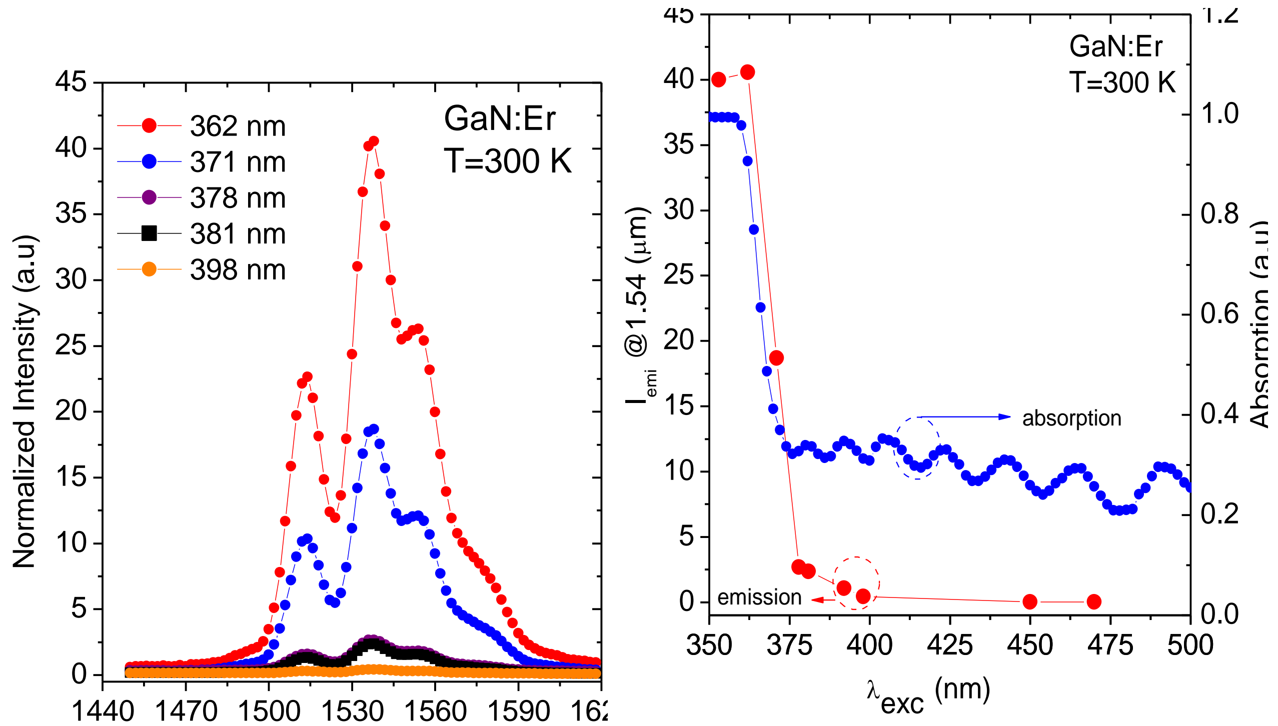

Fig. 6.2 (a) RT emission spectra near 1.54 μm of GaN:Er epilayer with III-nitride LEDs excitation. The excitation wavelengths (λ_{exc}) varies from 362 to 470 nm, corresponding to energies from below to above bandgap of the host GaN and the emission intensities were normalized to the LED optical power outputs, (b) PLE spectrum probed at 1.54 μm (left axis) and optical absorption spectrum (right axis) of GaN:Er. Fringes in the absorption spectrum are due to thin film (GaN:Er) interference effects.

current of 20 mA and were normalized to the optical power output of each LED. The emission spectra clearly demonstrate that the emission intensity increases sharply as the excitation energy (E_{exc}) approaches the bandgap of GaN (~3.35 eV or ~370 nm at RT) from below. This point is further supported by the PLE and optical absorption spectra shown in Fig. 6.2 (b). The PLE spectrum probed at 1.54 μm shows that the onset excitation wavelength for obtaining efficient 1.54 μm emission is λ_{exc}<370 nm and the emission intensity at 1.54 μm saturates for λ_{exc}<362 nm. Moreover, there is a little or no emission from excitation for λ_{exc}>400 nm. Compare the PLE spectrum measured at 1.54 μm and absorption spectrum of GaN:Er, a strong correlation between the two is evident. The two spectra follow exactly the same trend near the energy bandgap of GaN. These results clearly demonstrate that, in GaN:Er epilayers, excitation of free electrons and holes with above bandgap excitation and the subsequent energy transfer to Er^{3+} ion from electrons and holes is much more efficient compared to below bandgap excitation. These excited Er^{3+} ions emit photons at 1.54 μm due to intra-4*f*-transition of $^4I_{13/2}$ level to the ground state ($^4I_{15/2}$).

To further confirm these results, we have also grown and carried out similar measurements for $In_{0.06}Ga_{0.94}N$:Er epilayers. The relative emission intensity at 1.54 μm in $In_{0.06}Ga_{0.94}N$:Er epilayers is about three times weaker than that in GaN:Er epilayers. The PLE and optical absorption spectra of Er-doped $In_{0.06}Ga_{0.94}N$ epilayers show similar features as those of Er-doped GaN epilayers. The PLE spectrum probed at 1.54 μm and optical absorption spectrum of an $In_{0.06}Ga_{0.94}N$:Er epilayer are plotted in Fig. 6.3. It is evident that PLE and absorption spectra are again strongly correlated, especially near the energy bandgap of $In_{0.06}Ga_{0.94}N$, which is about 3.18 eV (~390 nm) at RT. In general, $In_{0.06}Ga_{0.94}N$:Er exhibits a similar trend as that observed in GaN:Er shown in Fig. 6.2 (b), except that the onset excitation energy for obtaining an efficient

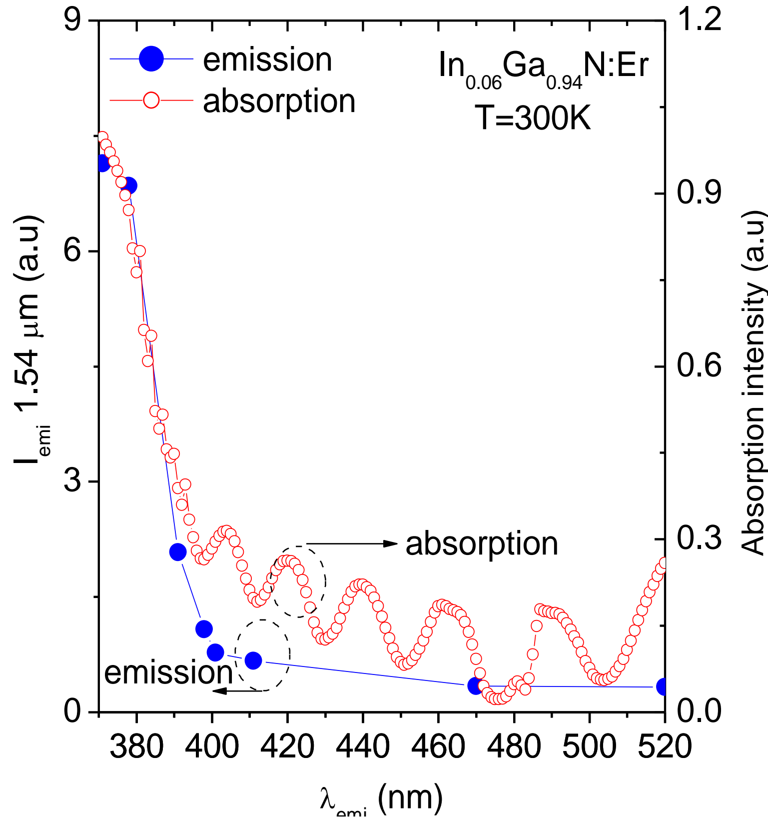

Fig. 6.3 PLE spectrum probed at 1.54 μm (left axis) and absorption spectrum (right axis) of a $In_{0.06}Ga_{0.94}N$:Er epilayer. Emission intensity at 1.54 μm, I_{emi}, increases sharply for excitation energy greater than 3.18 eV (λ_{exc}<390 nm) corresponding to the RT bandgap of $In_{0.06}Ga_{0.94}N$.

1.54 μm emission is reduced because of the smaller bandgap of $In_{0.06}Ga_{0.94}N$ than GaN (~3.18 eV for $In_{0.06}Ga_{0.94}N$ versus ~3.35 eV for GaN). The results obtained for $In_{0.06}Ga_{0.94}N$:Er further support the conclusion that the electron and hole energy transfer to Er^{3+} ions is much more effective than below bandgap excitation.

6.4 Current injected 1.54 μm emitter based on Er doped GaN: Fabrication and Characterization

The optical results shown in Figs. 6.2 and 6.3 indicate that efficient current-injected 1.54 μm emitters and optical amplifiers could be obtained by monolithically or heterogeneously integrating highly efficient UV/blue/green nitride LEDs or LDs with InGaN:Er or GaN:Er epilayers. Based on the PLE results for obtaining the most efficient 1.54 μm emission, current-injected 1.54 μm emitters were fabricated by heterogeneously integrating GaN:Er (or InGaN:Er)

epilayers with 365 nm nitride LEDs. The integration process started with the back polishing of GaN:Er grown on sapphire wafer down to ~100 μm and then dicing into 500×500 μm^2 chips. The diced chip was then bonded onto a 365 nm nitride LED chip using UV transparent epoxy with GaN:Er surface facing the LED. There was a distance of about 0.5 mm between the GaN:Er epilayer and top surface of the LED chip due to the presence of epoxy. A schematic of the heterogeneously integrated device is illustrated in the inset in Fig. 6.4. These 1.54 μm emitters were characterized in terms of spectral and power emission under different current levels at

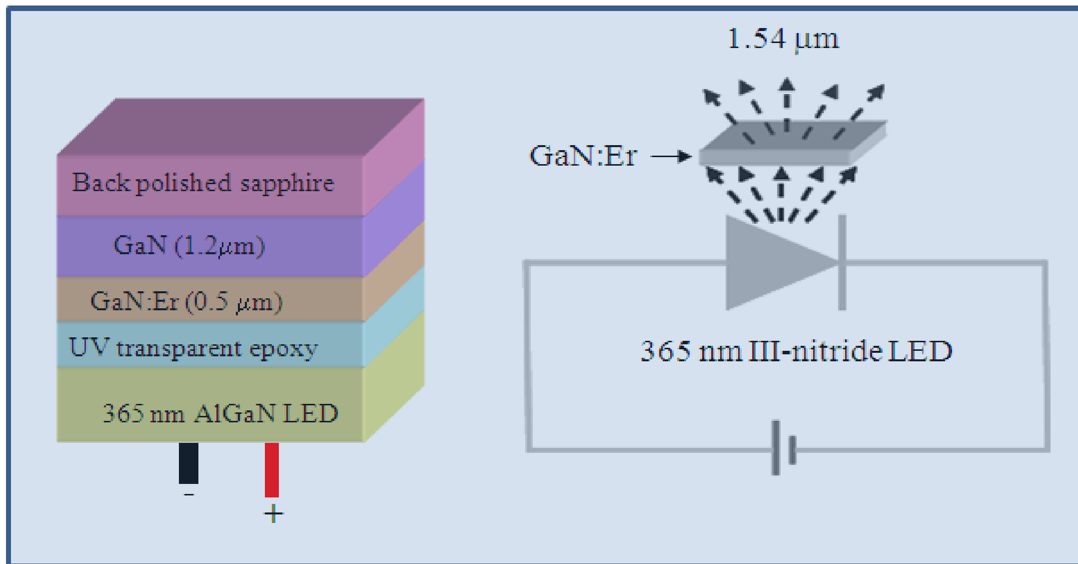

Fig. 6.4 Schematically illustrates that the 1.54 μm LED is fabricated by heterogeneous integration of a GaN:Er epilayer with a 365 nm III-nitride LED.

forward bias. Figure 6.5 (a) shows the IR emission spectra of a heterogeneously integrated device under different injection current levels at forward bias. The inset in Fig. 6.5 (a) shows that no Er-related emission in the visible spectral range (between 420 and 850 nm) were observed. The emission intensity at 1.54 μm increases almost linearly with the input current, as shown in Fig. 6.5 (b). The attainment of current-injected 1.54 μm emitters by heterogeneous integration here suggests that it is highly feasible to directly grow Er-doped nitride layers either on the top or on

the back side of the polished sapphire substrate of UV/blue/green nitride LED structure to achieve monolithic current-injected 1.54 μm optical emitters. It also appears feasible to obtain current-injected optical amplifiers based on GaN:Er (or InGaN:Er) waveguide layer deposited on top of a completed III-nitride UV (blue) emitter structure or AlGaN/(In)GaN:Er/AlGaN *p-i-n* quantum well (QW) structure. Such a development would require further improvements in GaN:Er and InGaN:Er epilayer quality and device architectures. In particular, it will be a challenging task to obtain highly conductive *p*-type AlGaN (GaN) cladding layers above GaN:Er (InGaN:Er) QW active region.

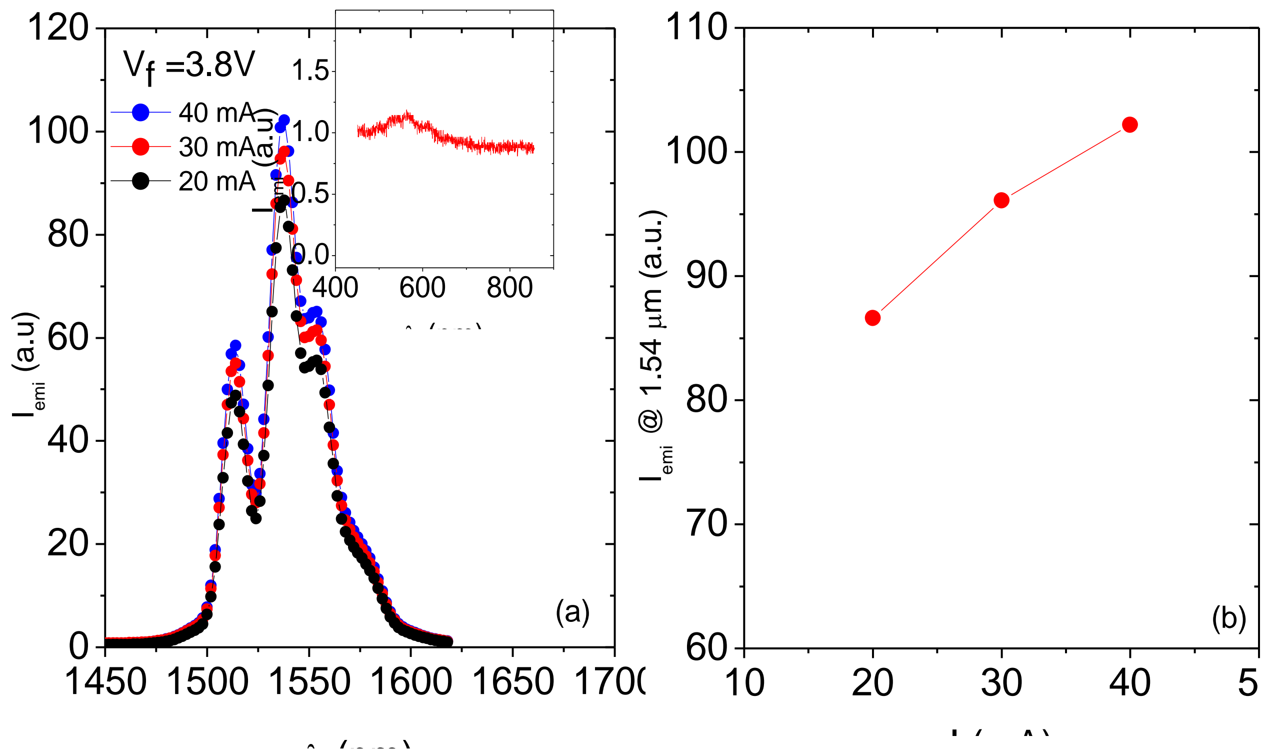

Fig. 6.5 (a) IR emission spectra of a current-injected 1.54 μm LED under different injection current levels. The inset is the visible emission spectrum of the same device, showing virtually no Er-related emission in the spectral range of 430–850 nm. (b) Emission intensity (I_{emi}) of the same 1.54 μm LED as a function of the forward injection current.

In summary, we have fabricated current-injected 1.54 μm LEDs based on heterogeneous integration of MOCVD grown Er-doped III-nitride epilayers with III-nitride UV LEDs. The Er emission intensity at 1.54 μm increases significantly as the excitation energy is tuned from below to above the energy bandgap of these epilayers, indicating that the band-to-band excitation of the host material and subsequent electron and hole mediated energy transfer to Er^{3+} ions is a much more effective excitation mechanism for 1.54 μm emission than below bandgap excitation. It was shown that the 1.54 μm emission intensity increases almost linearly with the input forward current. These results open up possibilities for developing next generation IR photonic devices based on Er-doped III-nitride materials such as 1.54 μm emitters and optical amplifiers for optical communications that possess the advantages of both semiconductor optical amplifiers (small size, electrical pumping, ability for photonic integration, etc.) and Er-doped fiber amplifiers (minimal cross-talk between different wavelength channels in wavelength-division multiplexing optical networks).

6.5 1.54 μm Er doped GaN/AlGaN Waveguide Optical Amplifiers

Er doped fiber amplifiers are part of a well established technology for long distance optical communications near 1.54 μm. They offer stable and low-noise amplification properties due to the atomic intra-4*f* transition of Er^{3+}. However, the narrow band and extremely small absorption cross section (~10^{-21} cm^{-3}) require not only long interaction distance but also a precisely tuned, powerful external laser excitation source. Such requirements hinder the realization of compact and inexpensive Er-doped waveguide amplifiers (EDWAs), which are a key component for local and wide area networks, cable television distribution, and anticipated fiber-to-the-home applications where multiple amplification steps are required. Optical waveguide amplifiers based on rare-earth-doped silica glasses, ceramics, and polymers have been

demonstrated and widely studied [137-141]. However, these waveguide amplifiers need high power laser excitation and relatively long cavities to achieve net optical gain. Earlier reports addressed increasing the absorption cross section by introducing Yb^{3+} as a sensitizer in Er-doped host medium (silica glasses) and demonstrated optical gain with 477 nm broadband LEDs excitation [142]. While prior EDWA research has focused on Er-doped silica glasses, silicon, or polymers [143, 144], our focus here is on EDWAs operating near 1.54 μm based on the III-nitride materials system.

Rare-earth-doped III-nitride wide bandgap semiconductors have potential applications in areas ranging from highly dense photonic integrated circuits (PICs) with multiple functionalities to full color display system, which are not possible to attain either with Er-doped silica glasses or narrow bandgap semiconductors such as InGaAsP. Planar waveguide amplifiers based on Er doped III-nitride materials, are expected to show better performance in terms of linear gain response, temperature insensitivity, and low noise. These are fundamental characteristics of waveguide amplifiers, a key component of chip size PICs, operating in the c-band communication wavelength region (1530–1550 nm). The III-N material system is essentially transparent in this wavelength range and optical signal absorption is expected to be negligible since the material band gap is far from the signal wavelength.

In the previous sections we have discussed the MOCVD growth of GaN:Er and InGaN:Er epilayers with excellent optical qualities and demonstrated a host bandgap-mediated excitation of Er^{3+} in these epilayers with a predominate optical emission at 1.54 μm [136, 145, 146]. Much research on Er-doped GaN/AlGaN has concentrated on the growth and optical properties for application in full color display systems [36, 43]. There appears to be no report of EDWAs based

on Er-doped GaN. We discuss here on the MOCVD growth of AlGaN/Er:GaN/AlGaN heterostructures and their processing into strip waveguides. We have measured their low optical loss properties and demonstrated optical signal enhancement at 1.54 μm under broadband LED excitation.

6.6 Er doped GaN/AlGaN Optical Waveguide Amplifier: Growth and Fabrication

The multilayer structure of optical waveguide devices consists of 0.5 μm $Al_{0.03}Ga_{0.97}N$ top cladding, 0.5 μm GaN:Er optically active core medium, and 1.5 μm $Al_{0.03}Ga_{0.97}N$ bottom cladding grown on *c*-plane sapphire substrate by MOCVD. The Er concentration in the active waveguide core medium was ~10^{21} cm^{-3}. The details of the MOCVD growth of GaN:Er epilayers can be found in our earlier publications [136, 145]. The strip waveguides were fabricated using standard optical lithography and inductively coupled plasma (ICP) dry etching techniques, followed by the deposition of a 250 nm SiO_2 passivation layer by PECVD.

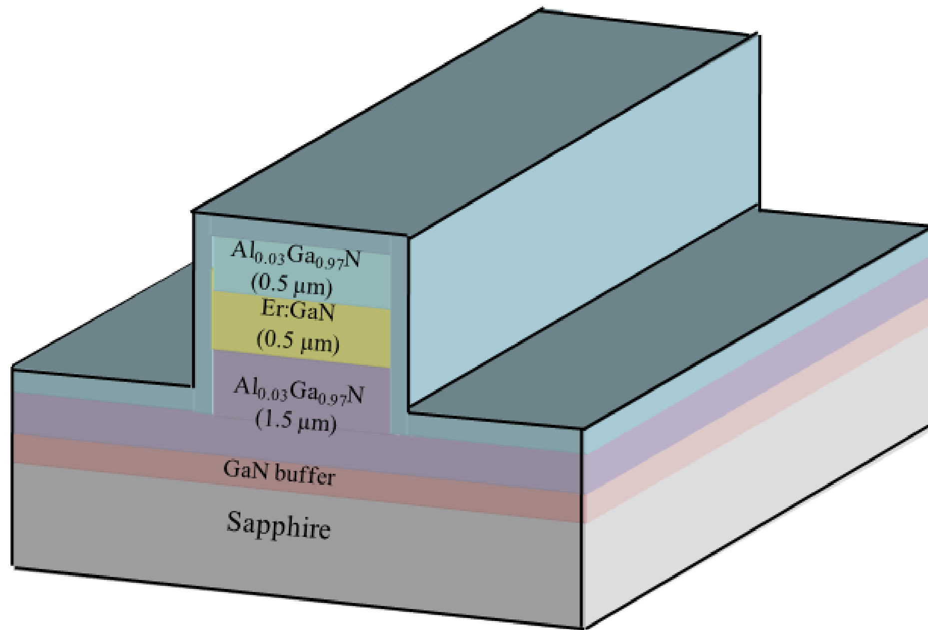

Fig. 6.6 Schematic layer structure of fabricated strip Er-doped GaN waveguide amplifier, which utilizes GaN:Er as optical gain medium with $Al_{0.03}Ga_{0.97}N$ as top and bottom cladding layers.

Figure 6.6 shows a schematic of the multilayer structure of the fabricated strip waveguide. The waveguide width is about 5 μm and the etching depth is ~2 μm. Waveguide facets were prepared by polishing vertically mounted waveguides using diamond paste and finally lapping on a cotton pad with silica solution. The length of the prepared waveguides was ~3 mm. Figure 6.7 contains an AFM image of an array of fabricated waveguides. The optical microscopy image of polished facets is shown in the inset of Fig. 6.7.

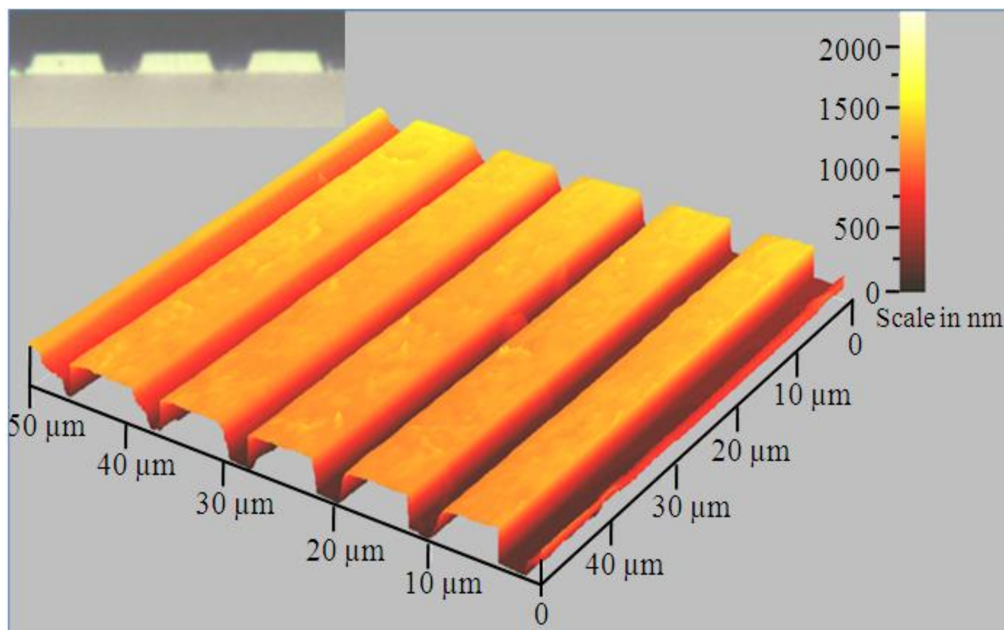

Fig. 6.7 Atomic force microscopy image of fabricated devices. The inset shows the optical microscopy image of waveguide facets prepared by mechanical polishing.

6.7 Er doped GaN/AlGaN Optical Waveguide Characterization: Optical Loss and Signal Amplification Measurement

To measure the optical loss in a fabricated waveguide, one end of the waveguide was illuminated from the top side by a 371 nm nitride laser beam to excite Er^{3+} ions and to generate 1.54 μm light within the waveguide. The beam diameter spot size was ~10 μm. The 1.54 μm light emission propagated through the waveguide and was collected from the far end using

tapered fiber coupled with a monochromator and an InGaAs detector. Figure 6.8 (a) shows the 1.54 μm PL spectra measured at room temperature from the far end of waveguide after excitation by the 371 nm laser beam. The inset in Fig. 6.8 (a) shows an illustration of the setup for the

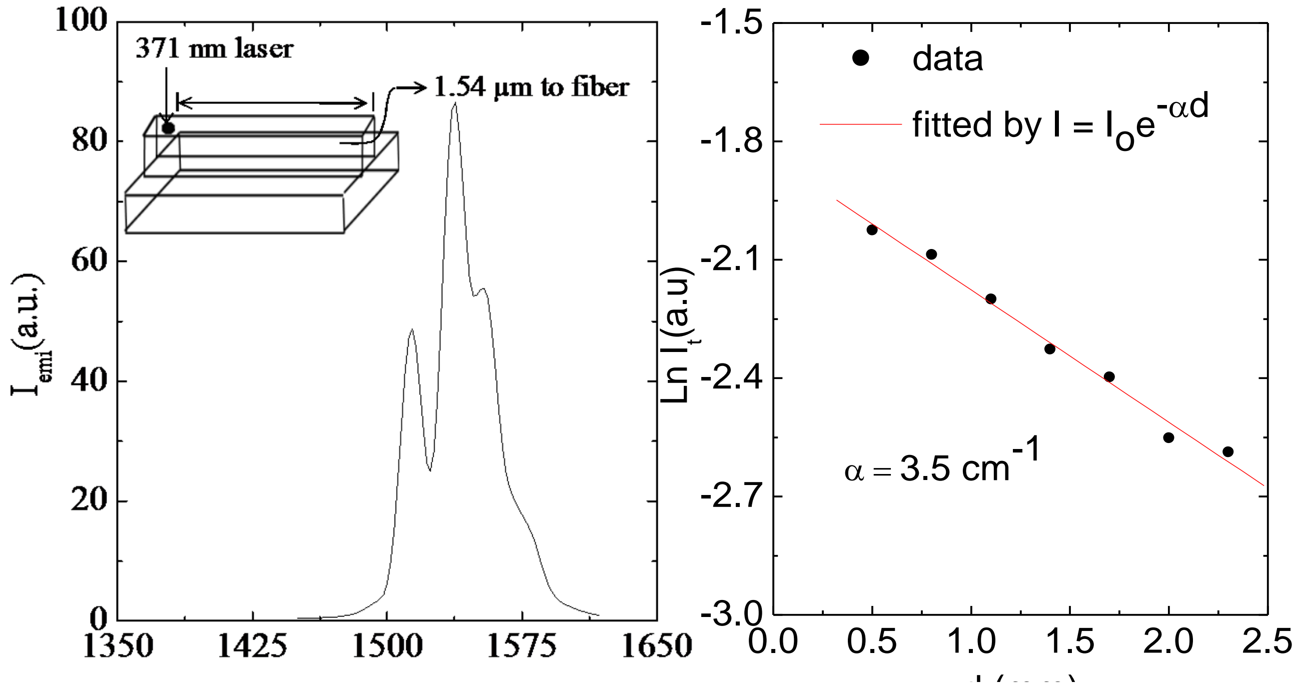

Fig. 6.8 (a) PL spectra of Er-doped GaN waveguide amplifier taken from the end facet of the waveguide when the other end is illuminated by a 371 nm nitride laser. 1.54 μm emission was generated at the laser excitation spot within the core of the waveguide and guided to the end facet of the waveguide. The inset shows the optical loss measurement setup, and (b) plot of 1.54 μm peak intensity as a function of laser excitation spot distance, *d*. The slope of the plot gives the optical loss, which is about 3.5 cm^{-1}.

optical loss measurement. PL spectra peak at 1.54 μm corresponding to the intra-4*f* Er^{3+} transitions from the $^4I_{13/2}$ level to the ground state ($^4I_{15/2}$). The integrated PL emission intensity collected at the exit facet of the waveguide is plotted in Fig. 6.8 (b) as a function of laser excitation spot distance, *d*. The emission intensity coming out of the waveguide facet I_t is described by the following relation:

$$I_t = I_0 e^{-\alpha d} \tag{6.1}$$

where I_0 is the PL emission intensity measured at the laser excitation spot, d is the optical path length, and α is the optical loss of the waveguide. From the slope of the plot of ln I_t versus d, the measured optical loss at 1.54 μm of the Er-doped GaN waveguide is about 3.5 cm^{-1}. This is about a factor of 3 larger than the values reported for the state of art Er-doped oxide waveguide amplifiers [147]. The optical loss is mainly due to light scattering by etched sidewalls of the waveguide and can be minimized through techniques such as wavelength selective coating and gentle wet etching following plasma etching, etc. This measured value of optical loss in Er-doped GaN devices is smaller than an earlier reported value of 4.45 cm^{-1} for undoped GaN ridge waveguide devices measured at visible (488 nm) wavelength [148]. The small value of optical loss in GaN:Er waveguide is what we expected because 1.54 μm wavelength is far from the band gap of the guiding medium, GaN (362 nm). This low optical loss at 1.54 μm demonstrates the great promise of GaN:Er waveguides for optical amplification in optical communication networks.

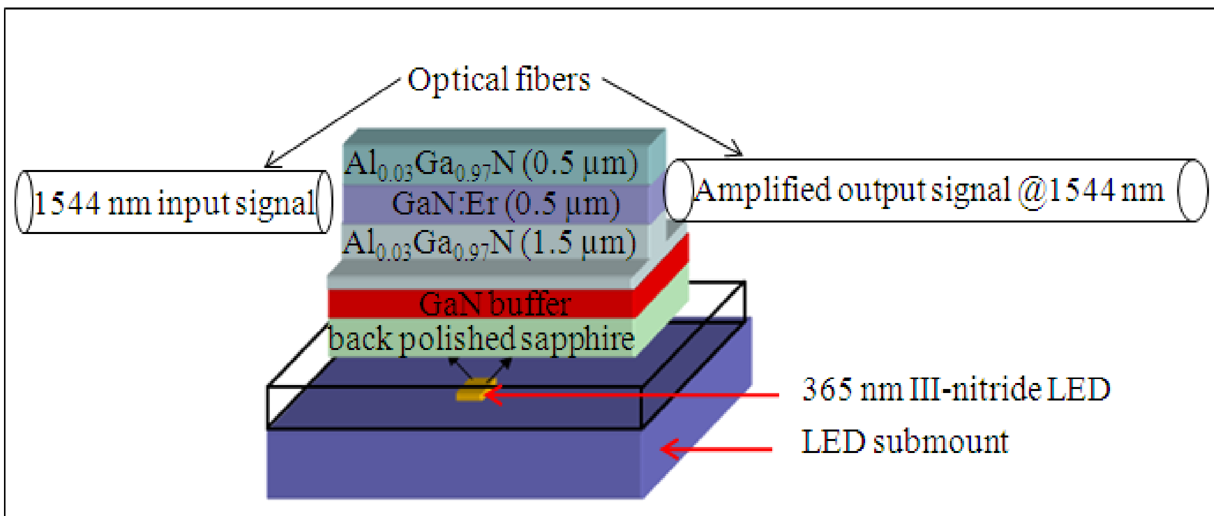

Fig. 6.9 Schematic of the optical amplification property measurement setup. The excitation source is III-nitride high power LEDs.

To study the amplification properties, waveguides were analyzed by studying the relative change in transmitted signal intensity at 1.54 μm. For the optical excitation, a 365 nm GaN LED was used from the bottom side, which is intended to substitute the finely tuned high power laser required for Er-doped silica or ceramic based waveguide amplifier. Figure 6.9 shows the

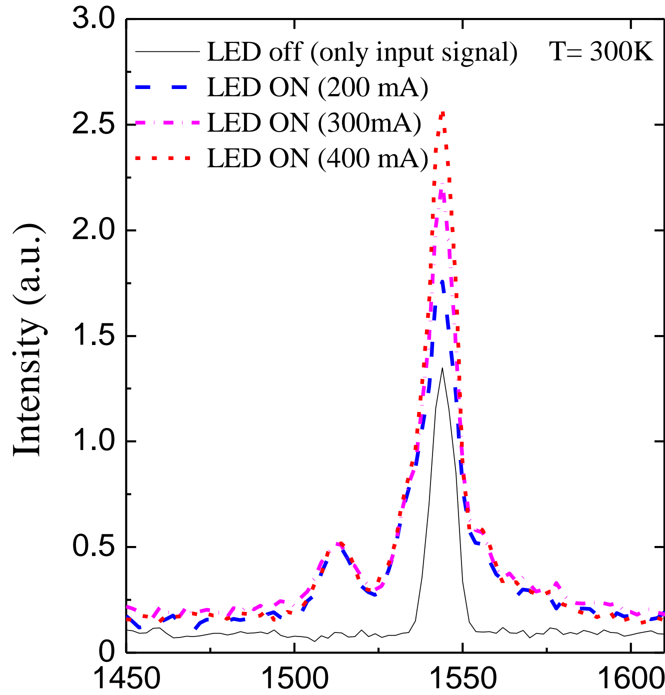

Fig. 6.10 Spectra of the transmitted 1.54 μm signal emerged from the exit end of the Er-doped GaN waveguide measured under the excitation by a 365 nm high power nitride LED operating at different forward currents. The intensity of the 1.54 μm signal guided through the waveguide increases with an increase of the forward current applied to the 365 nm LED, demonstrating a relative signal gain at 1.54 μm.

schematic of the measurement setup employed for optical amplification study. The signal at 1.54 μm from a laser diode was coupled into one end (entrance end) of the waveguide through tapered fiber with a focusing lens at the tip using microscope, *x*-micromanipulator, *y*-micromanipulator, and *z*-micromanipulator. Similarly, the transmitted beam was collected at the other end (exit end) of the waveguide by a tapered fiber with a collecting lens at the tip using another *x*-micromanipulator, *y*-micromanipulator, and *z*-micromanipulator. The exit end of the

fiber was coupled to a monochromator and InGaAs detector. Figure 6.10 shows the transmitted 1.54 μm signal spectra through the waveguide at different levels of 365 nm LED excitation. It is clearly seen that the relative signal intensity at peak signal wavelength (1.54 μm) increases with increasing the excitation intensity of the 365 nm LED. The measured relative signal enhancement is about 8 dB/cm for a 3-mm-long waveguide optically pumped by a 365 nm LED operating at 400 mA.

In summary, we have fabricated optical waveguide amplifiers based on MOCVD-grown Er-doped GaN. The measured optical loss of the fabricated devices was ~3.5 cm^{-1} at 1.54 μm. The optical amplification characteristics of the devices were analyzed by studying the relative change in 1.54 μm input signal intensity transmitted through the waveguide. It was observed that the transmitted 1.54 μm signal intensity through the waveguide was amplified under the excitation of a broadband 365 nm nitride LED and a relative signal enhancement of about 8 dB/cm was observed. The demonstrated 1.54 μm signal enhancement with a broadband LED excitation eliminates the finely tuned high power laser which is required for Er-doped silica glass waveguide amplifier. The results further exhibited the feasibility of achieving compact and cost effective current injected optical waveguide amplifiers based on Er-doped III-nitride semiconductors for future optical communication applications.

CHAPTER 7- Over all Conclusions

III-nitride based photonic/optoeletronic devices such as PDs, solar cells, LEDs and Er doped waveguide amplifiers were designed, fabricated and characterized.

DUV AlN MSM, Schottky barrier, and avalanche photodetectors (APDs) have been demonstrated by utlizing AlN epilayers grown on sapphire and n-SiC substrates. The fabricated AlN MSM PDs exhibited peak responsivity at 200 nm with a very sharp cut off wavelength at 207 nm as well as extremely low dark current, very high breakdown voltages, high responsivity (0.12 A/W at V_b=10 V), and more than four orders of magnitude of DUV to UV/visible rejection ratio. Moreover, AlN Schottky barrier PDs grown on n-SiC substrates exhibited very high reverse breakdown voltage (>200 V), extremely low dark current (less than 10 fA at V_b =−50 V), high responsivity, and thermal energy limited detectivity around 1.0 x 10^{15} cm $Hz^{1/2}$ W^{-1}, which is one of the highest values reported so far for AlGaN based UV detectors. This very high detectivity is due to the extremely small dark current and high zero bias responsivity. Also, Schottky barrier PDs showed four orders of magnitude of DUV to UV/visible rejection ratio. AlN DUV detectors also showed better responsivity in the EUV region (wavelength down to 30 nm) than AlGaN and GaN based detectors. These outstanding features exhibited by MSM and Schottky barrier PDs are direct attributes of excellent fundamental material properties and the high quality of AlN epilayers. These results demonstrated that AlN epilayers are excellent materials for DUV opto-electronic device applications.

We have further demonstrated the linear mode operation of AlN based APDs which possess the shortest cutoff wavelength of 210 nm. The photocurrent multiplication reached a value of 1200 under −250 V (E_b=2.8 MV/cm) reverse bias. Also, the device size dependent

breakdown field suggests that Geiger mode operation could be achieved by further reducing the dislocation density and optimizing device size and geometry. These results further demonstrate that AlN is an excellent active DUV material for future DUV optoelectronic device applications.

We performed MOCVD growth, fabrication and characterization of InGaN solar cells by utilizing $In_xGa_{1-x}N$/GaN MQWs with the purpose of demonstrating solar cell operation in wavelengths longer those that of previous attainments. $In_xGa_{1-x}N$/GaN MQWs solar cell with x =0.3 exhibited open circuit voltage about 2 V, a fill factor of about 60% and delivered an unprecedented external quantum efficiency (QE) of 40% at 420 nm and 10% at 450 nm. The performance of the lower energy bandgap device (x=0.4 in $In_xGa_{1-x}N$ active region) was much poorer than that of the higher energy bandgap device (x=0.3 in $In_xGa_{1-x}N$ active region). This degradation in solar cell performance in the $In_{0.4}Ga_{0.6}N$ active layer is a direct consequence of reduced material quality which follows from increasing In content. The photovoltaic characteristics observed here are also consistent with the well established fact that the QE of III-nitride green LEDs are much lower than those of blue LEDs. One novel way to overcome this difficulty could be the utilization of nanostructures such as QDs, MQWs, nanowire, and nanotubes as active layers in the solar cell structure, because the size effects help to mitigate strain effects in the active layer.

We also studied the PLE properties of Er doped GaN and $In_{0.0}6Ga_{0.94}N$ epilayers synthesized by MOCVD and demonstrated current-injected 1.54 μm LEDs based on heterogeneous integration of MOCVD grown Er-doped III-nitride epilayers with III-nitride UV LEDs. The Er emission intensity at 1.54 μm increases significantly as the excitation energy is tuned from below to above the energy bandgap of these epilayers, indicating that the band-to-

band excitation of the host material and subsequent electron and hole mediated energy transfer to Er^{3+} ions is an efficient excitation mechanism for 1.54 μm emission compared to below bandgap excitation. It was observed that the 1.54 μm emission intensity increases almost linearly with the input forward current. These results further motivated us to fabricate optical waveguide amplifiers based on MOCVD-grown Er-doped GaN. We fabricated stripe waveguide based on Er doped GaN and AlGaN heterostructure. The measured optical loss of the fabricated devices was ~3.5 cm^{-1} at 1.54 μm. The optical amplification characteristics of the devices were analyzed by studying the relative change in 1.54 μm input signal intensity transmitted through the waveguide. We observed that the transmitted 1.54 μm signal intensity through the waveguide was amplified under the excitation of a broadband 365 nm nitride LED and a relative signal enhancement of about 8 dB/cm was observed. The demonstrated 1.54 μm signal enhancement with a broadband LED excitation eliminates the finely tuned high power laser which is required for Er-doped silica glass waveguide amplifiers. The results further exhibited the feasibility of achieving compact and cost effective current injected optical waveguide amplifiers based on Er-doped III-nitride semiconductors for future optical communication applications.

References

1. S. Nakamura, S. Pearton, and G. Fasol, *The Blue Laser Diode*, 2nd ed. (Springer, New York, 2000).
2. T. Miyoshi, S. Masui, T. Okada, T. Yanamoto, T. Kozaki, S. Nagahama, and T. Mukai, Appl. Phys. Exp. **2,** 062201 (2009).
3. I. Akasaki and H. Amano, Jpn. J. Appl. Phys. **35**, L838 (1996).
4. M. Razeghi and M. Henini, *Optoelectronic devices: III-Nitrides*. Ist ed. Elsevier Ltd., 2004.
5. U. K. Mishra, P. Parikh, and Y.-F. Wu, *Proc. IEEE*, Vol. **90**, 1022 (2002).
6. M. Ali, V. Cimalla, V. Lebedev, H. Romanus, V. Tilak, D. Merfeld, P. Sandvik, and O. Ambacher**,** Sensors and Actuators B: Chemical, Vol. **113**, 797 (2006).
7. I. Georgakoudi, I. Tsai, C. Greiner, C. Wong, J. DeFelice, and D. Kaplan, Optics Express, Vol. **15**, 1043 (2007).
8. M. S. Shur and R. Gaska, Proc. of SPIE Vol. **6894,** 689419 (2008).
9. http://en.wikipedia.org/wiki/Wurtzite_(crystal_structure).
10. V. I. Gavrilenko and R. Q. Wu, Phys. Rev. B **61**, 2632 (2000).
11. A. Sciuto, F. Roccaforte, S. D. Franco, and V. Raineri, Appl. Phys. Lett. 89, 081111 (2006).
12. X. Xin, F. Yan, X. Sun, P. Alexandrove, C.M. Stahle, J. Hu, M. Matsumura, X. Li, M. Weiner, and H. J. Zhao, Electron. Lett. Vol. **41**, 4 (2005).
13. H. Miyake, H. Yasukawa, Y. Kida, K. Ohta, Y. Shibata, A. Motogaito, K. Hiramatsu, Y. Ohuchi, K. Tadatomo, Y. Hamamura, and K. Fukui, Phys. Stat. Sol. (a) **200**, 151 (2003).
14. Y. Taniyasu, M. Kasu, and T. Makimoto, Appl. Phys. Lett. **89**, 182112 (2006).
15. Y. Taniyasu, M. Kasu, and T. Makimoto, Nature **441**, 325 (2006).
16. A. BenMoussa, J. F. Hochedez, R. Dahal, J. Li, J. Y. Lin, H. X. Jiang, A. Soltani, J. C. De Jaeger, U. Kroth, and M. Richter, Appl. Phys. Lett. **92**, 022108 (2008).
17. J. C. Carrano, T. Li, P. A. Grudowski, R. D. Dupuis, and J. C. Campbell: IEEE Circuits & Devices **15**, 15 (1999).
18. E. Munoz, E. Monroy, J. L. Pau, F. Calle, F. Omnes, and P. Gibart: J. Phys.: Condens. Matt. **13**, 7115 (2001).

19. M. Razeghi, Proc. IEEE **90**, 1006 (2002).

20. E. Monroy, F. Omnes and F. Calle, Semicond. Sci. Technol. **18**, R33 (2003).

21. M. S. Shur and M. A. Khan, in Gallium Nitride (GaN) II, eds. J. I. Pankove and T. D. Moustakas (Academic Press, San Diego, 1999), Semiconductors and Semimetals, Vol. **57**, p. 407.

22. H. J. Möller, Semiconductor for solar cells. (Artech Housing, Inc., Norwood, MA, 1993).

23. J. A. Mazer, Solar Cells, An Introduction to crystalline Photovoltaic Technology. (Kluwer Academic Publisher, Boston, 1997).

24. O. Jani, I. Ferguson, C. Honsberg, and S. Kurtz, Appl. Phys. Lett. **91**, 132117 (2007).

25. X. Chen, K. D. Matthews, D. Hao, W. J. Schaff, and L. F. Eastman, Phys. Stat. Sol. (a), Vol. **205**, 1103 (2005).

26. Y. Nanishi, Y. Satio, and T. Yamaguchi, Jpn. J. Appl. Phys., Part 1 **42**, 2549 (2003).

27. M. Vazquez, C. Algora, I. Rey-Stolle, and J. R. Gonzalez, Prog. Photovoltaics **15**, 477 (2007).

28. C. J. Neufeld, N. G. Toledo, S. C. Cruz, M. Iza, S. P. DenBaars, and U. K. Mishra, Appl. Phys. Lett. **93**, 143502 (2008).

29. J. Wu, W. Walukiewicz, K. M. Yu, W. Shan, J. W. Ager, E. E. Haller, H. Lu, W. J. Schaff, W. K. Metzger, and S. Kurtz, J. Appl. Phys. **94**, 6477 (2003).

30. J. W. Ager and W. Walukiewicz, *High efficiency radiation hard solar cells,* Lawrence Berkeley National Laboratory report 56326, 2004.

31. K. W. J. Barnham and G. Duggan, J. Appl. Phys. **67**, 3490 (1990).

32. A. Luque and A. Martí, Phys. Rev. Lett. **78**, 5014 (1997).

33. R. Dahal, B. Pantha, J. Li, J. Y. Lin, and H. X. Jiang, Appl. Phys. Lett. **94**, 063505 (2009).

34. R. Oshima, A. Takata, and Y. Okada, Appl. Phys. Lett. **93**, 083111 (2008).

35. G. Wei, K. T. Shiu, N. C. Giebink, and S. R. Forrest, Appl. Phys. Lett. **91**, 223507 (2007).

36. A. J. Steckl and R. Birkhahn, Appl. Phys. Lett. **73**, 1700 (1998).

37. P. N. Favennec, H. L'Haridon, M. Salvi, D. Moutonnet, and Y. Le Guillou, Electron. Lett. **25**, 718 (1989).

38. J. M. Zavada and D. Zhang, Solid-State Electron. **38**, 1285 (1995).

39. M. R. Brown, A. F. J. Cox, W. A. Shand, and J. M. Williams, Advances in Quantum Electronics **2**, 69 (1974).

40. H. Ennen, J. Schneider, G. Pomrenke, and A. Axmann, Appl. Phys. Lett. **43**, 943 (1983).

41. R. Birkhahn, M. Garter, and A. J. Steckl, Appl. Phys. Lett. **74**, 2161 (1999).

42. R. G. Wilson, R. N. Schwartz, C. R. Abernathy, S. J. Pearton, N. Newman, M. Rubin,T. Fu, and J. M. Zavada, Appl. Phys. Lett. **65**, 992 (1994).

43. S. Kim, S. J. Rhee, X. Li, J. J. Coleman, and S. G. Bishop, Appl. Phys. Lett. **76**, 2403 (2000).

44. J. T. Torvik, R. J. Feuerstein, J. I. Pankove, C. H. Qiu, and F. Namavar, Appl. Phys. Lett. **69**, 2098 (1996).

45. J. Barden, Physical Review, **71**, 717 (1974).

46. S. M. Sze and K. K. Ng, Physics of Semiconductor Devices, 3rd Ed. (John Wiley & Sons, Inc. Hobboken, NewJersey, 2007).

47. F. W. Smith, H. Q. Le, V. Diadiuk, M. A. Hollis, A. R. Calawa, S. Gupta, and M. Frankel, D. R. Dykaar, G. A. Mourou, and T. Y. Hsiang, Appl. Phys. Lett. **54**, 890-892, (1989).

48. J. F. Holzman, F. E. Vermeulen, and A. Y. Elezzabi, IEEE J. Quantum Electron. **36**, 30-136, (2000).

49. W. Roth, H. Schumacher, J. Kluge, H.J. Geelen, and H. Beneking, IEEE, Trans. Electron. Devices, **ED-32**, 1034-1036, (1985).

50. B. J. Van Zeghbroeck, W. Patrick, J. M. Halbout, and P. Vettiger, IEEE Electron Device Lett. **9**, 527-529, (1988).

51. W.C. Koscielniak, J. L. Pelouard, and M.A. Littlejohn, Appl. Phys. Lett., **54**, 567-69, (1989).

52. M. Razeghi and A. Rogalski, J. App. Phys. 79(10), 7433 (1996).

53. J. Li, K. B. Nam, M. L. Nakarmi, J. Y. Lin, and H. X. Jiang, Appl. Phys. Lett. **81**, 3365 (2002).

54. K. B. Nam, J. Li, M. L. Nakarmi, J. Y. Lin, and H. X. Jiang, Appl. Phys. Lett. **82**, 1694 (2003).
55. J. Li, K. B. Nam, M. L. Nakarmi, J. Li, J. Y. Lin, H. X. Jiang, P. Carrier, and S. H. Wei, Appl. Phys. Lett. **83**, 5163 (2003).
56. V. Adivarahan, S. Wu, J. P. Zhang, A. Chitinis, M. Shatalov, V. Mandavilli, R. Gaska, and M. Asif Khan, Appl. Phys. Lett. **81**, 4910 (2002).
57. A. Yasan, R. McClintock, K. Mayes, D. Shiell, L. Gautero, S. R. Darvish, P. Kung, and M. Razeghi, Appl. Phys. Lett. **83**, 4701 (2003).
58. A. Hanlon, P. M. Pattison, J. F. Kaeding, R. Sharma, P. Fini, and S. Nakamura, Jpn. J. Appl. Phys., Part 2 **42**, L628 (2003).
59. J. Fischer, A. A. Allerman, M. H. Crawford, K. H. A. Bogart, S. R. Lee, R. J. Kaplar, W. W. Chow, S. R. Kurtz, K. W. Fullmer, and J. J. Figiel, Appl. Phys. Lett. **84**, 3394 (2004).
60. K. H. Kim, Z. Y. Fan, M. Khizar, M. L. Nakarmi, J. Y. Lin, and H. X. Jiang, Appl. Phys. Lett. **85**, 4777 (2004).
61. M. L. Nakarmi, K. H. Kim, M. Khizar, Z. Y. Fan, J. Y. Lin, and H. X. Jiang, Appl. Phys. Lett. **86**, 092108 (2005).
62. Y. Taniyasu, M. Kasu, and N. Kobayashi, Appl. Phys. Lett. **81**, 1255 (2002).
63. M. L. Nakarmi, K. H. Kim, K. Zhu, J. Y. Lin, and H. X. Jiang, Appl. Phys. Lett. **85**, 3769 (2004).
64. Y. Taniyasu, M. Kasu, and T. Makimoto, Appl. Phys. Lett. **85**, 4672 (2004).
65. T. Ive, O. Brandt, H. Kostial, K. J. Friedland, L. Daweritz, and K. H. Ploog, Appl. Phys. Lett. **86**, 024106 (2005).
66. D. Walker, X. Zhang, P. Kung, A. Saxler, S. Javapour, J. Xu, and M. Razeghi, Appl. Phys. Lett. **68**, 2100 (1996).
67. W. Lim, Q. C. Chen, J. Y. Yang, and M. Asif Khan, Appl. Phys. Lett. **68**, 3761 (1996).
68. A. Osinsky, S. Gangopadhyay, B. W. Lim, M. Z. Anwar, M. A. Khan, D. V. Kuksenkov, and H. Temkin, Appl. Phys. Lett. **72**, 742 (1998).
69. Walker, V. Kumar, K. Mi, P. Sandvik, P. Kung, X. H. Zhang, and M. Razeghi, Appl. Phys. Lett. **76**, 403 (2000).
70. T. Li, D. J. H. Lambert, A. L. Beck, C. J. Collins, B. Yang, J. M. M. Wong, U. Chowdhury, R. D. Dupuis, and J. C. Campbell, Electron. Lett. **36**, 1581 (2000).

71. M. M. Wong, U. Chowdhury, C. J. Collins, B. Yang, J. C. Denyszyn, K. S. Kim, J. C. Campbell, and R. D. Dupuis, Phys. Status Solidi A **188**, 333 (2001).
72. J. Collins, U. Chowdhury, M. M. Wong, B. Yang, A. L. Beck, R. D. Dupuis, and J. C. Campbell, Appl. Phys. Lett. **80**, 3754 (2002).
73. J. Y. Duboz, J. L. Reverchon, D. Adam, B. Damilano, N. Grandjean, F. Semond, and J. Massies, J. Appl. Phys. **92**, 5602 (2002).
74. U. Chowdhury, M. M. Wong, C. J. Collins, B. Yang, J. C. Denyszyn, J. C. Campbell, and D. Dupuis, J. Cryst. Growth **248**, 552 (2003).
75. N. Biyikli, I. Kimukin, T. Kartaloglu, O. Aytur, and E. Ozbay, Phys. Status Solidi C **7**, 2314 (2003).
76. N. Biyikli, I. Kimukin, T. Kartaloglu, O. Aytur, and E. Ozbay, Electron. Lett. **41**, 276 (2005).
77. S. Butun, T. Tut, B. Butun, M. Gokkavas, H. Yu, and E. Ozbay, Appl. Phys. Lett. **88**, 123503 (2006).
78. B. Heying, X. H. Wu, S. Keller, Y. Li, D. Kapolnek, B. P. Keller, S. P. DenBaars, and J. S. Speck, Appl. Phys. Lett. **68**, 643 (1996).
79. Y. J. Sun, O. Brandt, T. Y. Liu, A. Trampert, K. H. Ploog, J. Bläsing, and A. Krost, Appl. Phys. Lett. **81**, 4928 (2002).
80. L. C. Chen, M. S. Fu, and I. L. Huang, Jpn. J. Appl. Phys. Part 1 **43**, 3353 (2004).
81. K. B. Nam, J. Li, M. L. Nakarmi, J. Y. Lin, and H. X. Jiang, Appl. Phys. Lett. **81**, 1038 (2002).
82. J. Li, Z. Y. Fan, R. Dahal, M. L. Nakarmi, J. Y. Lin, and H. X. Jiang, Appl. Phys. Lett. **89**, 213510 (2006).
83. C. J. Collins, U. Chowdhury, M. M. Wong, B. Yang, A. L. Beck, R. D. Dupuis, and J. C. Campbell, Appl. Phys. Lett. **80**, 3754 (2002).
84. C. Pernot, A. Hirano, M. Iwaya, T. Detchprohm, H. Amano, and I. Akasaki, Jpn. J. Appl. Phys., Part 1 **39**, 387 (2000).
85. N. Biyikli, O. Aytur, I. Kimukin, T. Tut, and E. Ozbay, Appl. Phys. Lett. **81**, 3272 (2002).
86. N. Biyikli, I. Kimukin, O. Aytur, and E. Ozbay, IEEE Photonics Technol. Lett. **16**, 1718 (2004).

87. T. Tut, N. Biyikli, I. Kimukin, T. Kartaloglu, O. Aytur, M. S. Unlc, and E. Ozbay, Solid-State Electron. **49**, 117 (2005).

88. X. Xin, F. Fan, T. W. Koeth, C. Joseph, J. Hu, and J. H. Zhao, Electron. Lett. **41**, 1192 (2005).

89. E. J. Tarsa, P. Kozodoy, J. Ibbetson, B. P. Keller, G. Parish, and U. Mishra, Appl. Phys. Lett. **77**, 316 (2000).

90. H. Miyaki, H. Yasukawa, Y. Shibata, A. Motogaito, K. Hiramatsu, Y. Ohuchi, Y. Hamamura, and K. Fukui, Phys. Status Solidi A **200**, 151 (2003).

91. H. Jiang, T. Egawa, and H. Ishikawa, IEEE Photonics Technol. Lett. **18**, 1353 (2006).

92. M. O. Aboelfotoh, R. S. Kern, S. Tanaka, and R. F. Davis, Appl. Phys. Lett. **69**, 2873 (1996).

93. C. M. Zetterling, M. Östling, N. Nordell, O. Schön, and M. Deschler, Appl. Phys. Lett. **70**, 3549 (1997).

94. L. Lipkin and J. Palmour, IEEE Trans. Electron Devices **46**, 525 (1999).

95. J. Choi, R. Puthenkovilakam, and G. P. Chang, Appl. Phys. Lett. **86**, 192101 (2005).

96. S. Donati, *Photodetectors, Devices, Circuits, and Applications* (Prientice-Hall, Englewood Cliffs, NJ, 2000), p. 43.

97. B. N. Pantha, R. Dahal, M. L. Nakarmi, N. Nepal, J. Li, J. Y. Lin, H. X. Jiang, Q. S. Paduano, and D. Weyburne , Appl. Phys. Lett. **90**, 241101 (2007).

98. P. Lu, J.H. Edgar, C. Cao, K. Hohn, R. Dalmau, R. Schlesser, and Z. Sitar, J. Crystal Growth, **310**, 2464-2470 (2008).

99. H. Hirayama, N. Noguchi, S. Fujikawa, J. Norimatsu, N. Kamata, T. Takano and K. Tsubaki, Proc. SPIE, Vol. **7216**, 721621 (2009).

100. M. Kneissl, Z. Yang, M. Teepe, C. Knollenberg, O. Schmidt, P. Kiesel, N. M. Johnson, S. Schujman, and L. J. Schowalter, J. Appl. Phys. **101**, 123103 (2007).

101. T. Takano, Y. Narita, A. Horiuchi, and H. Kawanishi, Appl. Phys. Lett. **84**, 3567(2004).

102. H. Jiang, and T. Egawa, Appl. Phys. Lett. **90**, 121121 (2007).

103. M. Horita, J. Suda, and T. Kimoto, Appl. Phys. Lett. **89**, 112117 (2006).

104. R. Dahal, T. M. Al Tahtamouni, Z. Y. Fan, J. Y. Lin, and H. X. Jiang, Appl. Phys. Lett. **90**, 263505 (2007).

105. T. Tut, M. Gokkavas, A. Inal, and E. Ozbay, Appl. Phys. Lett. **90**, 163506 (2007).

106. R. McClintock, A. Yasan, K. Minder, P. Kung, and M. Razeghi, Appl. Phys. Lett. **87**, 241123 (2005).

107. T. Tut, S. Butan, B. Butan, M. Gokkavas, H. Yu, and E. Ozbay, Appl. Phys. Lett. **87**, 223502 (2005).

108. J. B. Limb, D. Yoo, J. H. Ryou, W. Lee, S. C. Shen, R. D. Dupuis, M. L. Reed, C. J. Collins, M. Wraback, D. Hanser, E. Preble, N. M. Williams, and K. Evans, Appl. Phys. Lett. **89**, 011112 (2006).

109. A. Nishikawa, K. Kumakura, and T. Makimoto, Jpn. J. Appl. Phys., Part 1 **46**, 2316 (2007).

110. M. O. Aboelfotoh, R. S. Kern, S. Tanaka, R. F. Davis, and C. I. Harris, Appl. Phys. Lett. **69**, 2873 (1996).

111. D. Wood, *Optoelectronic Semiconductor Devices* (Prentice Hall, UK, 1994), pp. 331–332.

112. V. W. L. Chin, T. L. Tansley, and T. Osotchan, J. Appl. Phys. **75**, 7365 (1994).

113. S. K. O'Leary, B. E. Foutz, M. S. Shur, U. V. Bhapkar, and L. F. Eastman, Solid State Commun. **105**, 621 (1998).

114. C. Sevik and C. Bulutay, Appl. Phys. Lett. **83**, 1383 (2003).

115. S. Nakamura, M. Senoh, S. Nagahama, N. Iwasa, T. Yamada, T. Matsushita, Y. Sugimoto, and H. Kiyoku, Appl. Phys. Lett. **69**, 1477 (1996).

116. T. Kozaki, S. Nagahama, and T. Mukai, Proc. SPIE **6485**, 648503 (2007).

117. C. Skierbiszewski, P. Winiewski, M. Siekacz, P. Perlin, A. Feduniewicz-Zmuda, G. Nowak, I. Grzegory, M. Leszczyński, and S. Porowski, Appl. Phys. Lett. **88**, 221108 (2006).

118. H. X. Jiang, S. X. Jin, J. Li, J. Shakya, and J. Y. Lin, Appl. Phys. Lett. **78**, 1303 (2001).

119. M. Funato, M. Unde, Y. Kawakami, Y. Narukawa, T. Kosugi, M. Takanashi, and T. Mukai, Jpn. J. Appl. Phys., Part 2 **45**, L659 (2006).

120. T. Lu, C. Kao, H. Kuo, G. Huang, and S. Wang, Appl. Phys. Lett. **92**, 141102 (2008).

121. A. De Vos, *Endoreversible Thermodynamics of Solar Energy Conversion* (Oxford University Press, Oxford, 1992), p. 90.

122. I. Ho and G. B. Stringfellow, Appl. Phys. Lett. **69**, 2701 (1996).

123. S. Y. Karpov, MRS Internet J. Nitride Semicond. Res. **3**, 16 (1998).

124. B. N. Pantha, J. Li, J. Y. Lin, and H. X. Jiang, Appl. Phys. Lett. **93**, 182107 (2008).

125. R. Singh, D. Doppalapudi, T. D. Moustakas, and L. T. Romano, Appl. Phys. Lett. **70**, 1089 (1997).

126. A. Tabata, L. K. Teles, L. M. R. Scolfaro, J. R. Leite, A. Kharchenko, T. Frey, D. J. As, D. Schikora, K. Lischka, J. Furthmuller, and F. Bechstedt, Appl. Phys. Lett. **80**, 769 (2002).

127. P. G. Kik and A. Polman, MRS Bull. **23**, 48 (1998).

128. J. M. Zavada, S. X. Jin, N. Nepal, J. Y. Lin, H. X. Jiang, P. Chow, and B. Hertog, Appl. Phys. Lett. **84**, 1061 (2004).

129. J. M. Zavada, N. Nepal, C. Ugolini, J. Y. Lin, H. X. Jiang, R. Devies, J. Hite, C. R. Abernathy, S. J. Pearton, E. E. Brown, and U. Hommerich, Appl. Phys. Lett. **91**, 054106 (2007).

130. K. P. O'Donnel and B. Hourahine, Eur. Phys. J. Appl. Phys. **36**, 91 (2006).

131. U. Hommerich, M. Thaik, R. N. Schwartz, R. G. Wilson, J. M. Zavada, S. J. Pearton, C. R. Abernathy, and J. D. MacKenzie, Proc.-Electrochem. Soc. **2**, 110 (1998).

132. J. T. Torvik, C. H. Qiu, R. J. Feuerstein, J. I. Pankove, and F. Namavar, J. Appl. Phys. **81**, 6343 (1997).

133. J. T. Seo, U. Hommerich, J. D. MacKenzie, C. R. Abernathy, and J. M. Zavada, J. Korean Phys. Soc. **36**, 311 (2000).

134. M. A. J. Klik, I. Izeddin, J. Phillips, and T. Gregorkiewicz, Mater. Sci. Eng., B **105**, 141 (2003).

135. J. M. Zavada, U. Hommerich, and A. J. Steckl, *III-Nitride Semiconductors: Optical Properties I*, edited by M. O. Manasreh and H. X. Jiang, (Taylor & Francis, New York, 2002).

136. C. Ugolini, N. Nepal, J. Y. Lin, H. X. Jiang, and J. M. Zavada, Appl. Phys. Lett. **89**, 151903 (2006).

137. G. N. van den Hoven, R. J. I. M. Koper, A. Polman, C. van Dam, J. W. M. van Uffelene, and M. K. Smit, Appl. Phys. Lett. **68**, 1886 (1996).

138. M. A. Lourenco, R. M. Gwilliam, and K. P. Homewood, Appl. Phys. Lett. **91**, 141122 (2007).

139. P. Joshi, S. Shen, and A. Jha, J. Appl. Phys. **103**, 083543 (2008).

140. D. Zhang, C. Chen, C. Ma, D. Zhang, S. Bo, and Z. Zhen, Appl. Phys. Lett. **91**, 161109 (2007).

141. S. Zhou, H. Dong, H. Zeng, J. Hao, J. Chen, and J. Qiu, J. Appl. Phys. **103**, 103532 (2008).

142. H. S. Han, S. Y. Seo, and J. H. Shin, Appl. Phys. Lett. **79**, 4568 (2001).

143. G. Karve, B. Bihari, and R. T. Chen, Appl. Phys. Lett. **77**, 1253 (2000).

144. C. C. Baker, J. Heikenfeld, Z. Yu, and A. J. Steckl, Appl. Phys. Lett. **84**, 1462 (2004). (2003).

145. C. Ugolini, N. Nepal, J. Y. Lin, H. X. Jiang, and J. M. Zavada, Appl. Phys. Lett. **90**, 051110 (2007).

146. R. Dahal, C. Ugolini, J. Y. Lin, H. X. Jiang, and J. M. Zavada, Appl. Phys. Lett. **93**, 033502 (2008).

147. Y. C. Yan, A. J. Faber, H. de Waal, A. Polman, and P. G. Kik, Appl. Phys. Lett. **71**, 2922 (1997).

148. O. Skorka, B. Meyler, and J. Salzman, Appl. Phys. Lett. **84**, 3801 (2004).

Appendix

Reswarch Work Publications

1. **R. Dahal**, C. Ugolini, J.Y. Lin, H.X. Jiang, and J.M. Zavada, “Nitride optical waveguide amplifiers”, Appl. Phys. Lett. **95**, 111109 (2009)
2. S. Nikishin, B. Borisov, M. Pandikunta, **R. Dahal**, J. Y. Lin, H.X. Jiang, H. Harris, and M. Holtz, “High quality AlN for deep UV photodetectors”, Appl. Phys. Lett. **95**, 054101 (2009)
3. N. Nepal, J. M. Zavada, **R. Dahal**, C. Ugolini, A. Sedhain, J. Y. Lin, and H.X. Jiang, “Optical enhancement of room temperature ferromagnetism in Er doped GaN epilayers”, Appl. Phys. Lett. **95**, 022510 (2009).
4. A. BenMoussa , A. Soltani, U. Schühle, K. Haenen, Y.M. Chong, W.J. Zhang, **R. Dahal**, J.Y. Lin, H.X. Jiang, H. A. Barkad, B. BenMoussa, D. Bolsee, C. Hermans, U. Kroth, C. Laubis, V. Mortet, J.C. De Jaeger, B. Giordanengo, M. Richter, F. Scholze, and J.F.Hochedez, “Recent developments of wide-bandgap semiconductor based UV sensors”. Diamond and related materials, **18**, 860 (2009).
5. B. Giordanengo, A. Ben Moussa, J.-F. Hochedez, A. Soltani, P. de Moor, K. Minoglou, P. Malinowski, J.-Y. Duboz, Y.M. Chong, Y.S. Zou, W.J. Zhang, S.T. Lee, **R. Dahal**, J. Li, J.Y. Lin and H.X. Jiang “ Recent ROB developments of on wideband gap based UV sensors” Astrophysics Detector Workshop 2008,P. Kern (ed) EAS Publications Series, **37,**) 199(2009).
6. B. N. Pantha, **R. Dahal**, J. Li, J. Y. Lin, H. X. Jiang, and G. Pomrenke, “Thermoelectric Properties of $In_{0.3}Ga_{0.7}N$ Alloys”, Journal of Electronic Material, **38**, 7, pp.1132-1135 (2009).
7. **R. Dahal**, B. Pantha, J. Li, J. Y. Lin, and H. X. Jiang, “InGaN/GaN multiple quantum well solar cells with long operating wavelengths”, Appl. Phys. Lett. **94**, 063505 (2009).

8. **R. Dahal,** C. Ugolini, J. Y. Lin, H.X. Jiang, and J. M. Zavada**,** "Current-injected 1.54 μm light emitting diodes based on erbium-doped GaN**",** Appl. Phys. Lett. **93**, 033502 (2008).

9. **R. Dahal**, J. Li, Z. Y. Fan, M. L. Nakarmi, T. M. Al Tahtamouni, J. Y. Lin, and H. X. Jiang, **"**AlN MSM and Schottky photodetectors**",** phys. stat. sol. (c), 1– 4 (2008).

10. B. N. Pantha, **R. Dahal**, J. Li, J. Y. Lin, H. X. Jiang, and G. Pomrenke, '**'**Thermoelectric properties of $In_xGa_{1-x}N$ alloys**'',** Appl. Phys. Lett. **92**, 042112 (2008).

11. A. BenMoussa, J. F. Hochedez, **R. Dahal**, J. Li, J. Y. Lin, H. X. Jiang, A. Soltani, J.-C. De Jaeger, U. Kroth, and M. Richter "Characterization of AlN metal-semiconductor-metal diodes in the spectral range of 44–360 nm: Photoemission assessments**",** Appl. Phys. Lett. **92**, 022108 (2008).

12. **R. Dahal**, T. M. Al Tahtamouni, J. Y. Lin, and H. X. Jiang, "AlN avalanche photodetectors", Appl. Phys. Lett. **91**, 243503 (2007).

13. **R. Dahal**, T. M. Al Tahtamouni, Z. Y. Fan, J. Y. Lin, and H. X. Jiang, "Hybrid AlN–SiC deep ultraviolet Schottky barrier photodetectors", Appl. Phys. Lett. 90, 263505 (2007).

14. B. N. Pantha, **R. Dahal**, M. L. Nakarmi, N. Nepal, J. Li, J. Y. Lin, H. X. Jiang, Q. S. Paduano, and David Weyburne, "Correlation between optoelectronic and structural properties and epilayer thickness of AlN", Appl. Phys. Lett. **90**, 241101 (2007).

15. J. Li, Z. Y. Fan, **R. Dahal**, M. L Nakarmi, J. Y. Lin, and H. X. Jiang, "200 nm deep ultraviolet photodetectors based on AlN," Appl. Phys. Lett. **89**, 213510 (2006).

Research Work Presentations

1. **R. Dahal**, et al., “InGaN/GaN multiple quantum well solar cells with long operating wavelengths”, 65th Southwest regional meeting of the ACS, Materials for energy symposium, November 4-7, 2009, El Paso, TX, Presentation (Oral).
2. **R. Dahal** et al.,” Current-injected 1.54 µm emitters based on Er Doped GaN”, MRS Fall meeting, December 1-5, 2008, Boston MA, Presentation (Oral) # D3.8.
3. **R. Dahal** et al., “1.54 µm emitters based on monolithic integration of nitride emitters”APS march meeting, March 10-14, New Orleans, LA, 2008, Presentation (Oral)# J35.00008.
4. **R. Dahal** et al., “AlN MSM and Schottky photodetectors”ICNS-7, Los Vegas, Neveda, September, 16-21, 2007, (Poster).
5. **R. Dahal** et al., “200 nm deep ultraviolet photodetectors based on AlN”APS march meeting, March 5-9, 2007, Denver, CO, Presentation (Oral) # J41.000041.